EVALUATION OF SITE EFFECTS UTILIZING CASCADIA SUBDUCTION ZONE GROUND MOTIONS

Final Report

PROJECT SPR 824

Oregon Department of Transportation

EVALUATION OF SITE EFFECTS UTILIZING CASCADIA SUBDUCTION ZONE GROUND MOTIONS

Final Report

PROJECT SPR 824

By

Arash Khosravifar, PhD, PE
Peter Dusicka, PhD, PE
Nathan Villeneuve
Matthew O'Tousa

Department of Civil and Environmental Engineering
Portland State University

for

Oregon Department of Transportation
Research Section
555 13th Street NE, Suite 1
Salem OR 97301

and

Federal Highway Administration
1200 New Jersey Avenue SE
Washington, DC 20590

June 2023

Technical Report Documentation Page

1. Report No. FHWA-OR-RD-23-12	2. Government Accession No.	3. Recipient's Catalog No.
4. Title and Subtitle Evaluation of Site Effects Utilizing Cascadia Subduction Zone Ground Motions		5. Report Date June 2023 6. Performing Organization Code
7. Author(s) Arash Khosravifar, PhD, PE 0000-0002-7137-6289; Peter Dusicka, PhD, PE 0000-0003-2199-1619; Nathan Villeneuve 0000-0002-7802-5836; Matthew O'Tousa 0000-0001-8011-5315		8. Performing Organization Report No.
9. Performing Organization Name and Address Oregon Department of Transportation Research Section 555 13th Street NE, Suite 1 Salem, OR 97301		10. Work Unit No. (TRAIS) 11. Contract or Grant No.
12. Sponsoring Agency Name and Address Oregon Dept. of Transportation Research Section 555 13th Street NE, Suite 1 Salem, OR 97301 Federal Highway Admin. 1200 New Jersey Avenue SE Washington, DC 20590		13. Type of Report and Period Covered Final Report 14. Sponsoring Agency Code

15. Supplementary Notes

16. Abstract: The potential Cascadia Subduction Zone (CSZ) megathrust earthquake is recognized as one of the major natural hazards affecting the Pacific Northwest of the United States. The estimation of expected ground-motions is complicated by the long-duration motions from CSZ as well as site effects from deep sedimentary basins in northwest Oregon. This study evaluates the combined effects of long duration motions and basin effects on site amplification factors due to propagation of earthquake waves in surficial soils. Nonlinear and equivalent linear one-dimensional site response analyses were performed using broadband synthetic CSZ ground motions from the M9 Project. A web-based tool was developed to synthesize the vast data and geographically visualize the M9 ground motions as well as the subsequently computed response spectra. Five soil profiles representing a range of site classes from Site Class C to Site Class E were considered for the analyses. Ground motions were extracted at three locations inside major basins in Northwest Oregon (Portland basin, Tualatin basin, and North Willamette basin) and three comparable locations outside the basins. The effect of basin on soil amplification factor was characterized by comparing the soil amplifications inside and outside basins for the same soil profiles. The basin amplification factors calculated for CSZ broadband synthetic ground motions at bedrock (Site Class B/C) for selected sites within the three basins in Oregon were found to be noticeably larger than the ratios calculated from empirical correlations that are incorporated in New Generation Ground Motion Attenuation Models (NGA-West2). The soil amplification ratios calculated from the site response analyses were generally within the envelope of code-based site coefficients in ASCE 7, except for very short periods (<0.5 seconds). The effect of basins on soil amplification ratios ranged from 50% increase to 30% decrease at periods close to the natural period of the basin (generally between 1 sec and 2 sec). The implication of these findings on the use of code-based site coefficients and advantages of performing site-specific site response analysis are discussed.

17. Key Words ground motion, seismic hazard, basin effects, site effects	18. Distribution Statement: Copies available from NTIS, and online at www.oregon.gov/ODOT/TD/TP_RES/		
19. Security Classification (of this report): Unclassified	20. Security Classification (of this page): Unclassified	21. No. of Pages 111	22. Price

SI* (MODERN METRIC) CONVERSION FACTORS

APPROXIMATE CONVERSIONS TO SI UNITS

Symbol	When You Know	Multiply By	To Find	Symbol
		LENGTH		
in	inches	25.4	millimeters	mm
ft	feet	0.305	meters	m
yd	yards	0.914	meters	m
mi	miles	1.61	kilometers	km
		AREA		
in^2	square inches	645.2	millimeters squared	mm^2
ft^2	square feet	0.093	meters squared	m^2
yd^2	square yards	0.836	meters squared	m^2
ac	acres	0.405	hectares	ha
mi^2	square miles	2.59	kilometers squared	km^2
		VOLUME		
fl oz	fluid ounces	29.57	milliliters	ml
gal	gallons	3.785	liters	L
ft^3	cubic feet	0.028	meters cubed	m^3
yd^3	cubic yards	0.765	meters cubed	m^3
~NOTE: Volumes greater than 1000 L shall be shown in m^3.				
		MASS		
oz	ounces	28.35	grams	g
lb	pounds	0.454	kilograms	kg
T	short tons (2000 lb)	0.907	megagrams	Mg
		TEMPERATURE (exact)		
°F	Fahrenheit	(F-32)/1.8	Celsius	°C

APPROXIMATE CONVERSIONS FROM SI UNITS

Symbol	When You Know	Multiply By	To Find	Symbol
		LENGTH		
mm	millimeters	0.039	inches	in
m	meters	3.28	feet	ft
m	meters	1.09	yards	yd
km	kilometers	0.621	miles	mi
		AREA		
mm^2	millimeters squared	0.0016	square inches	in^2
m^2	meters squared	10.764	square feet	ft^2
m^2	meters squared	1.196	square yards	yd^2
ha	hectares	2.47	acres	ac
km^2	kilometers squared	0.386	square miles	mi^2
		VOLUME		
ml	milliliters	0.034	fluid ounces	fl oz
L	liters	0.264	gallons	gal
m^3	meters cubed	35.315	cubic feet	ft^3
m^3	meters cubed	1.308	cubic yards	yd^3
		MASS		
g	grams	0.035	ounces	oz
kg	kilograms	2.205	pounds	lb
Mg	megagrams	1.102	short tons (2000 lb)	T
		TEMPERATURE (exact)		
°C	Celsius	1.8C+32	Fahrenheit	°F

*SI is the symbol for the International System of Measurement

ACKNOWLEDGEMENTS

The authors would like to thank the members of ODOT's Technical Advisory Committee as well as the Research Section for their advice and assistance during the project and preparation of this report.

DISCLAIMER

TABLE OF CONTENTS

LIST OF TABLES

LIST OF FIGURES

1.0 INTRODUCTION

1.1 BACKGROUND

Seismic hazards have been recognized as one of the primary natural hazards facing the Pacific Northwest, highlighted by the potential for a Cascadia Subduction Zone (CSZ) megathrust earthquake. Great subduction zone earthquakes like the CSZ are difficult to study due to their relative rarity in the history of recorded earthquakes. The lack of region-specific data makes it difficult to understand properly the effects of local geology on the propagation of strong ground motions due to a CSZ rupture in the Pacific Northwest. Further complicating the issue is the presence of deep sedimentary basins in northwest Oregon, which have the potential to modify CSZ ground motions significantly.

This study evaluates how site effects are influenced by specific characteristics of CSZ earthquakes using seismic models and data recently developed by the M9 Project. This report documents the site response analyses performed for northwest Oregon basins using broadband synthetic CSZ ground motions from the M9 Project. Sections 2.0 through 5.0 present the methodologies and results of the site response analyses. Section 6.0 is a discussion of the results, and Section 7.0 summarizes the study and provides conclusions, recommendations for engineering practice, and suggestions for further research.

1.2 M9 PROJECT

While recent subduction zone earthquakes recorded in Chile and Japan have advanced our understanding of ground motion characteristics of subduction earthquakes, there are still no recorded CSZ ground motions. The M9 Project is a collaboration between the U.S. Geological Survey (USGS) and the University of Washington (UW) to reduce the potentially devastating effects of a CSZ earthquake by advancing seismic research, methodologies, and engineering and community practices. A key portion of the M9 research was the development of a seismic model of the Pacific Northwest, which was used to run 30 full-scale simulations of a CSZ megathrust earthquake. The data from these simulations, including velocity and acceleration time histories, rock depths (Z Values), and other associated data, was made available to this study to perform seismic hazard analyses related to geologic basins in northwest Oregon.

1.3 BASIN EFFECTS ON GROUND MOTIONS

Seismic waves are known to be modified by local geologic conditions, which can greatly influence nature of the wave as it passes from the source to the ground surface. This phenomenon is known as site effects and are accounted for in seismic codes by applying amplification factors for difference site classes. Deep sedimentary basins, typically consisting of alluvial deposits and low-velocity sedimentary rock, are a specific case of site effects that generally increase or amplify ground motions at the surface (Frankel et al., 2009; Hatayama et al., 2007). While basin effects are highly complex, the amplification effect is generally

attributed to the impedance of seismic waves between basin layers and the reflection of waves at the basin edges. Due to their size and shape, basins can trap reflected waves, extend the duration of shaking, and influence shaking over a wide area. Several studies have found that basins produce larger than expected damage demonstrated by several earthquakes, including the 1985 Michoacán (Hall & Beck, 1986), 2001 Nisqually (Frankel et al., 2009), and 2003 Tokachi-Oki (Hatayama et al., 2007).

1.4 NORTHWEST OREGON BASINS

The Willamette Valley is the southern portion of the Puget-Willamette lowland, a structural depression formed from tectonic activity related to the CSZ (Evarts et al., 2009). The structural history of the Willamette Valley and its recent depositional environment have resulted in an ideal setting for basin formation. Three distinct basins have been identified in northwest Oregon: the Portland Basin, the Tualatin Basin, and the North Willamette Basin (Evarts et al., 2009; McPhee et al., 2014). Figure 1.1 displays the locations of several basins in the Pacific Northwest, including those in northwest Oregon. While other basins exist across Oregon, the three basins above are located near major population centers and are investigated in this study. Figure 1.2 and Figure 1.3 show the three basins in northwest Oregon and the basement depth developed by McPhee et al. (2014). The basement depth may be considered approximately equal to $Z_{2.5}$, the depth corresponding to rock with a shear wave velocity of 2.5 km/sec.

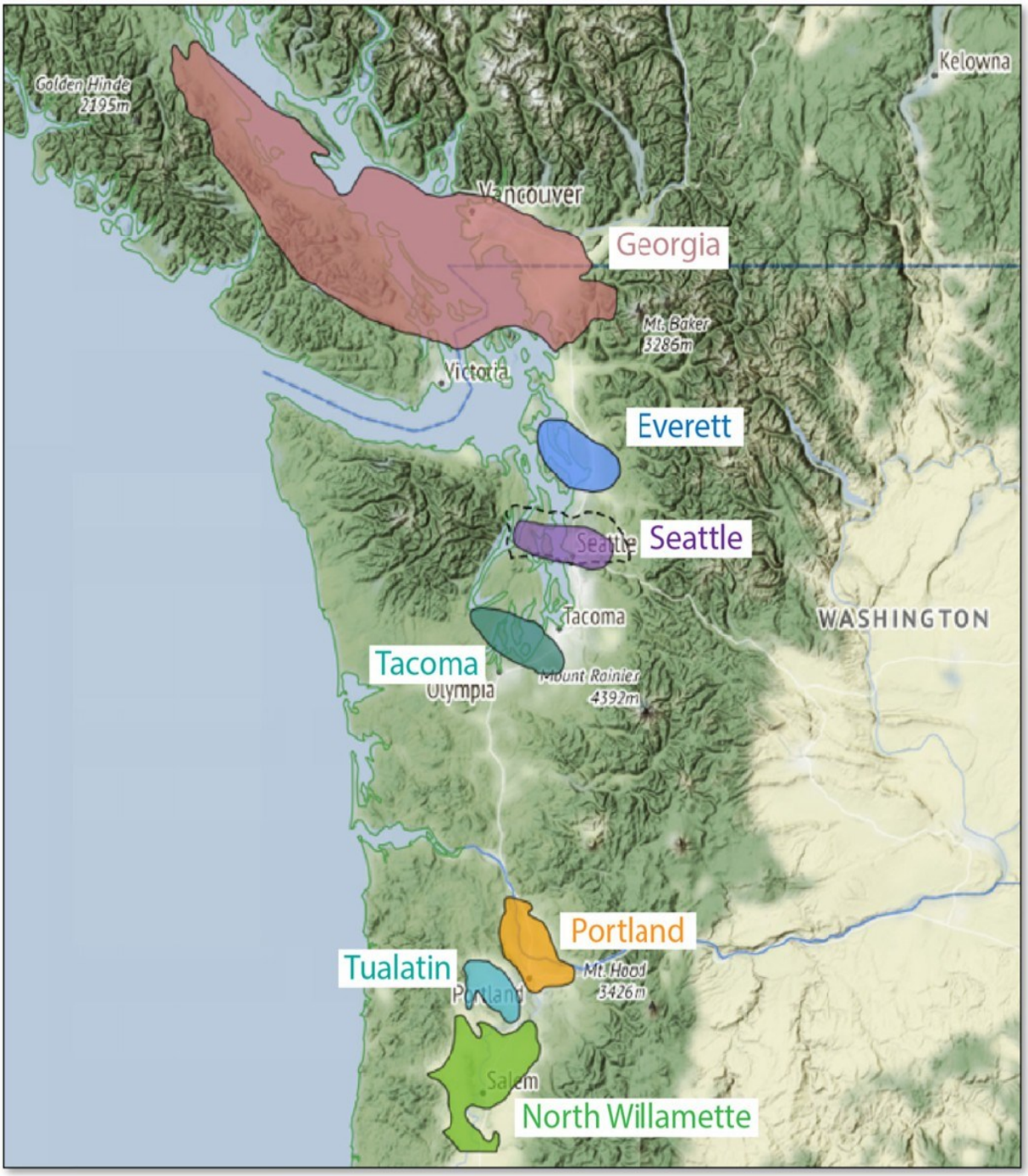

Figure 1.1: Basin Locations in the Pacific Northwest (Bozorgnia, 2020).

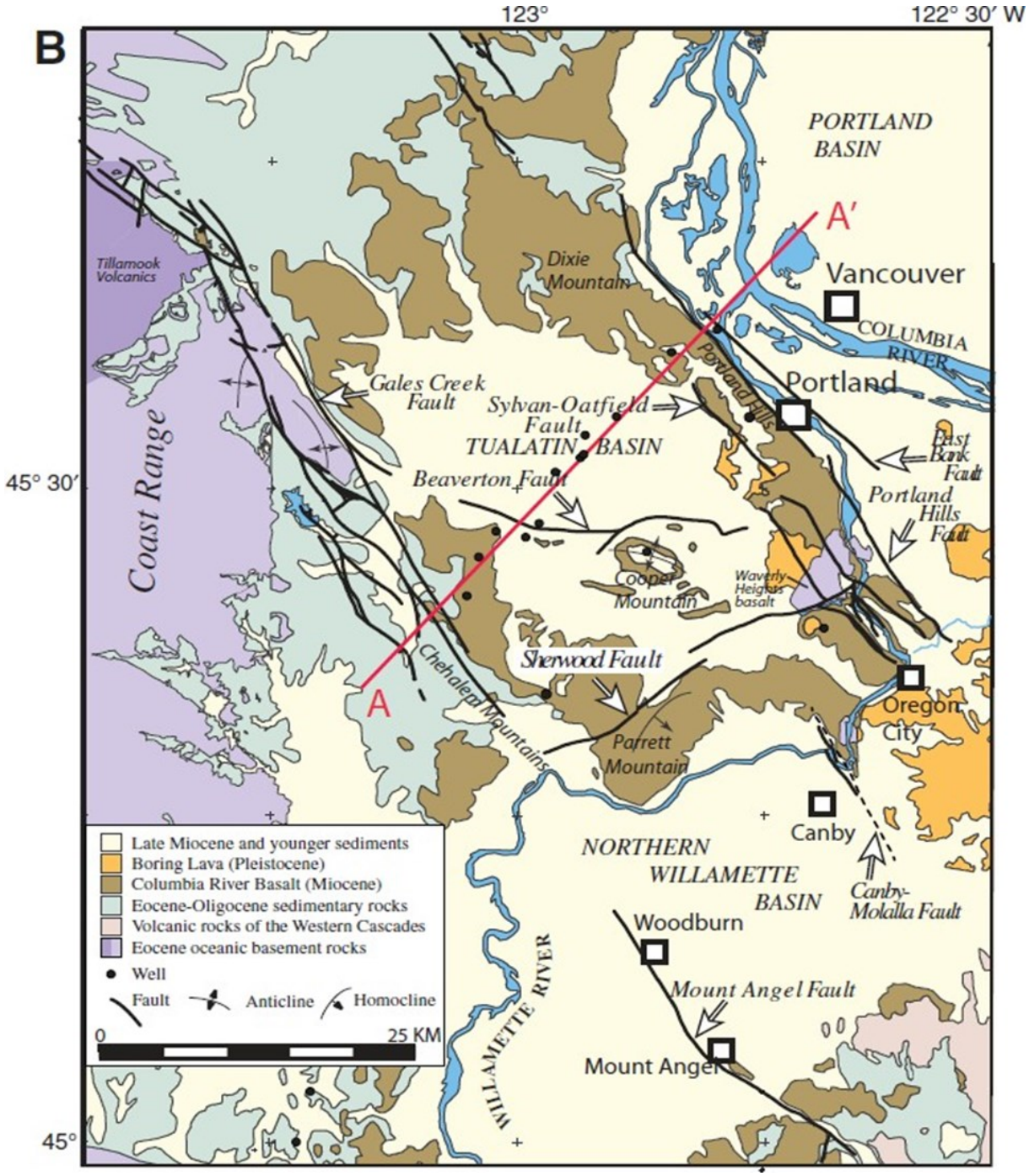

Figure 1.2: Map of three basins in northwest Oregon (McPhee et al. 2014).

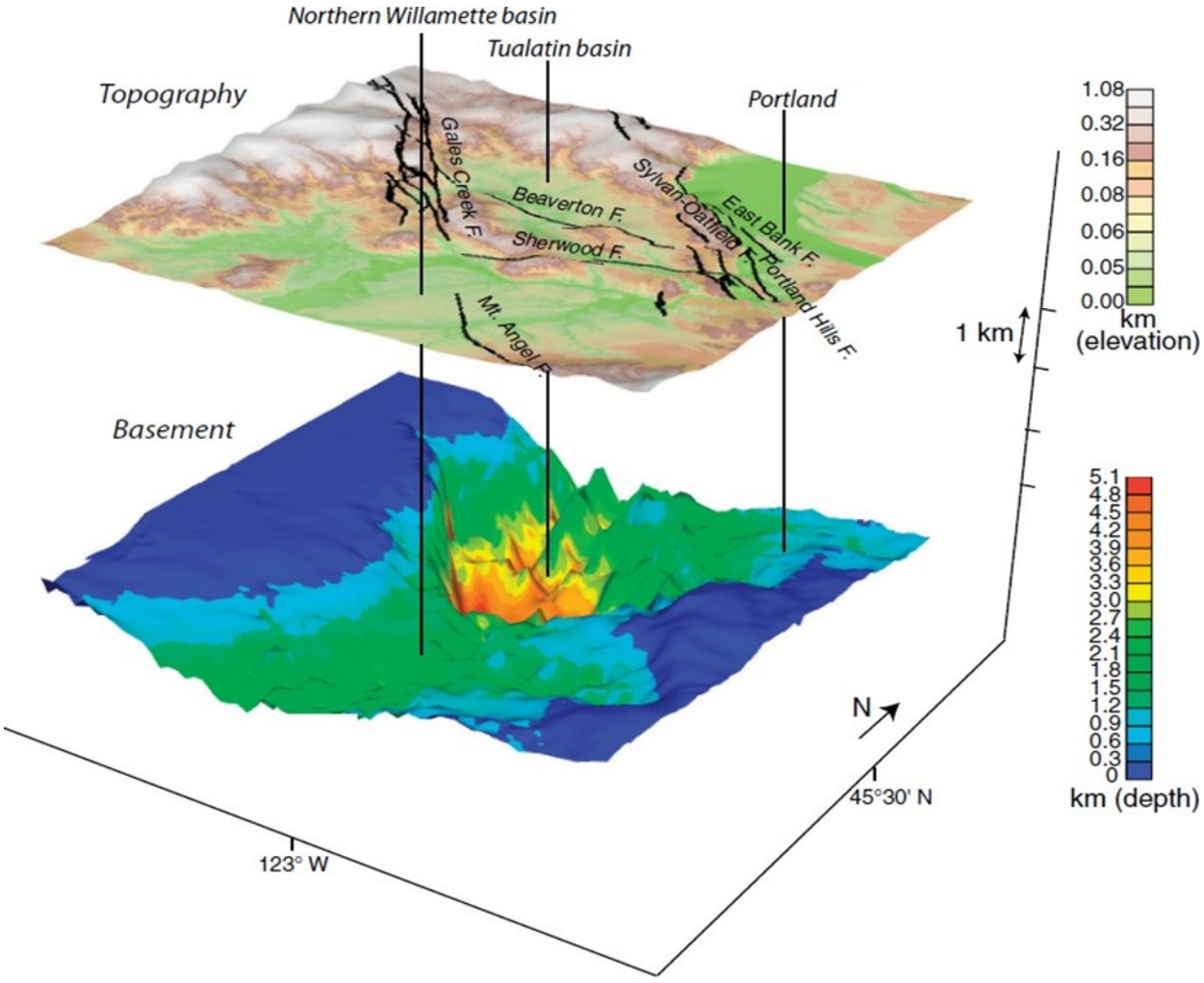

Figure 1.3: Topography and Depth to basement for three basins in northwest Oregon (McPhee et al. 2014).

1.4.1 Portland Basin

The Portland Basin is a 30 by 80-kilometer, northwest-trending basin covering much of eastern Portland and Vancouver. The basin is formed by a syncline in the Eocene and Oligocene basement rock and bounded by faults to the northeast and the Portland Hills to the southwest. Basin fill consists of Columbia River Basalt Group (CRBG) flows, Miocene and Pliocene sediments, and Quaternary alluvial and flood deposits (Evarts et al., 2009).

1.4.2 Tualatin Basin

The Tualatin Basin is a 20 by 30-kilometer, northwest-trending basin just to the west of the Portland Basin. The basin is formed from tectonic extension of Siletz terrane basement rock and is bounded to the northeast by the Portland Hills and to southwest by the Gales Creek Fault Zone. Basin fill consists of Eocene to Miocene sediments overlain by CRBG flows with Quaternary alluvial and flood deposits at the surface (McPhee et al., 2014).

1.4.3 North Willamette Basin

The North Willamette Basin (also referred to as Northern Willamette Basin) is located to the south of the Tualatin Basin and occupies much of the Willamette Valley from Canby south to Salem. The basin is bounded to the west by the Siletz terrane and marine sedimentary rocks of the Coast Range. To the east, the basin is bounded by the volcanic rocks of the Cascade Range. Basin fill consists of Quaternary alluvial and flood deposits with pockets of CRBG flows (McPhee et al., 2014).

1.5 PROJECT OBJECTIVES

The main objective of this study is to evaluate the effects of basins on site response considering that basin motions typically have larger acceleration spectral values at long periods. The site effects due to amplification/de-amplification of motions at the ground surface due to surficial soils (i.e., soft soil effects) are evaluated by performing site response analyses for five hypothetical soil profiles ranging from Site Class C to E. The site response analyses were performed using M9 rock motions extracted from six locations in Oregon (three inside of basins and three outside of basins) which were used to evaluate the potential effects of basins on soil amplifications. The soil amplification factors from site response analyses are compared to code-based site amplification ratios (i.e., F_a and F_v per ASCE 7-16) and practical recommendations are provided.

2.0 SIMULATED CSZ EARTHQUAKES

Frankel et al. (2018) developed a suite of 30 synthetic ground motions for Mw 9.0 earthquakes on the CSZ by combining results of 3D finite-difference simulations with finite-source, stochastic synthetics. The suite consists of 30 scenarios (herein referred to as "realizations") of a potential CSZ earthquake, each considering a different hypocenter location and rupture parameters.

The 3D finite-difference simulations used for long periods utilize the 3D velocity model of the Pacific Northwest developed by Stephenson et al. (2017). This P- and S-wave velocity model includes the crust and upper mantle up to a depth of 60 km, with the subducting slab and sedimentary basins as key features. The sedimentary basins are subdivided into Quaternary and Tertiary geologic units. Quaternary deposits in the Willamette Valley were not included in the model region. Therefore, the input ground motions account for the effects of basin amplification only from Tertiary geologic units.

2.1 GROUND MOTION SELECTION

The M9 rock motions used in this study correspond to a surface shear-wave velocity, Vs, of 650 m/s (Frankel et al. 2018). The M9 data used in this study was accessed via the under-development CSZ@PDX online tool. The tool provides spatial visualization of the M9 simulations in the form of map zones with selectable geographic coordinates in a grid pattern. Of the five available zones, two were used for this study. The Portland Zone (1 by 1 km grid) covers the Portland and Vancouver metro areas and includes the Portland and Tualatin basins. The PNW Zone (20 by 20 km grid) covers western Washington, western Oregon, and northwestern California and includes the NW basin. Once a coordinate is selected, various data for each of the 30 realizations is available to visualize and download. Data used for this project included spectral acceleration values, depth to rock (Z Values), and acceleration time histories.

Three coordinates were selected to represent each of the three basins. The inside basin ("IN" or "inside") coordinates were selected by reviewing the 5-percent damped response spectra of the M9 ground motions where basin Z Values were highest. Recent updates to seismic hazard maps and several ground motion models (GMMs) have included basin effects by correlation to Vs_{30} or the depth to shear wave velocities of 2.5, 1.5, and 1.0 km/sec corresponding to $Z_{2.5}$, $Z_{1.5}$, and $Z_{1.0}$, respectively. Therefore, the Z values were used as a proxy to delineate the boundaries of the three basins. Figure 2.1 shows $Z_{1.5}$ as an example for the studied area and the approximate boundaries of the three basins in northwest Oregon. The coordinates with the largest spectral acceleration values at a long period of 1.5 sec were selected to represent the basins. For comparison, a further three coordinates were selected to act as control or non-basin coordinates. The outside basin ("OUT" or "outside") coordinates were selected by reviewing the response spectra of M9 ground motions outside the boundary of a specific basin while maintaining the same longitude as the IN coordinates. The objective of maintaining longitude was to keep the rupture distance from the simulation hypocenters, which all occur off the coast, roughly similar.

The coordinates and associated acceleration time histories selected for analysis are summarized in Table 2.1 below. The locations of the coordinates are also presented on Figure 2.2 and Figure 2.3.

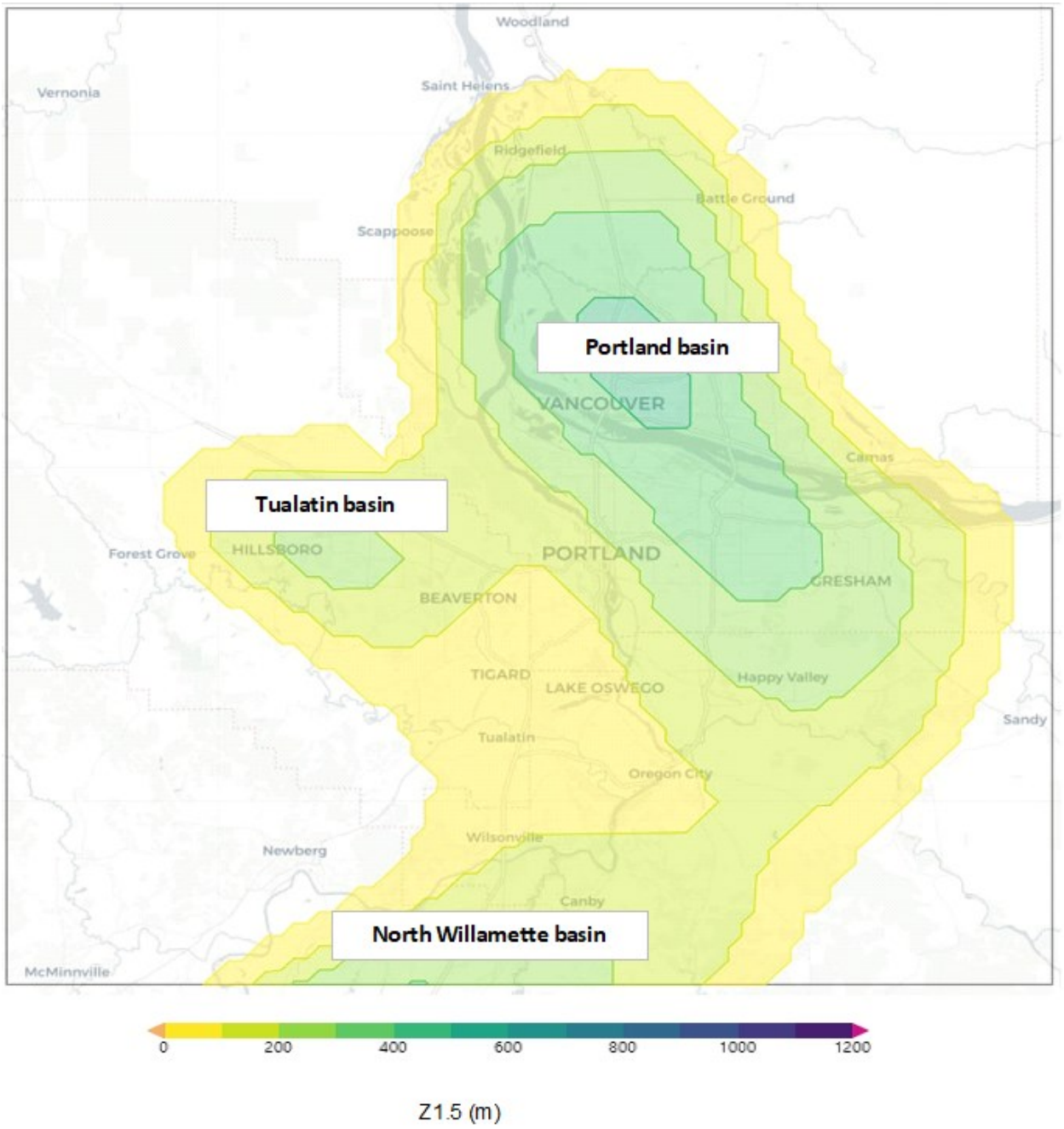

Figure 2.1: $Z_{1.5}$ Depths for the three basins in northwest Oregon.

Table 2.1: Summary of Selected Coordinates for Analysis.

Designation	Latitude (degrees)	Longitude (degrees)	Basin	$Z_{2.5}$ (m)
PDX IN	45.58	-122.49	Portland	1,815
PDX OUT	45.83	-122.49	Outside Portland	NA
TUA IN	45.52	-122.92	Tualatin	2,012
TUA OUT	45.67	-122.92	Outside Tualatin	NA
NWB IN	45.11	-122.76	North Willamette	1,709
NWB OUT	44.75	-122.76	Outside North Willamette	NA

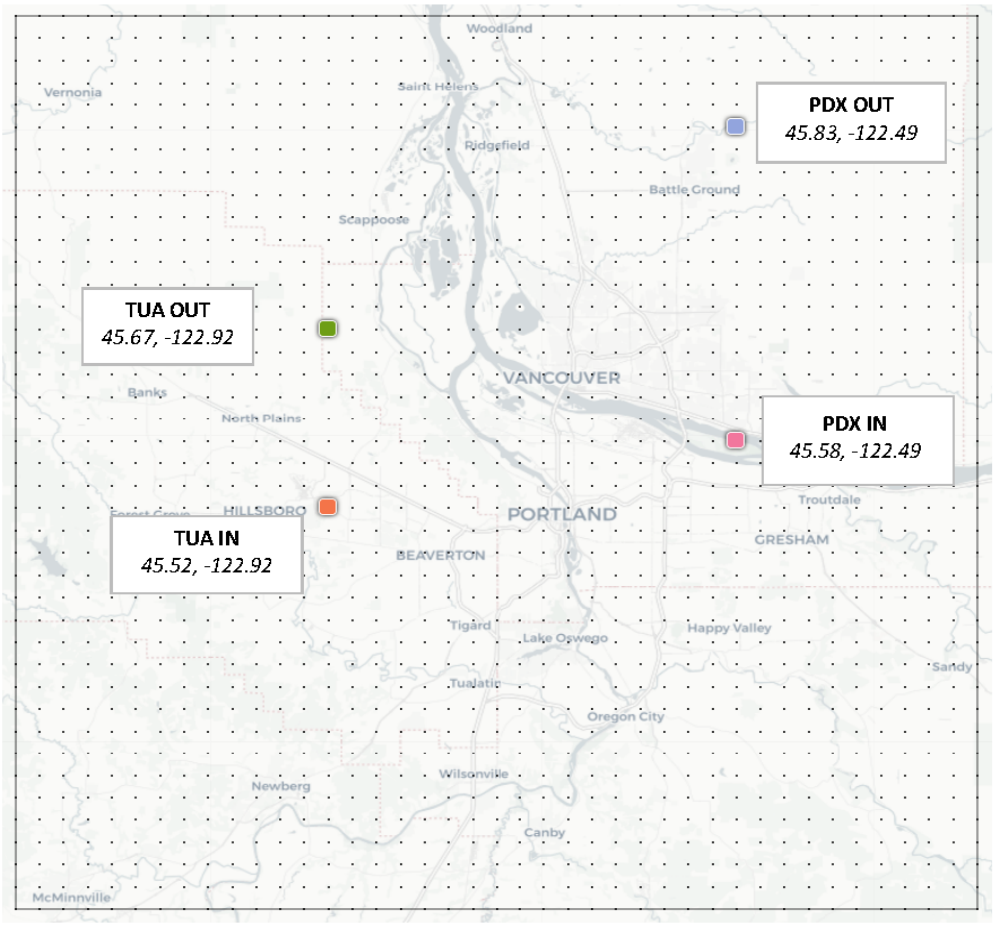

Figure 2.2: Location of M9 input motions—Portland and Tualatin Basins.

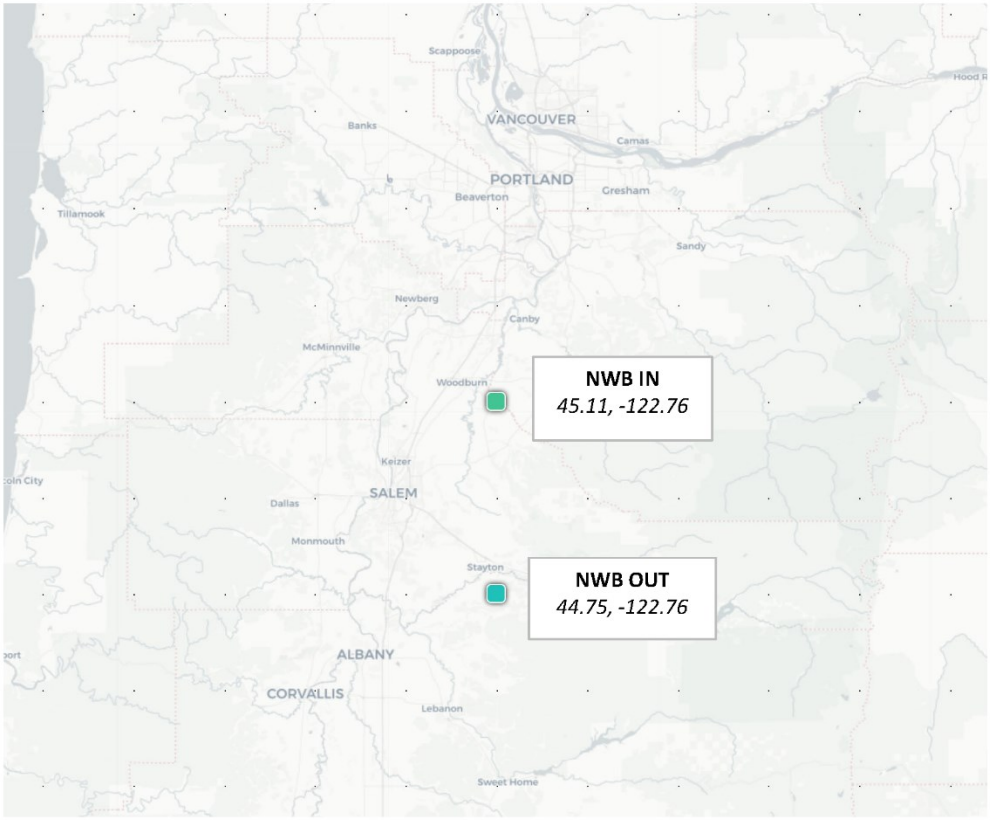

Figure 2.3: Locations of M9 input motions—North Willamette Basin.

The acceleration response spectra of the input rock motions are presented in Figure 2.4 through Figure 2.9 for three IN locations and three OUT locations considered in this study. These figures include the geometric mean of the 30 M9 realizations and plots of the realizations themselves. The geometric means of the 30 M9 realizations are plotted on the same figure in Figure 2.10 for comparison. It is clear from this figure that the spectral coordinates of the motions inside basins are noticeably larger than those outside the basins for periods ranging 1 sec to 4 sec. Figure 2.11, Figure 2.12, Figure 2.13, Figure 2.14, Figure 2.15, and Figure 2.16 present acceleration time histories of the 30 M9 realizations in shades of blue for each of the six coordinates. While the realizations are not labeled and most are not visible, the plots give an overall idea of the range of accelerations covered by the individual motions.

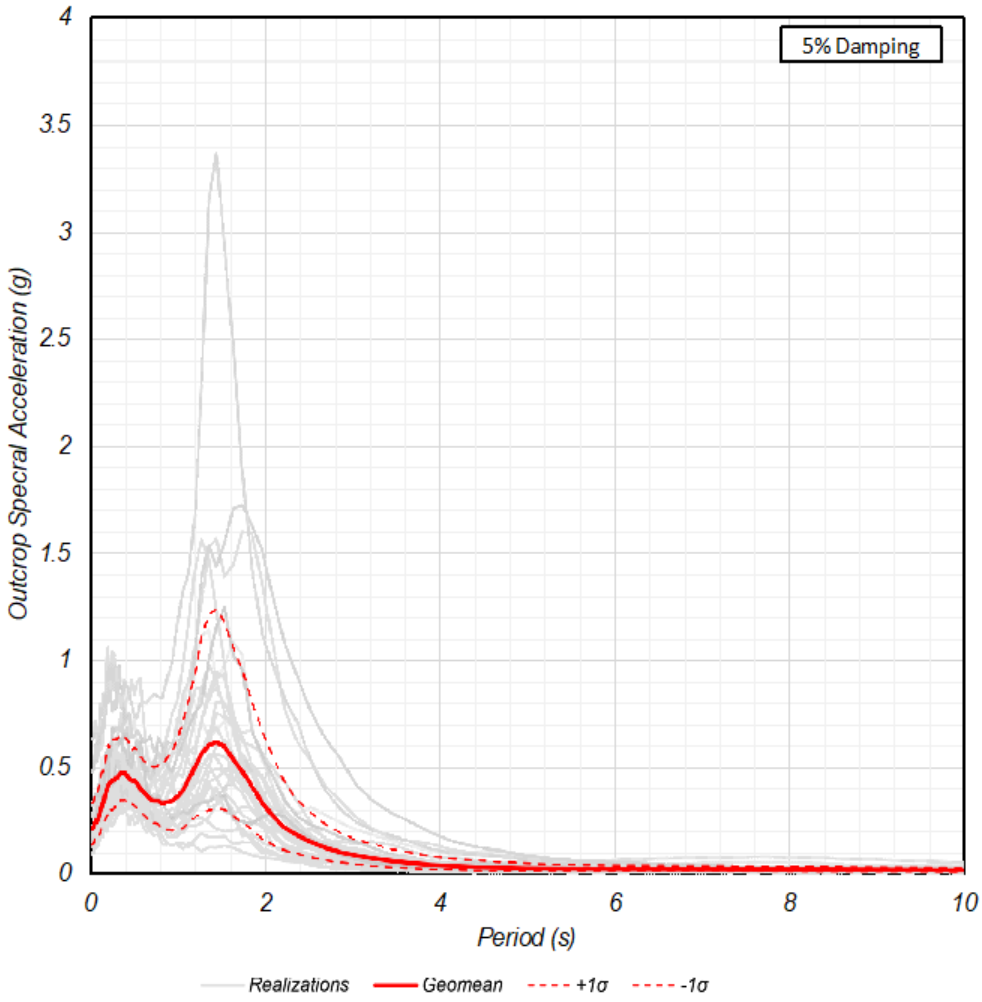

Figure 2.4: PDX IN (45.59, -122.49) input motion response spectra—Outcrop.

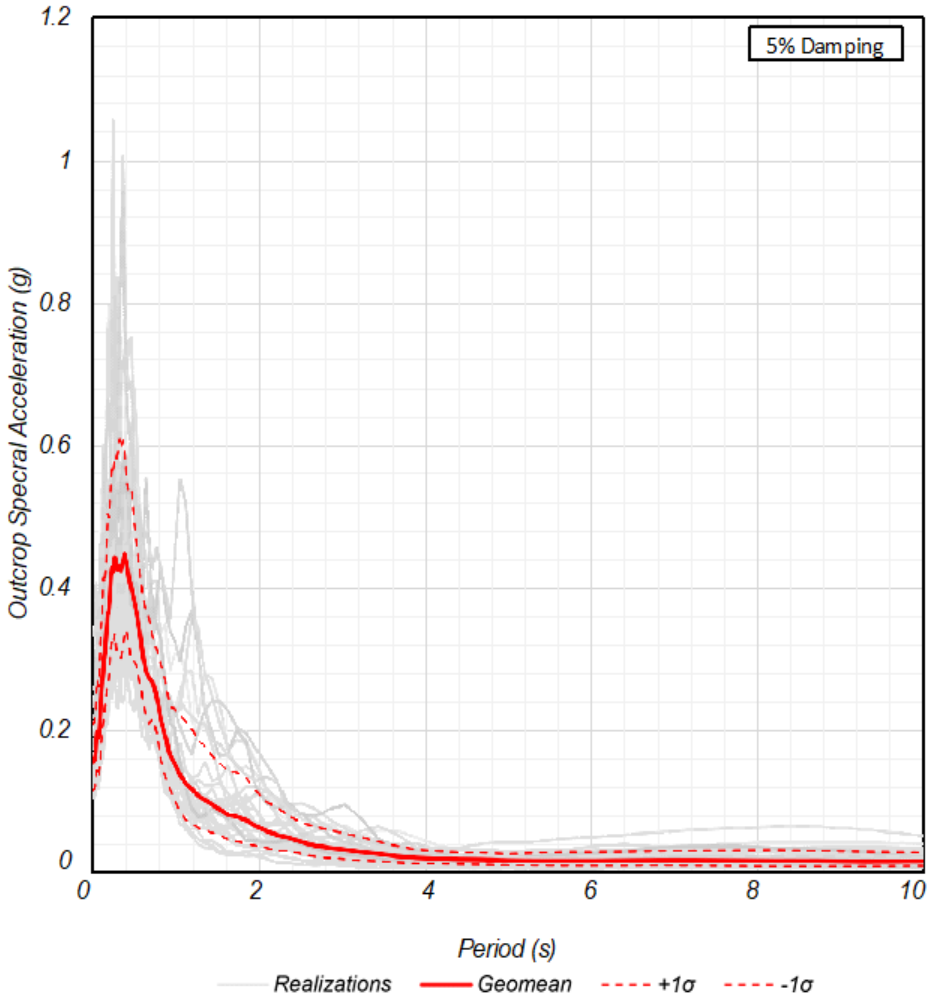

Figure 2.5: PDX-OUT (45.83, -122.49) response spectra of input motions—Outcrop.

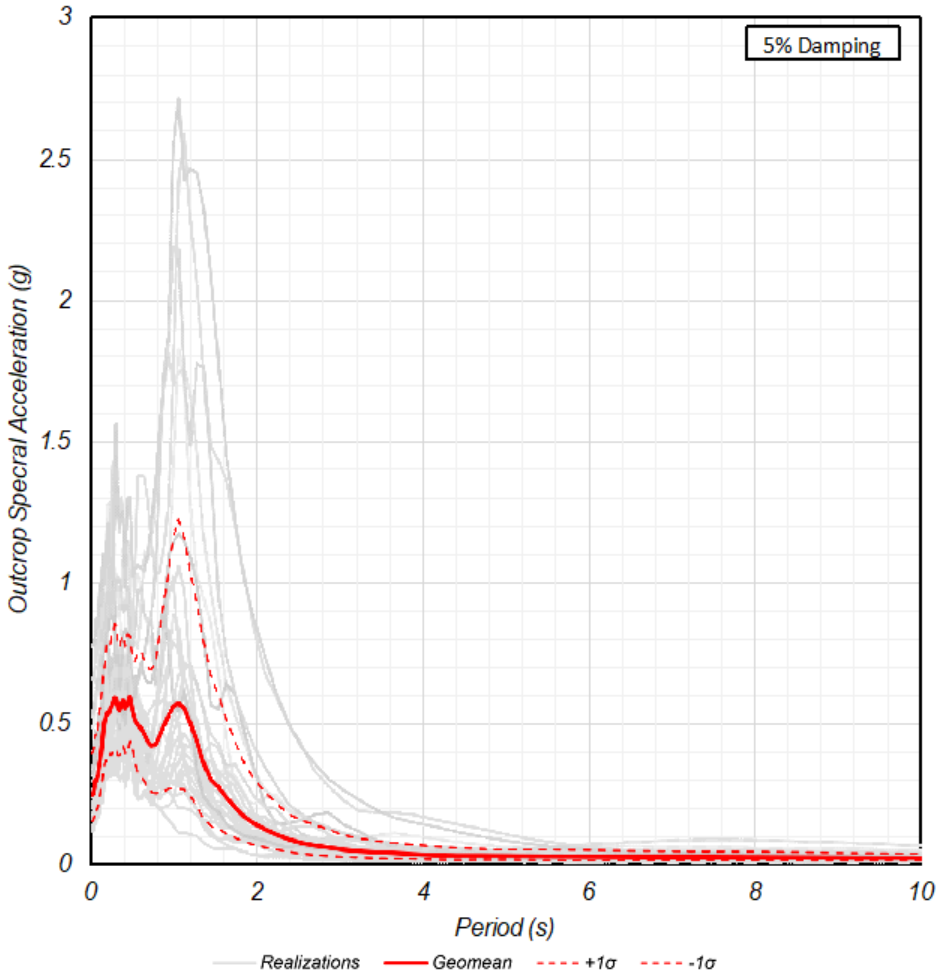

Figure 2.6: TUA-IN (45.52, -122.92) response spectra of input motions—Outcrop.

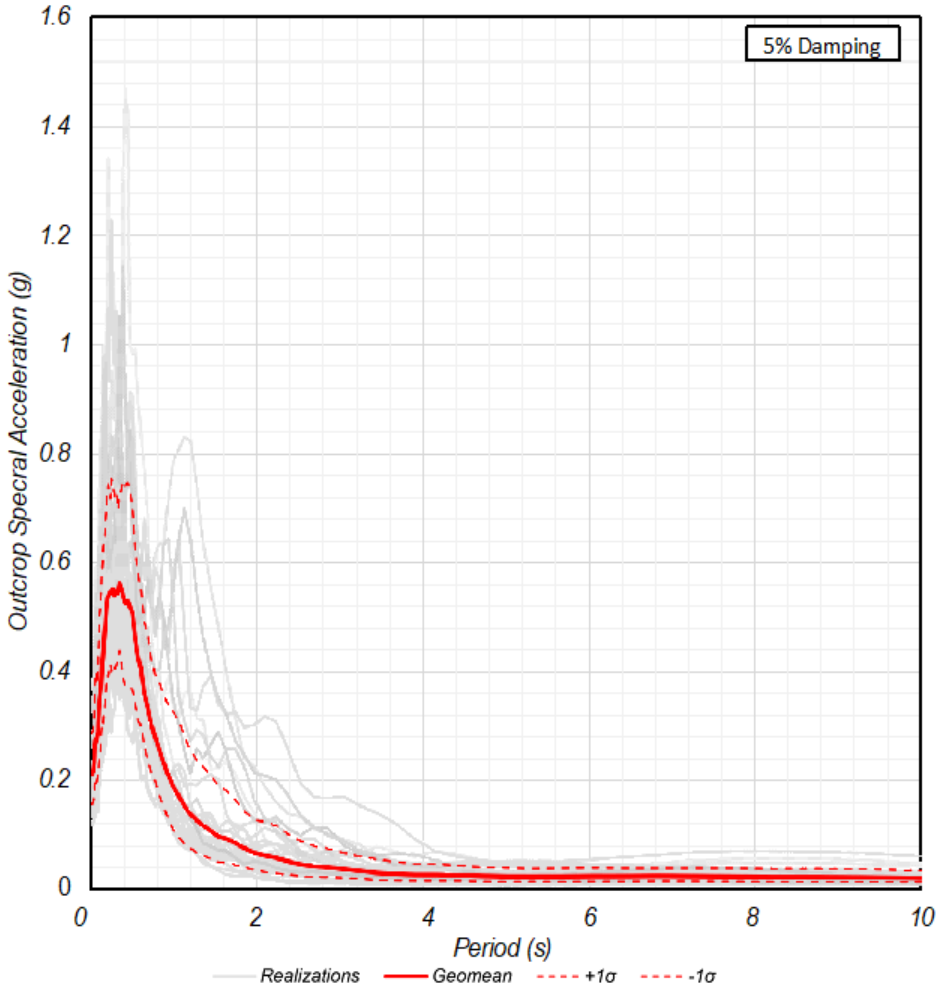

Figure 2.7: TUA-OUT (45.67, -122.92) response spectra of input motions—Outcrop.

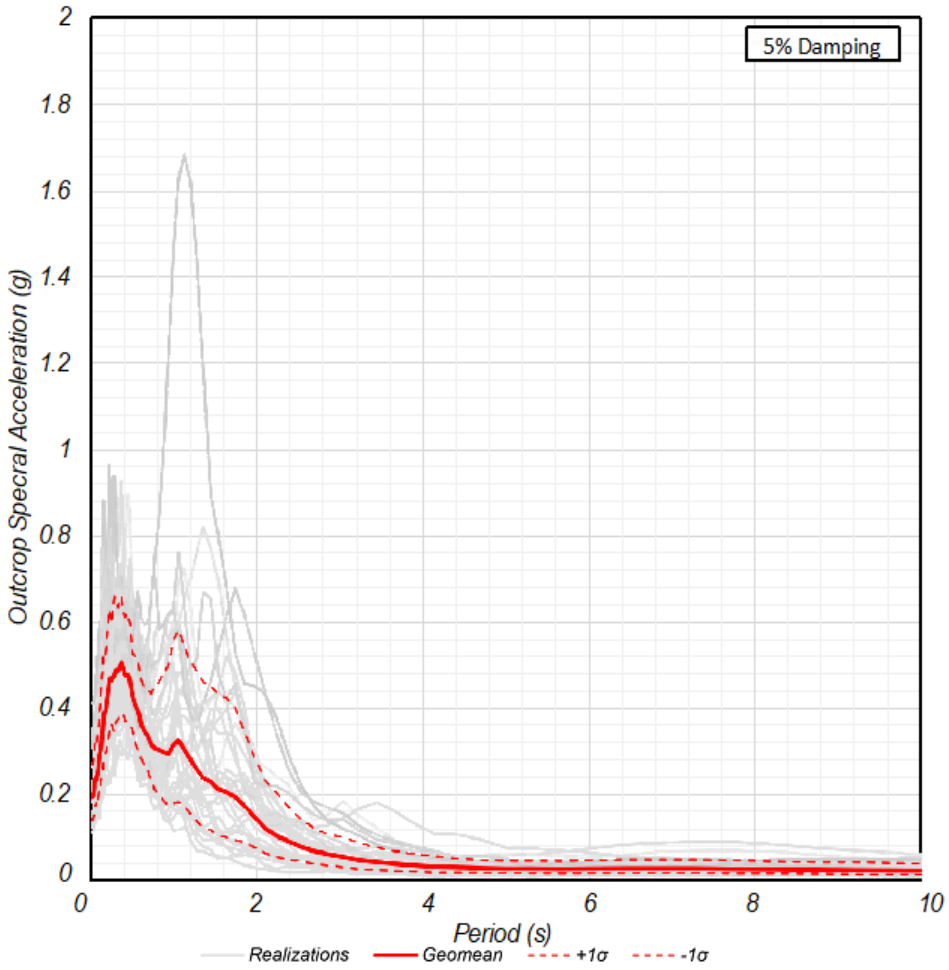

Figure 2.8: NWB-IN (44.75, -122.76) response spectra of input motions—Outcrop.

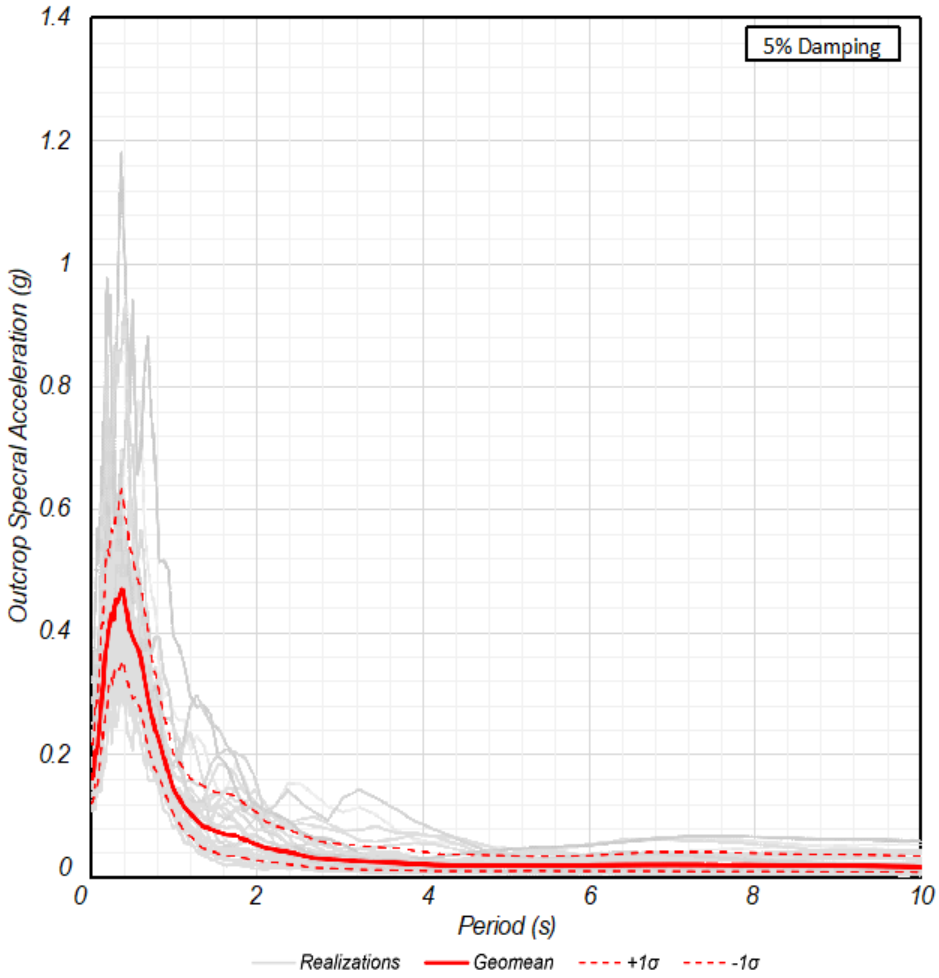

Figure 2.9: NWB-OUT (45.11, -122.76) response spectra of input motions—Outcrop.

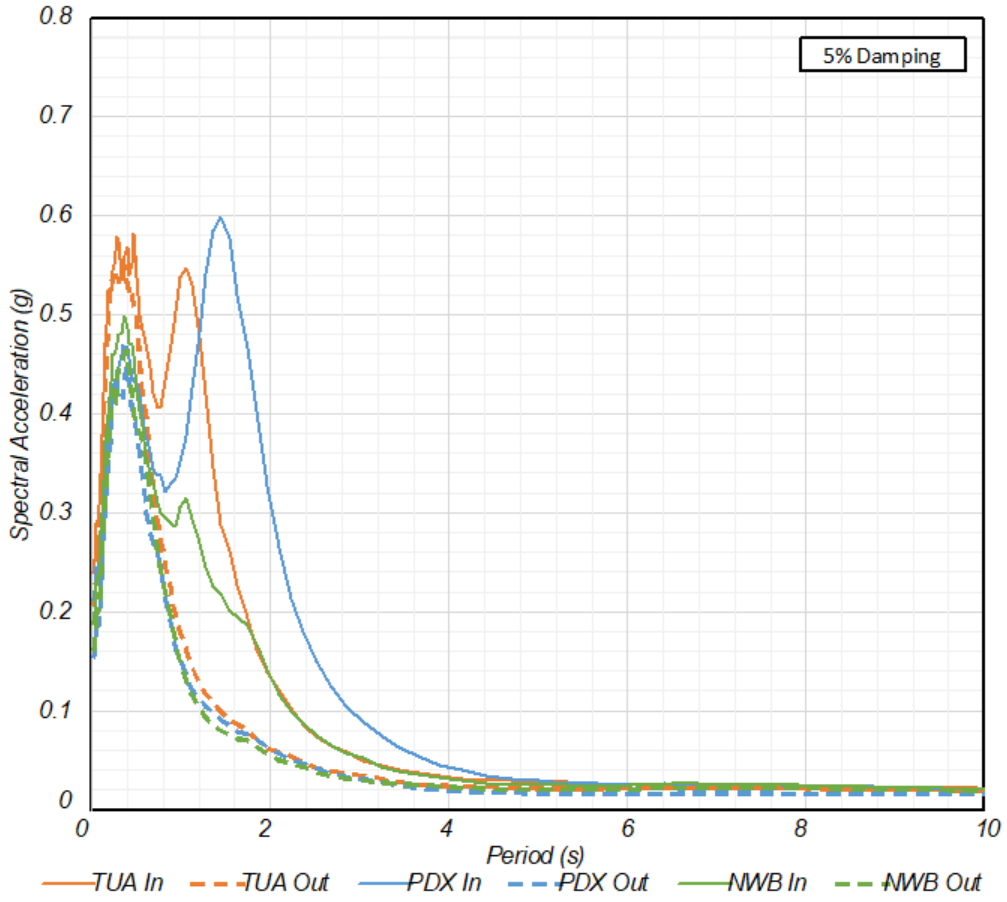

Figure 2.10: Geometric means of response spectra of input motions for each of the six sites (geometric means of 30 M9 realizations at each site).

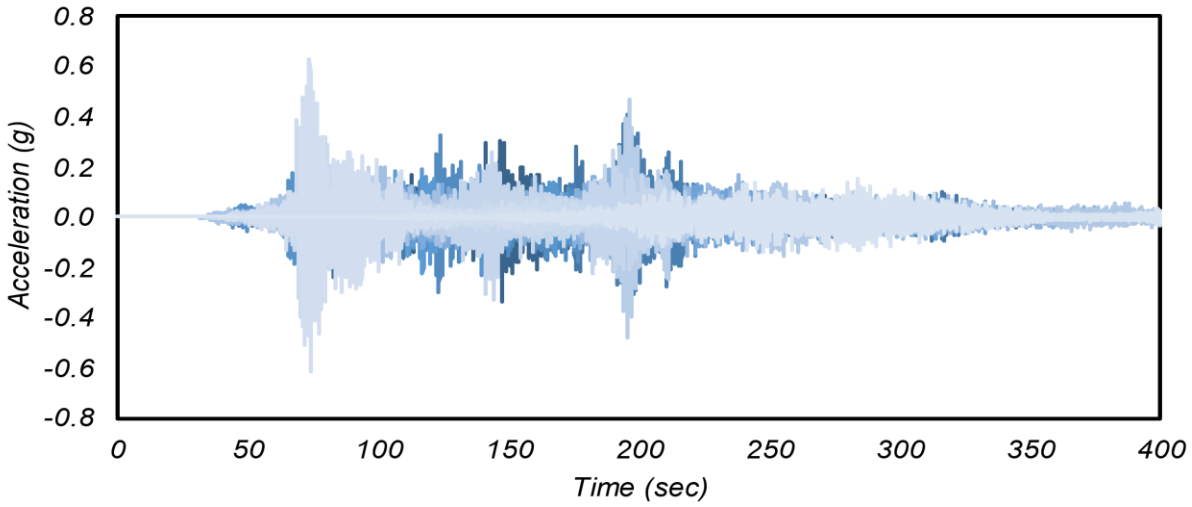

Figure 2.11: PDX IN (45.58, -122.49) superimposed input rock ground motion time histories for all 30 M9 realizations.

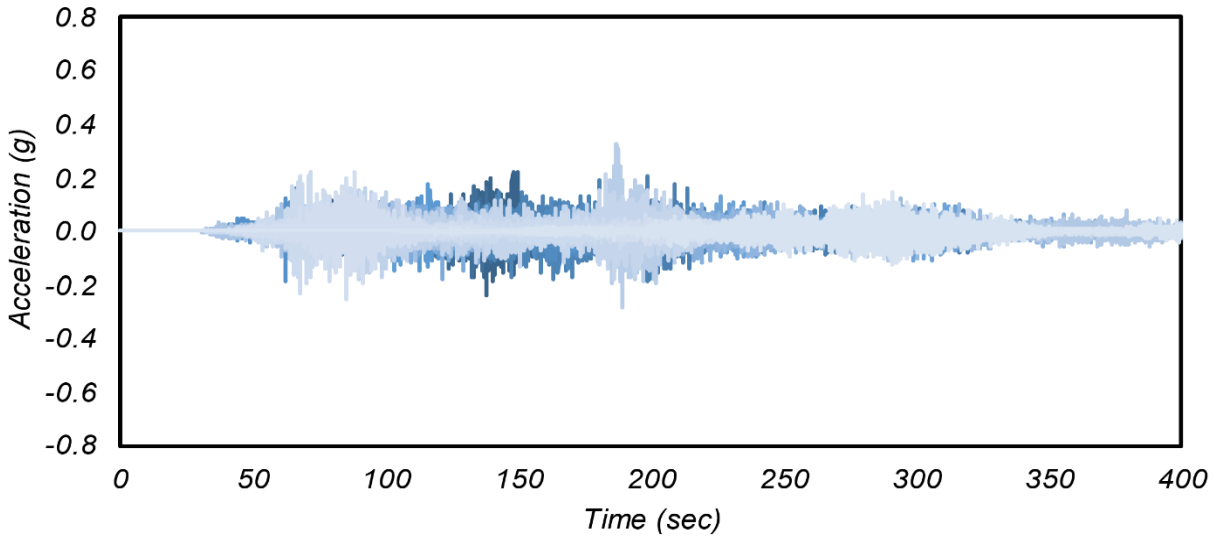

Figure 2.12: PDX OUT (45.83, -122.49) superimposed input rock ground motion time histories for all 30 M9 realizations.

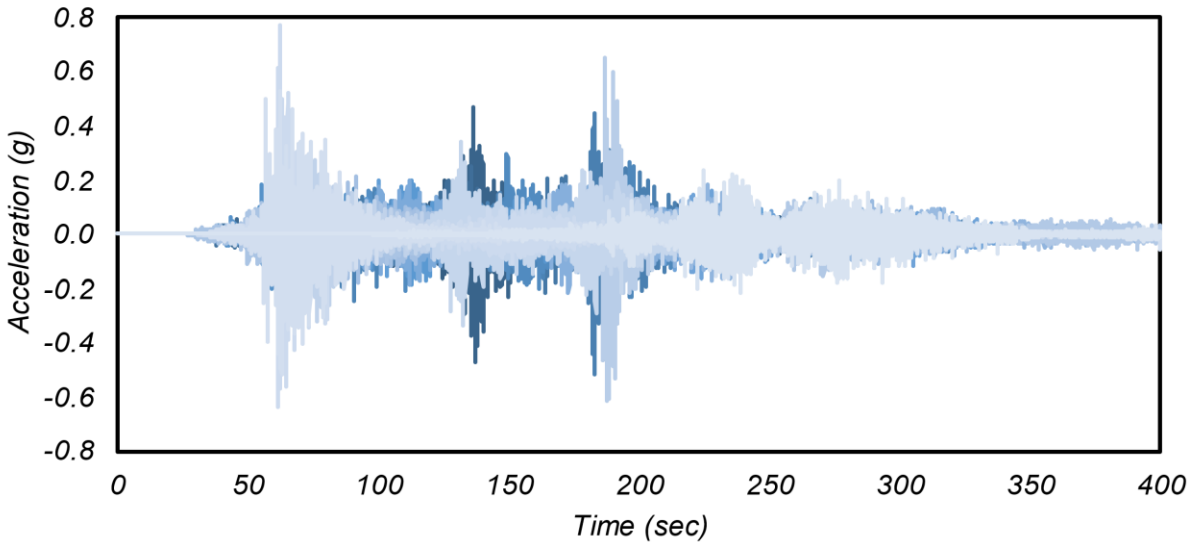

Figure 2.13: TUA IN (45.52, -122.92) superimposed input rock ground motion time histories for all 30 M9 realizations.

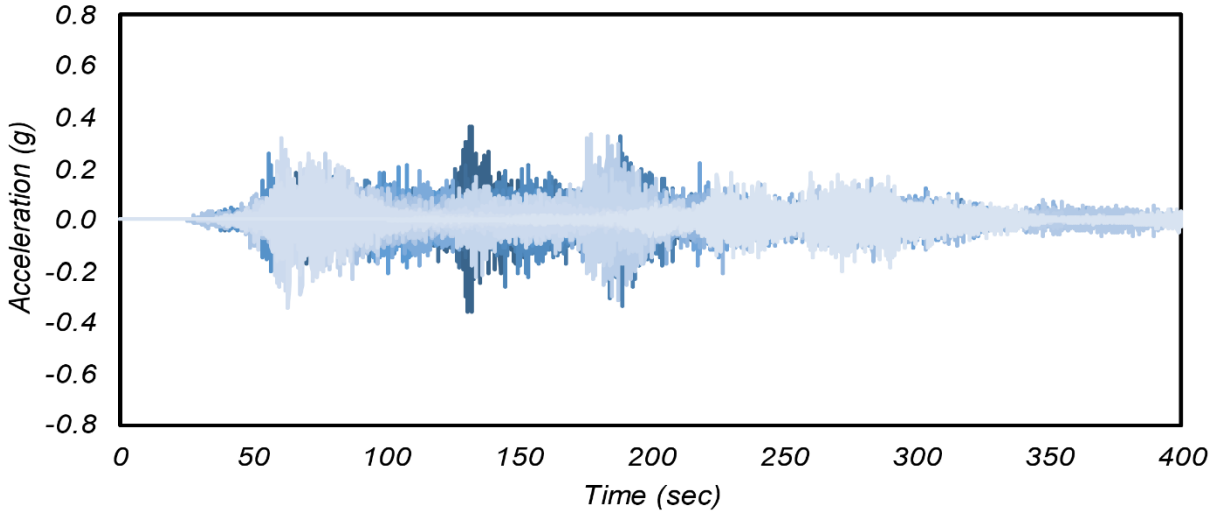

Figure 2.14: TUA OUT (45.67, -122.92) superimposed input rock ground motion time histories for all 30 M9 realizations.

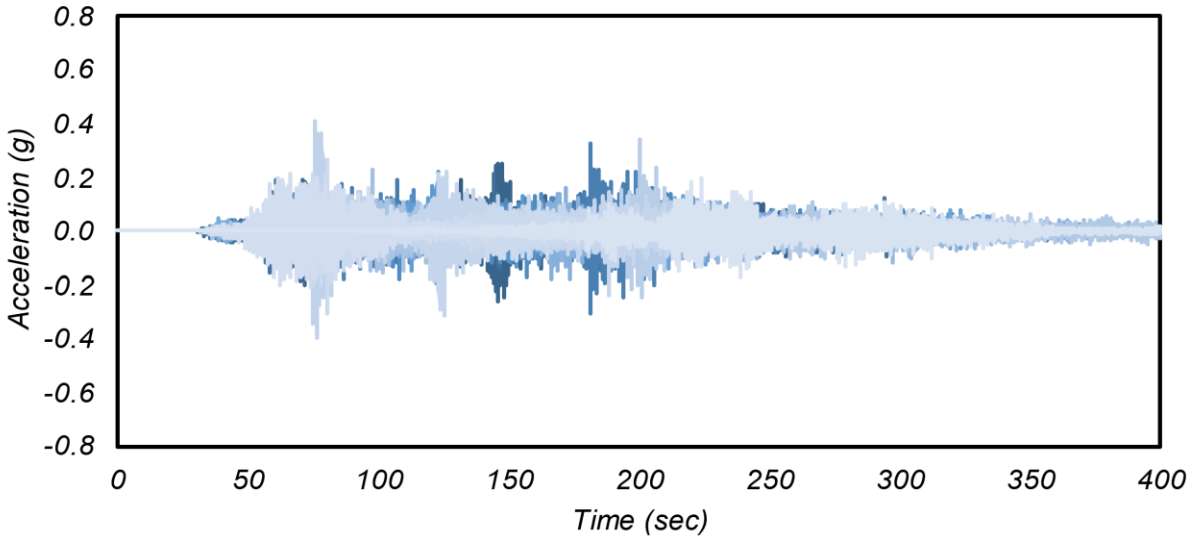

Figure 2.15: NWB IN (45.11, -122.76) superimposed input rock ground motion time histories for all 30 M9 realizations.

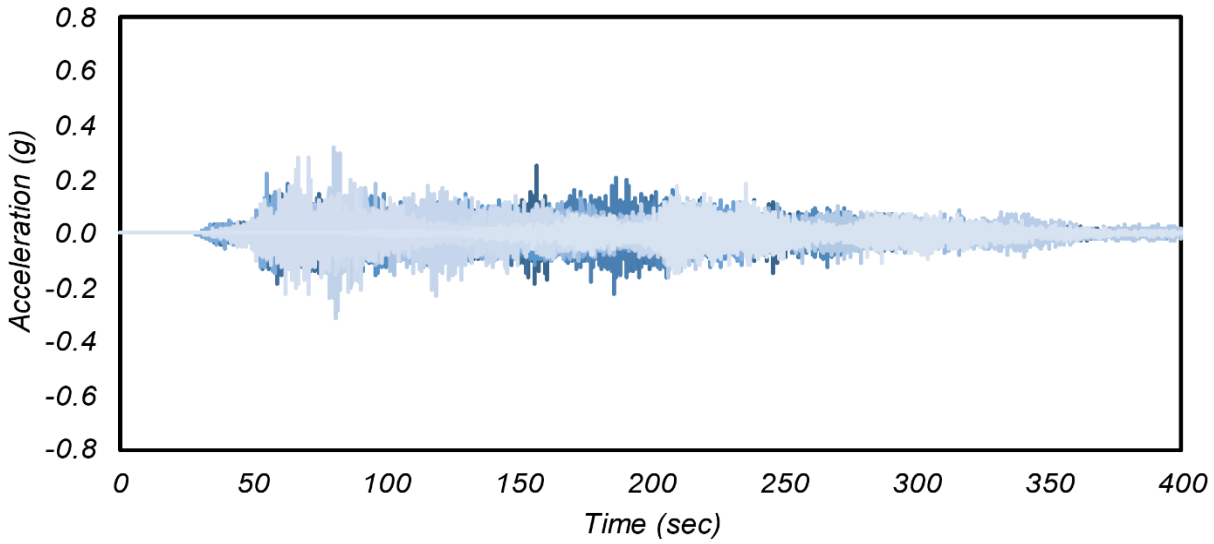

Figure 2.16: NWB OUT (44.75, -122.76) superimposed input rock ground motion time histories for all 30 M9 realizations.

2.2 BASIN AMPLIFICATION RATIOS

For this study, the basin amplification ratio is defined as the ratio of the inside basin bedrock spectral acceleration values to the outside basin bedrock spectral acceleration values.

$$\textbf{basin amplification ratio} = \frac{\textbf{bedrock } S_{a,in}}{\textbf{bedrock } S_{a,out}} \quad \textbf{(2-1)}$$

Figure 2.17, Figure 2.18, and Figure 2.19 present the basin amplification ratios of the three basins. The basin amplification ratios are calculated for all 30 M9 realizations and the geometric mean of all realizations at each coordinate location. Figure 2.20 compares the geometric mean basin amplification ratios for the three basins where the peak amplification ratios range from approximately 3 to 7 for periods ranging between 1.3 sec and 1.7 sec. These basin amplification factors should be used considering the range of ratios estimated from other studies. While the ratios calculated in this study are larger than the basin amplification ratios estimated using empirical correlations by Campbell and Bozorgnia (2014) that are incorporated in NGA-West2 GMM models, other studies (e.g., Frankel and Grant 2021) have also reported basin amplification ratios as high as 7 using recorded earthquakes at seismic stations within Portland and Tualatin basins. These studies are described in the next section.

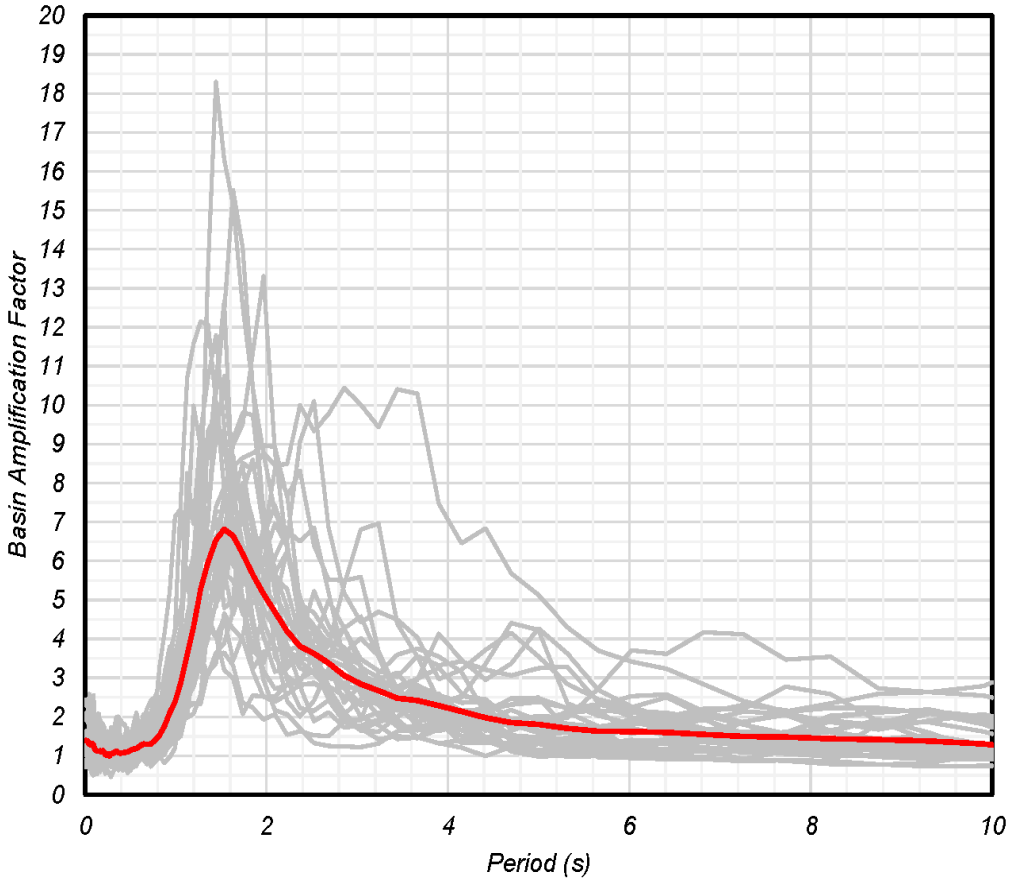

Figure 2.17: Basin amplification ratios of bedrock input motions for Portland Basin.

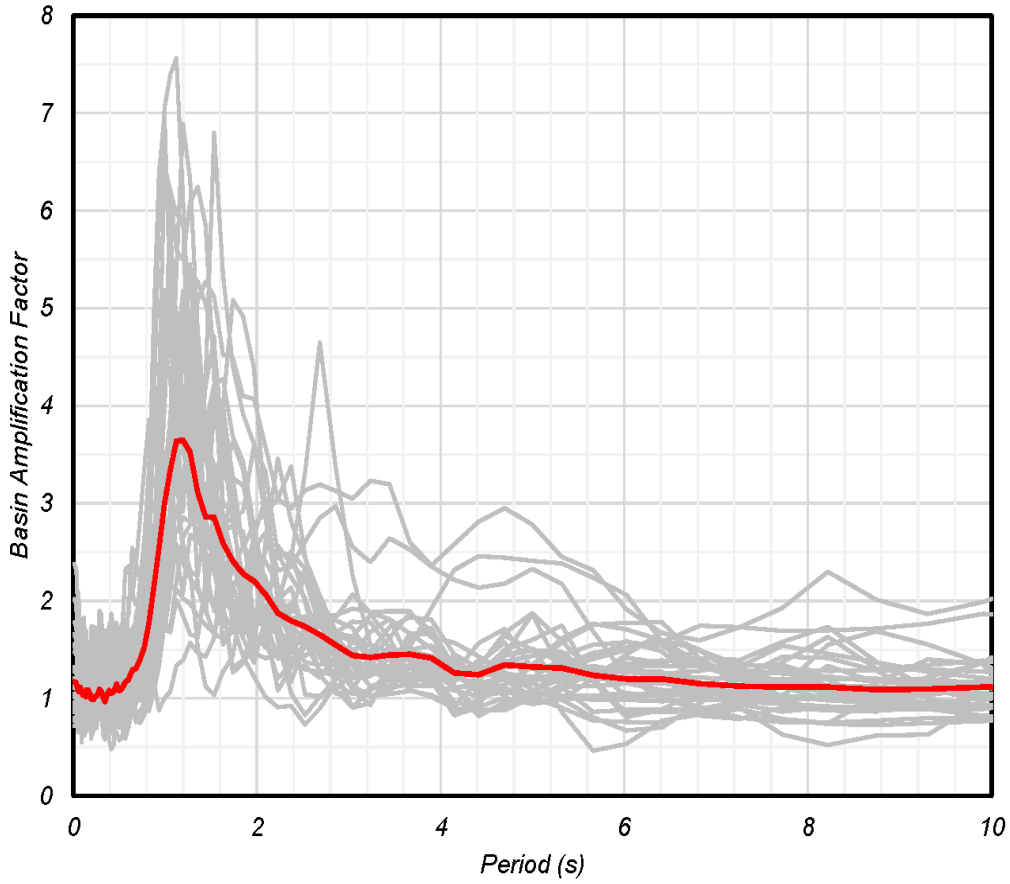

Figure 2.18: Basin amplification ratios of bedrock input motions for Tualatin Basin.

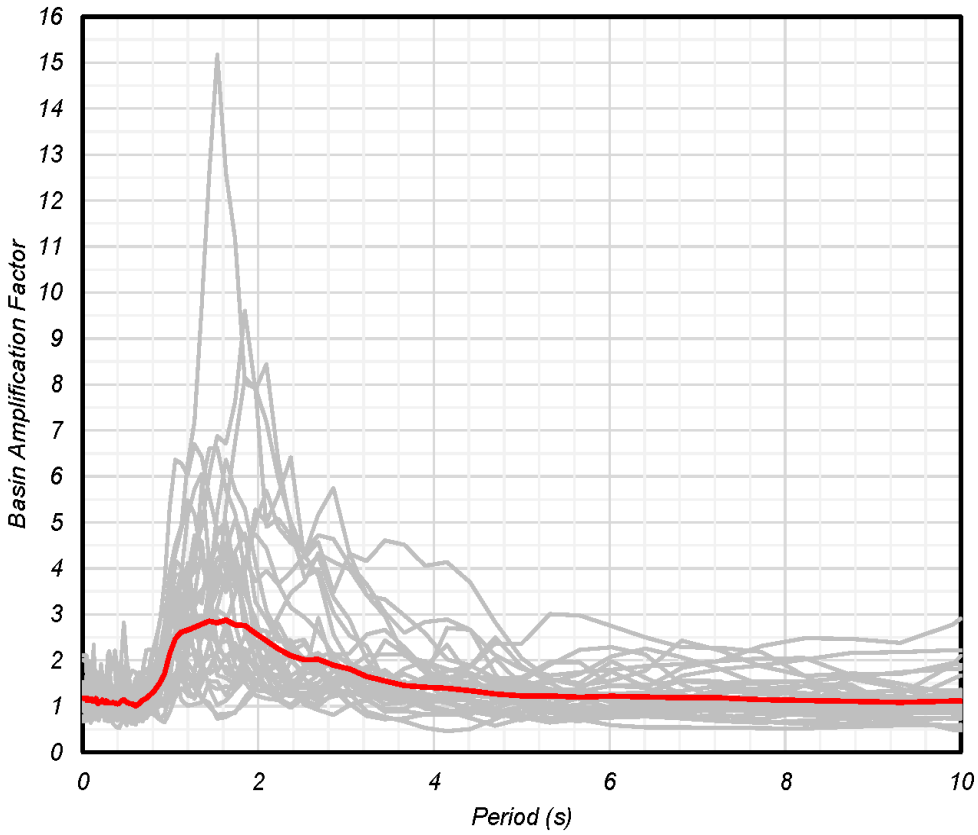

Figure 2.19: Basin amplification ratios of bedrock input motions for North Willamette basin.

It is also important to note that the spatial distribution of the basin amplification ratios within the basins. The ratios reported in Figure 2.20 are the largest amplifications that are calculated within each basin. The spatial distribution of amplification ratios within the Portland and Tualatin basins are shown in Figure 2.21. This figure shows the mean basin amplification ratio (mean of 30 realizations) at a period of 1.65 sec corresponding to the approximate period at which the peak amplification ratio occurs. While there are areas within the Portland basin that experience basin amplification ratios as high as 7, the ratios are smaller over the larger basin area. It is recommended that the basin amplification factors characterized in this study be considered in combination with the results from other studies using empirical methods such as those in NGA-West2 (Campbell & Bozorgnia, 2014) and Frankel and Grant (2021).

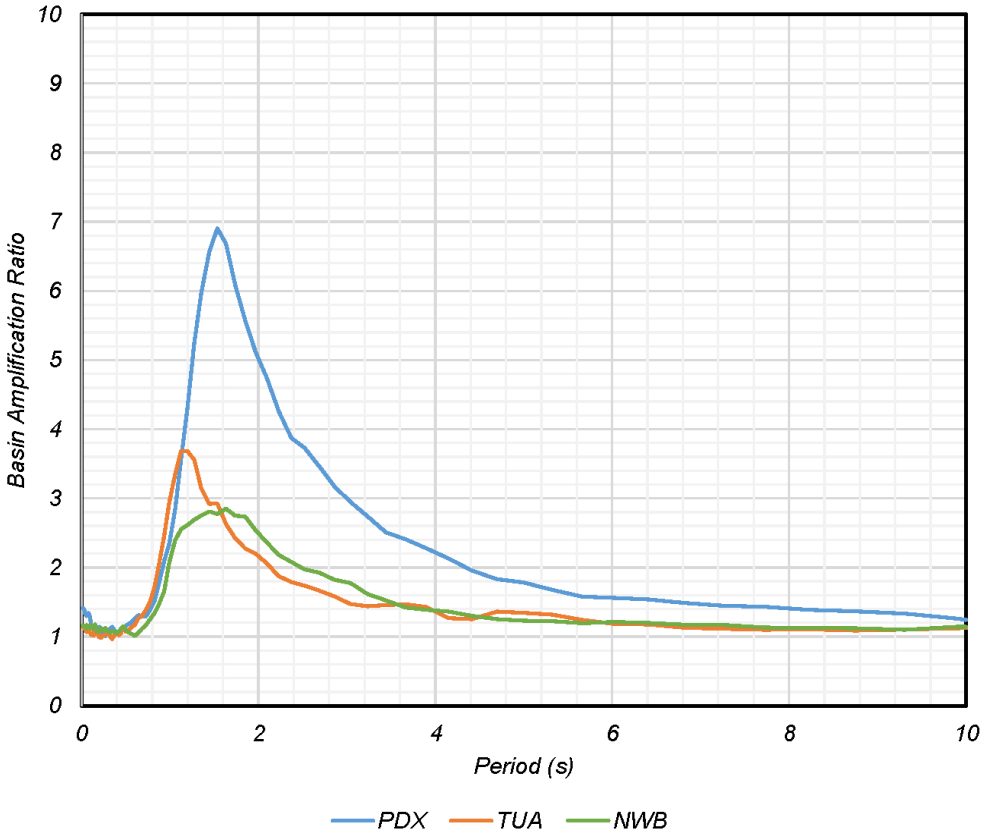

Figure 2.20: Basin amplification ratios of outcrop motions using geometric means of 30 M9 realizations.

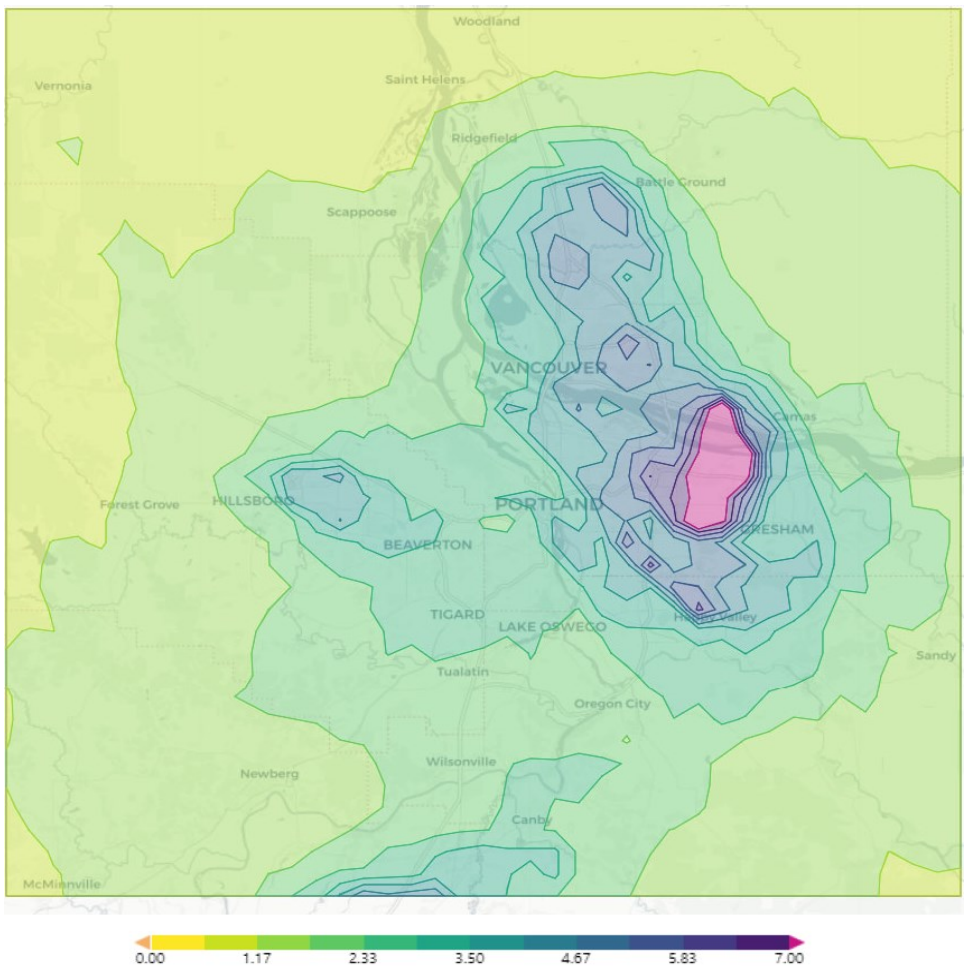

Figure 2.21: Map of basin amplification ratios of outcrop motions using geometric means of 30 M9 realizations at period of 1.65 sec.

2.3 COMPARISON WITH OTHER STUDIES

Numerous studies have demonstrated that geologic basins can amplify seismic waves, and several GMMs now incorporate basin effects into the model, typically via correlation with Vs_{30} or $Z_{2.5}$. GMM documentation and basin effects studies relevant to this project are briefly summarized below.

Frankel and Grant (2021) calculated basin amplification ratios in Portland and Tualatin basins using accelerometer recordings from recent earthquakes. They calculated basin amplification ratios between 1 and 6 for Portland basin and between 2.5 and 7 for Tualatin basin. Their basin amplification ratios are shown in Figure 2.22.

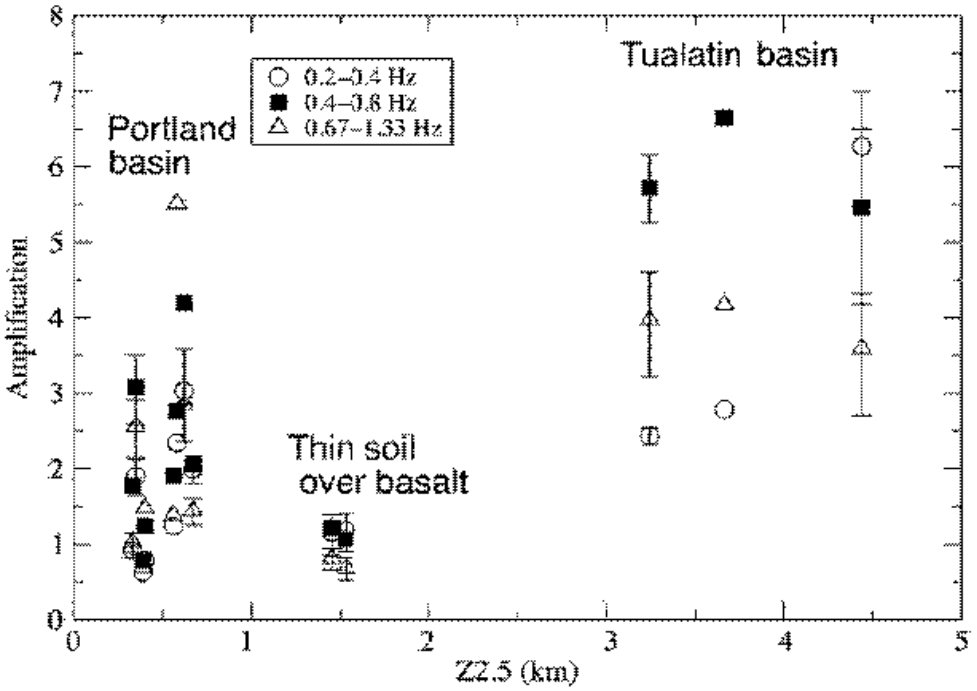

Figure 2.22: Basin amplification ratios for Portland and Tualatin Basins from recorded accelerometers by Frankel and Grant (2021).

Basin effects in the Next Generation Attenuation – West 2 (NGA-West 2) GMMs are correlated with $Z_{2.5}$ (Campbell & Bozorgnia, 2014) or $Z_{1.0}$ (Abrahamson et al., 2014; Boore et al., 2014; Chiou & Youngs, 2014). During a workshop on incorporating basin effects in the design of tall buildings in the Puget Sound (Chang et al., 2014) Ken Campbell reported that deep basin amplification terms in the Campbell and Bozorgnia (2014) model averaged a factor of about 2. Figure 2.23 shows the basin amplification factors by Campbell and Bozorgnia (2014) for different periods and $Z_{2.5}$ values as reported by Marafi et al. (2017).

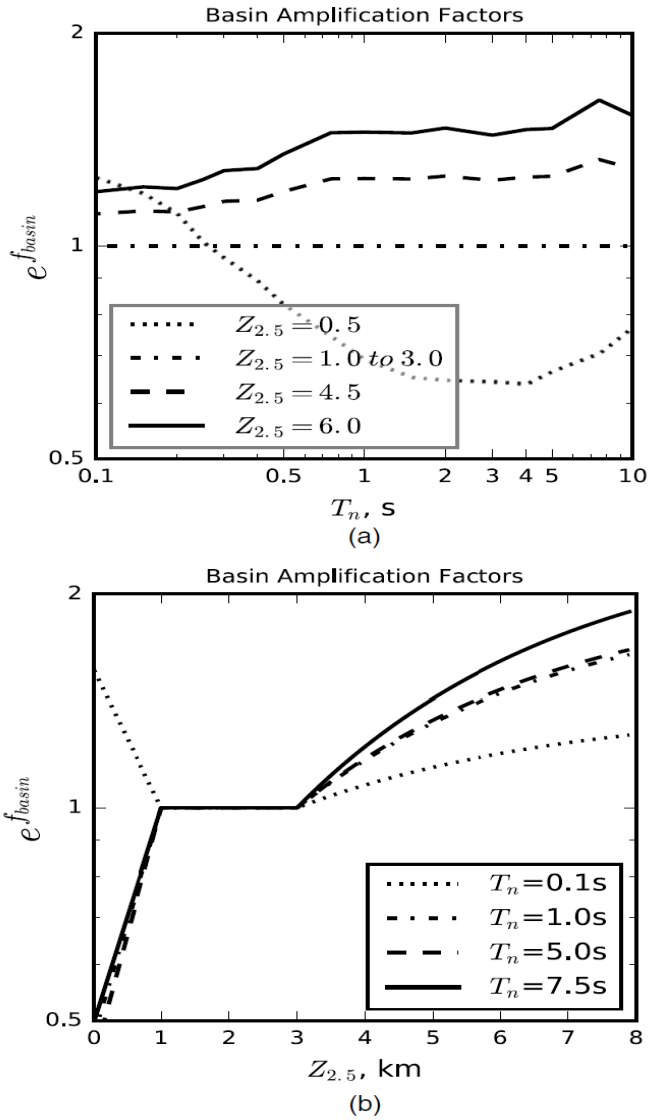

Figure 2.23: Basin amplification ratios by Campbell and Bozorgnia (2014) model that was incorporated in NGA-West2 (figure created by Marafi et al. 2017).

The 2014 National Seismic Hazard Maps (NSHM) (Petersen, 2014) did not consider basin effects directly in the calculations for the western U.S. seismic model. For the 2018 NHSM update, the NGA West 2 GMMS were used to develop the western U.S. seismic model. Four urban basin regions were specifically included in the model (Petersen et al., 2020), however the Portland area was not included as one of the four regions.

The Next Generation Attenuation – Subduction (NGA-Sub) is a recently developed earthquake ground-motion database, as well as a suite of GMMs for global subduction zone earthquakes. These GMMs include period-dependent basin sediment-depth models to account for basin amplification. In Cascadia, the GMMs were developed using the basins identified in Figure 1.1, with estimates of the basin depth based on models by Stephenson et al. (2017).

Pratt et al. (2003) and Pratt & Brocher (2006) studied recordings of local earthquakes from stations in Puget Lowland basins. Compared to reference bedrock sites outside of the Puget Lowland, the peak amplifications ranged from 2 to 6. They noted that amplification decreased with increasing frequency.

Frankel et al. (2009) recognized that basin effects were observed in Seattle during the M_w 6.8 2001 Nisqually Earthquake. Figure 2.24 shows the basin amplification ratios ranging between 2 to 4 as reported by Chang et al. (2014). Previous research demonstrated that large amplifications ranging from 3 to 7, which are likely the result of basin surface-waves, were possible in the Seattle area. The authors performed a series of 3D earthquake simulations that predicted many of the features observed in real seismograms, including the observed basin effects and amplifications.

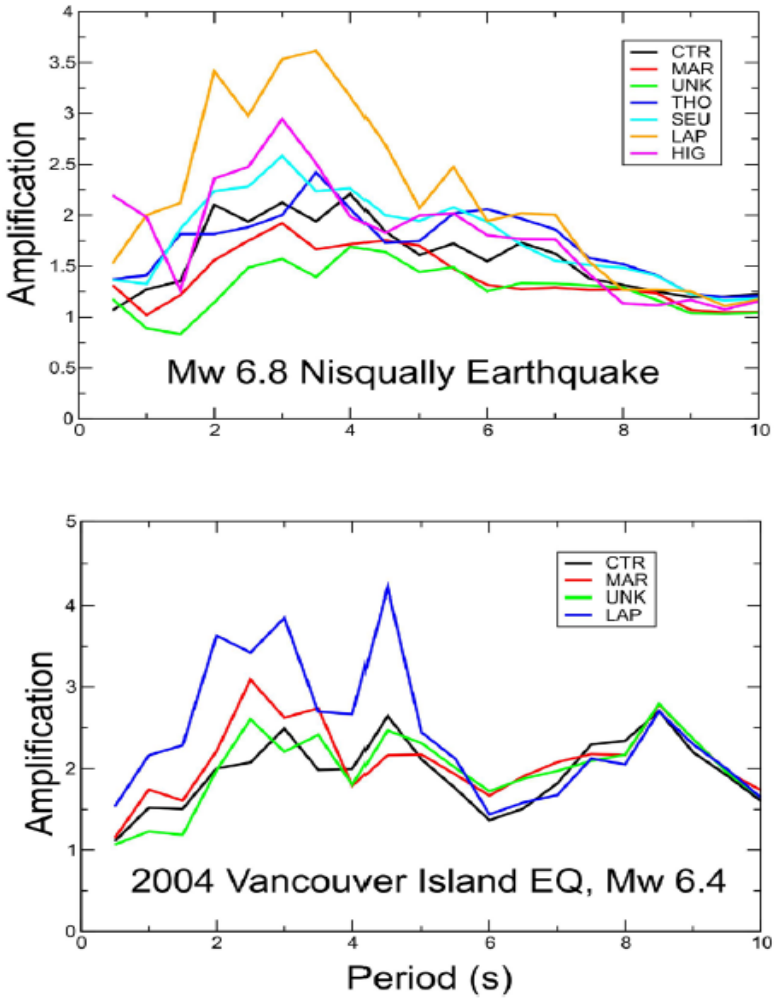

Figure 2.24: Basin amplification ratios for sites within the Seattle Basin from 2011 Nisqually and 2004 Vancouver Island earthquakes (Chang et al. 2014).

Day et al. (2008) developed a model for basin effects on long-period response spectra based on the analysis of 3D numerical simulations of ground motions for a suite of sixty scenario

earthquakes within the Los Angeles basin region. Using $Z_{1.0}$, $Z_{1.5}$, and $Z_{2.5}$ as predictor variables, the analysis found basin amplification is period dependent, with the highest amplifications occurring for the longest periods and greatest basin depths. Relative to their very hard rock reference site, the maximum observed amplifications were about a factor of 8.

Marafi et al. (2017) evaluated the effects of basins using subduction earthquake recordings from basins in Japan with similar depths to basins near Seattle, Washington. For several basins, spectral accelerations were amplified by factors ranging from 2 to 4 for periods above 2.0 seconds as shown in Figure 2.25.

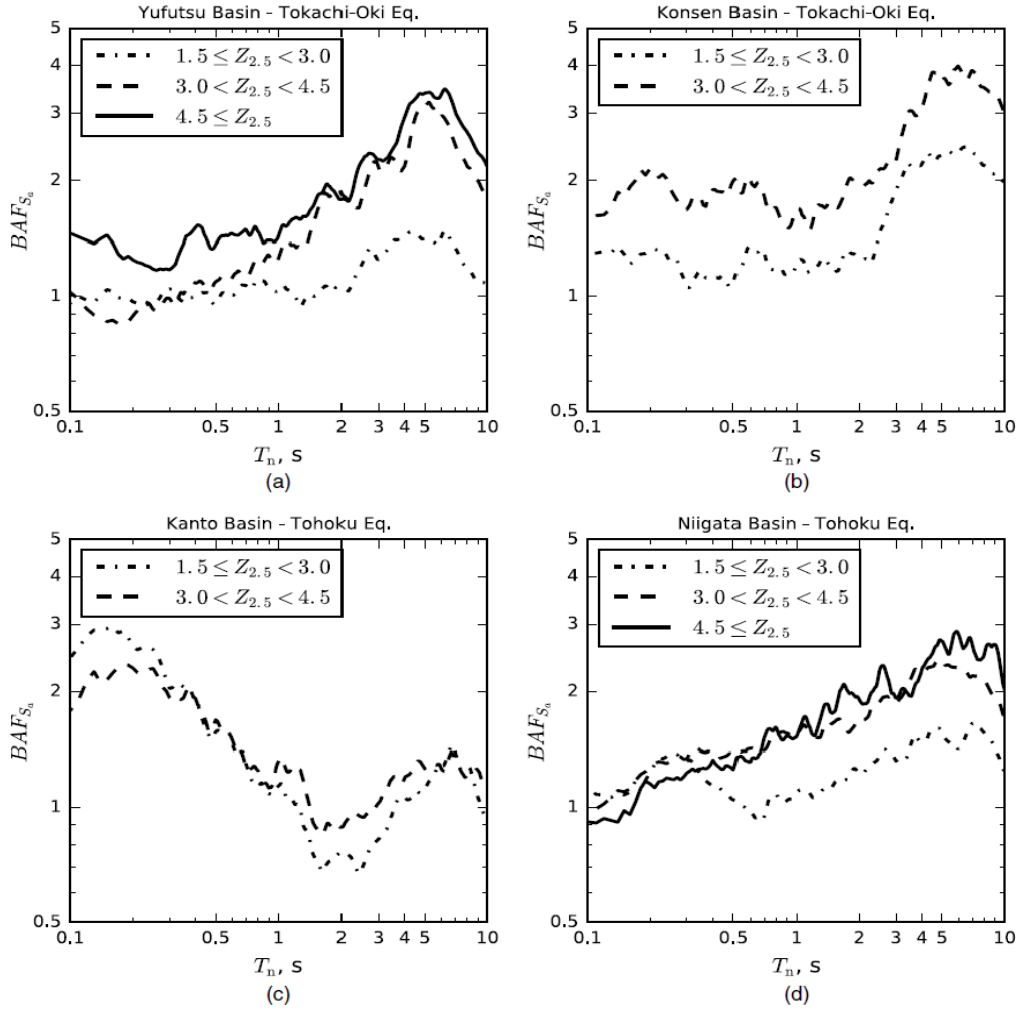

Figure 2.25: Basin amplification factors calculated for basins in Japan by Marafi et al. (2017).

Kakoty et al. (2020) utilized the M9 broadband synthetic motions to develop basin amplification factors for the Georgia Basin in Vancouver, British Columbia. The proposed basin amplification factors reached geometric mean values as high as 4.5 at a 2.0-second period as shown in Figure 2.26.

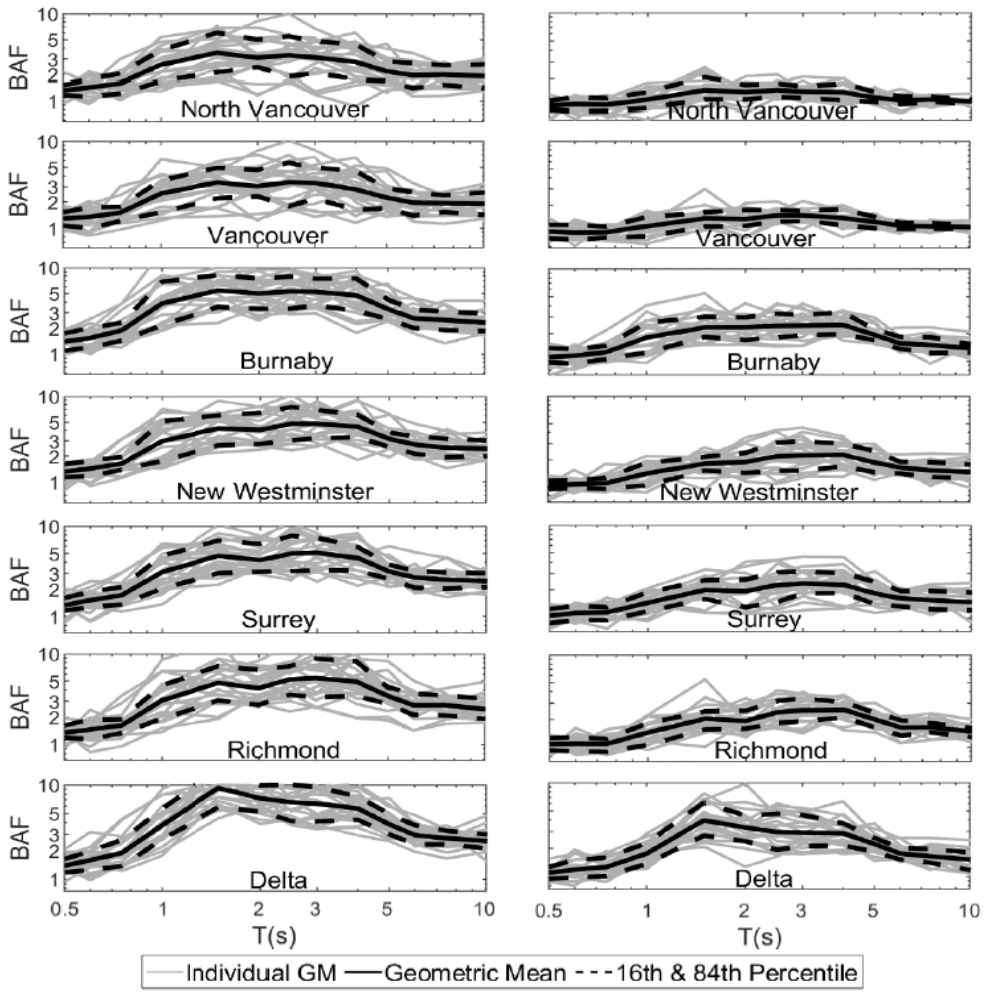

Figure 2.26: Basin amplification factors calculated for Vancouver, B.C. using M9 synthetic motions (Kakoty et al. 2020).

3.0 SOIL PROFILES AND PARAMETERS

Site response analyses were performed to characterize the spectral amplification ratios due to propagation of seismic waves in surficial soils (above rock level). The site response analyses were performed for idealized subsurface profiles representing a range of soil Site Classes from C to E. The soil profiles were developed based on data from three borings (B-1, B-2, and B-3) and their associated testing performed as part of geotechnical investigations for the Critical Energy Infrastructure (CEI) Hub in northwest Portland (Moug et al. 2021). A cross section of the site showing the locations of three borings is presented in Figure 3.1. This location was selected based on the available data and the ability of the site to represent a wide range of site classes using the same units, discussed below.

3.1 SUBSURFACE SOIL AND ROCK UNITS

The general geologic profile at the CEI Hub consists of Fill, underlain by Quaternary alluvium (Qal), followed by weathered Columbia River Basalt (WCRB) grading to fresh Columbia River Basalt (CRB). Table 3.1 presents the static and dynamic parameters used for the site response analyses.

Table 3.1: Subsurface Soil and Rock Parameters for Site Response Analysis.

Unit	Total Unit Weight (kN/m3)	Friction Angle (degrees)	Cohesion (kPa)	Shear Wave Velocity (m/s) or Equation1	Modulus Reduction and Damping Curves
Fill	18.0	33	0.0	182	EPRI
Qal	16.5	33	14.4	y = 2.6x + 136.9	Darendeli, 2001
WCRB	20.4	N/A	N/A	y = 8.8x + 212.8	Modeled as elastic
CRB	20.4	N/A	N/A	800	N/A

3.2 SHEAR WAVE VELOCITY (VS) PROFILES

The shear wave velocity (Vs) profiles were estimated using the Vs model developed by the Oregon Department of Geology and Mineral Industry, DOGAMI (Roe et al. 2013). Figure 3.1 shows the geologic cross-section and location of the three bore holes used to develop the model profiles. Three initial shear-wave velocity profiles were developed using the subsurface units and depths encountered in borings B-1, B-2, and B-3. A further two shear-wave velocity profiles were developed by modifying the parameters of the B-1 and B-3 profiles to correspond to site classes “C” and “E” for the analyses (named profile B-1UB and B-3-LB, respectively). Table 3.2 presents a summary of the five profiles with their corresponding site classes. The shear wave velocities versus depth are plotted for each of the profiles in Figure 3.2.

Table 3.2: Profile Summary.

Profile	Depth to Half-space (m)	Vs_{30} (m/s)	Site Class
B-1UB	11.0	465	C
B-1	11.0	346	C/D
B-2	23.5	217	D
B-3	28.0	189	D/E
B-3LB	28.0	144	E

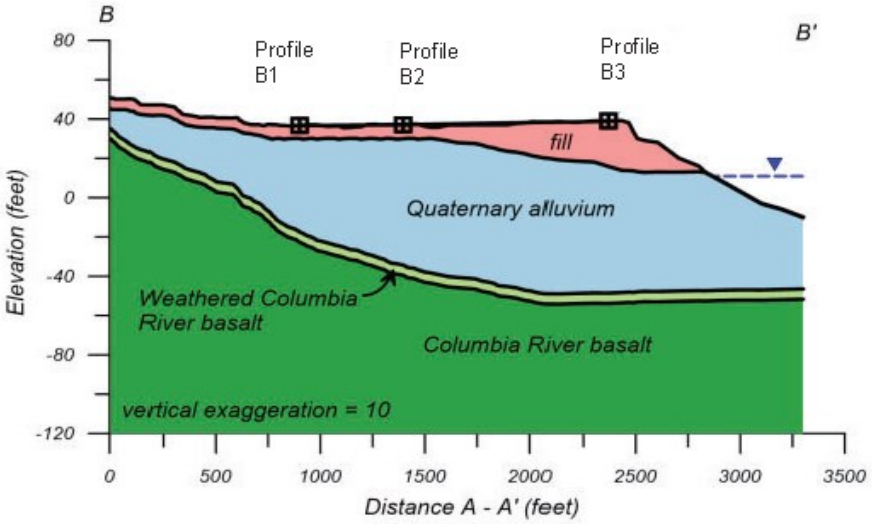

Figure 3.1: Cross-section and location of borings used to develop model shear-wave velocity profiles for analysis.

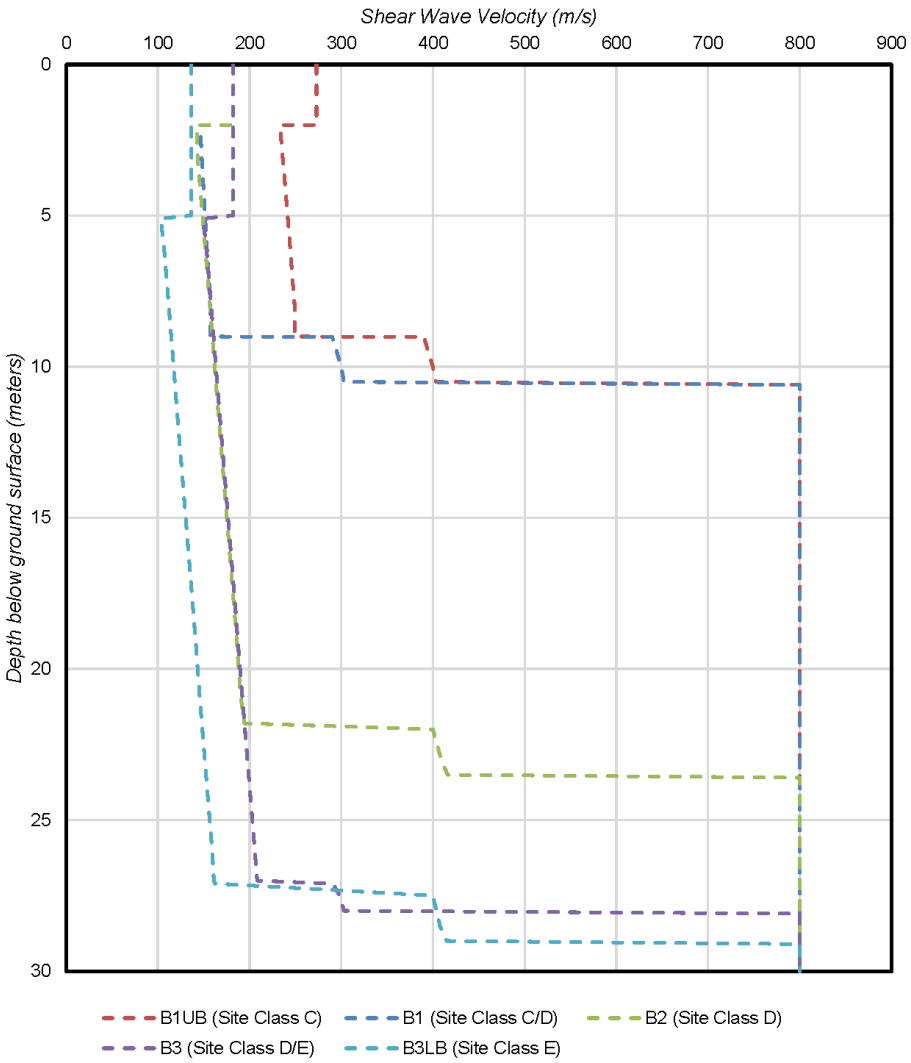

Figure 3.2: Shear-wave velocity profiles.

4.0 SITE RESPONSE ANALYSES

4.1 MODEL GENERATION

Using the subsurface units and profiles discussed in Section 3.0, subsurface models were generated for site response analysis. Each profile was divided by subsurface unit and further subdivided into 0.5- to 1.0-meter layers for analysis. Shear strength and shear wave velocity were calculated for each sublayer using the parameters in Table 3.1. The DEEPSOIL model for each of the four profiles is presented in Figure 4.1, Figure 4.2, Figure 4.3, Figure 4.4, and Figure 4.5.

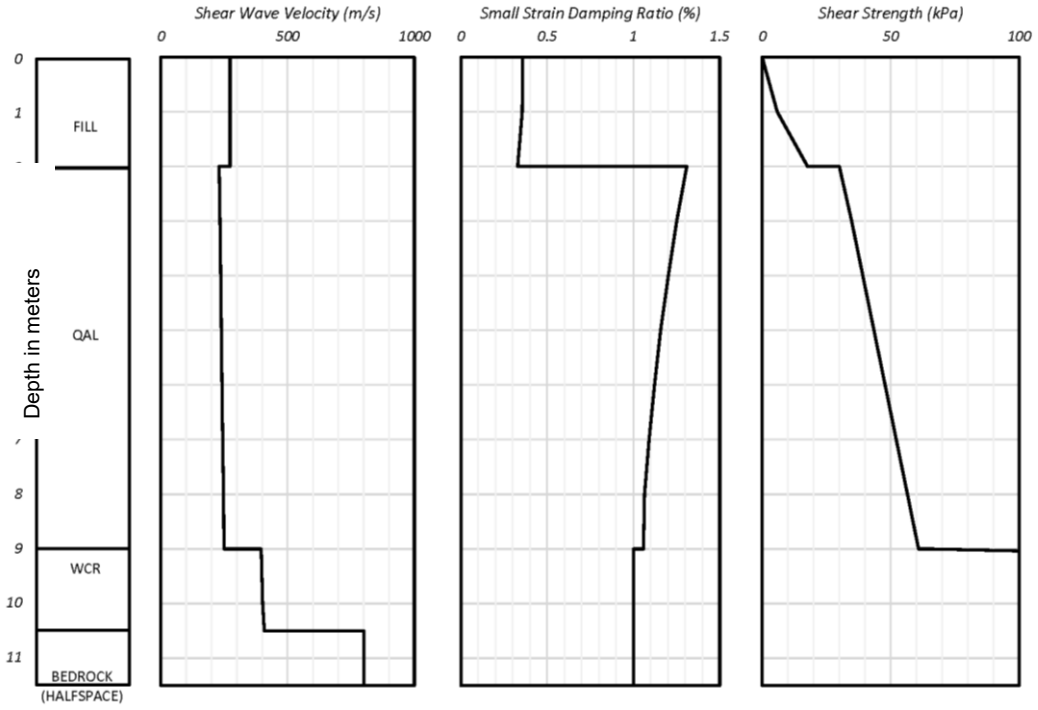

Figure 4.1: Profile B1UB DEEPSOIL model.

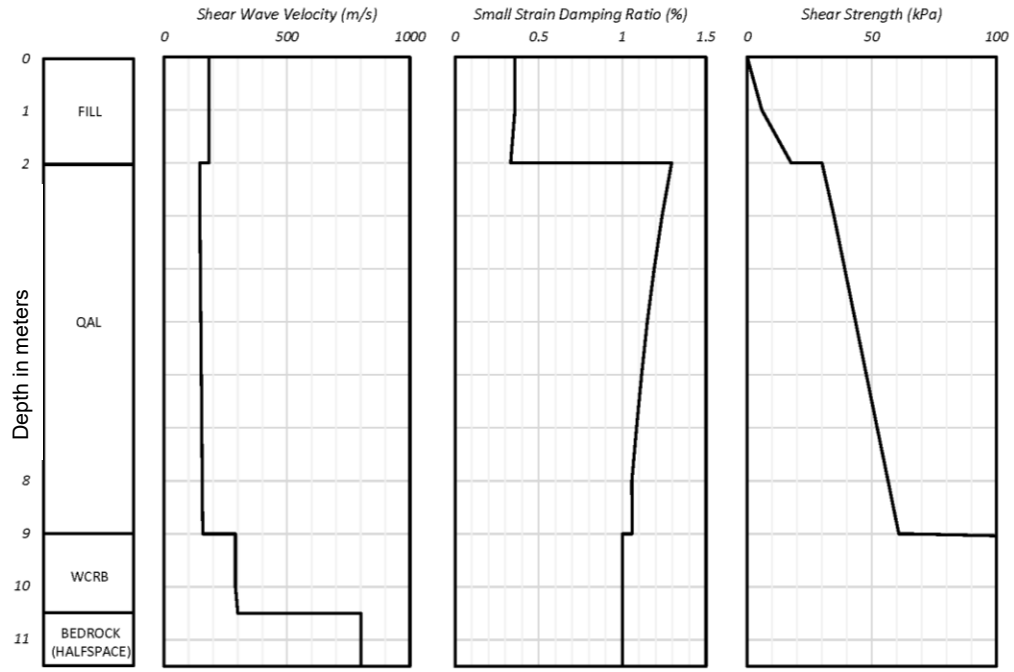

Figure 4.2: Profile B1 DEEPSOIL model.

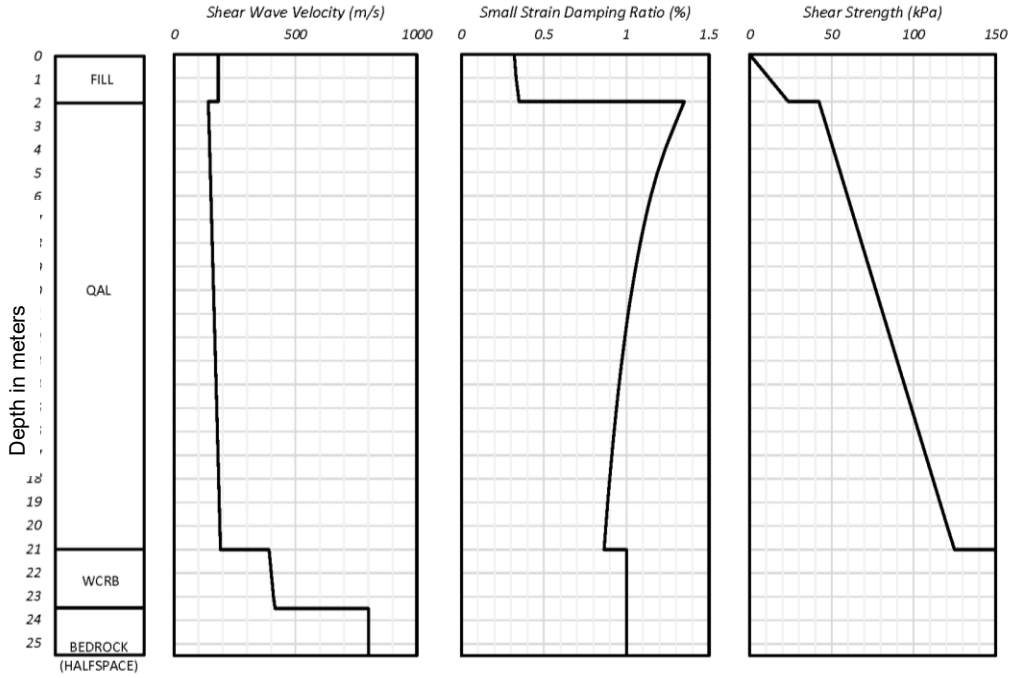

Figure 4.3: Profile B2 DEEPSOIL model.

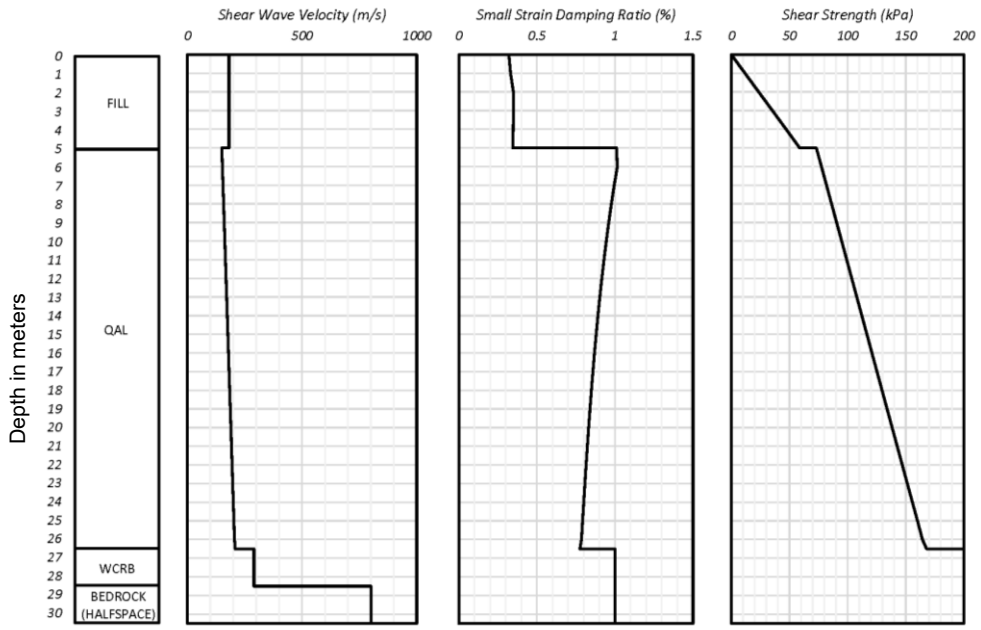

Figure 4.4: Profile B3 DEEPSOIL model.

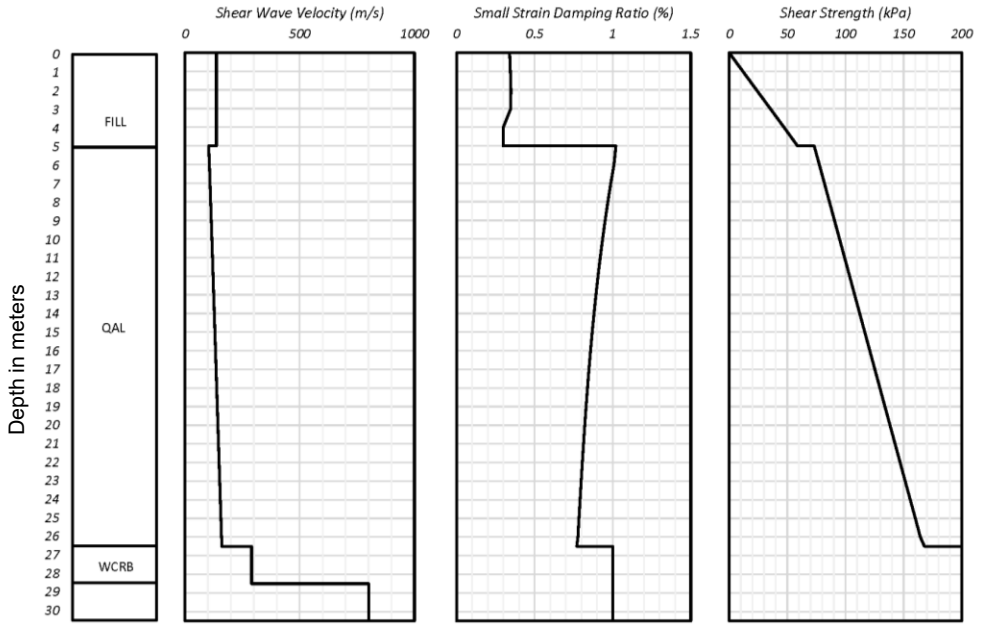

Figure 4.5: Profile B3LB DEEPSOIL model.

4.2 DEEPSOIL

The analyses were performed using the program DEEPSOIL (Hashash et al., 2020). DEEPSOIL is a unified site response platform that performs one-dimensional nonlinear time domain analyses and one-dimensional equivalent linear frequency domain analyses concurrently. For these

analyses, the General Quadratic/Hyperbolic Model (Groholski et al., 2016) was used as the default soil model. Non-Masing Reloading/Unloading rule was used as the default hysteretic formulation. Modulus reduction and damping curve fitting to the curves listed in Table 2.1 was performed using the built-in MRDF-UIUC curve-fitting tool in DEEPSOIL. The dynamic analyses were performed and analyzed for both equivalent linear and nonlinear dynamic analysis. However, for simplicity, the results of the nonlinear dynamic analysis are included in most of the results and figures.

Nonlinear and equivalent-linear site-response analyses were performed at each coordinate location identified in Table 2.1. This was done using all 30 M9 realization bedrock time-histories at each location. The analysis was repeated for each profile listed in Table 3.2, resulting in 300 analyses per coordinate (150 nonlinear and 150 equivalent linear) for an overall total of 1800 analyses.

4.3 REPRESENTATIVE ANALYSIS

Due to the large volume of analyses, the individual realization results are shown for a representative analysis followed by a summary of results for all analyses. Selected graphs from the analysis for realization 05, Profile B2, coordinate PDX IN (45.58, -122.49) are presented on Figures 4.6 to 4.11 to demonstrate the data produced from one realization analysis.

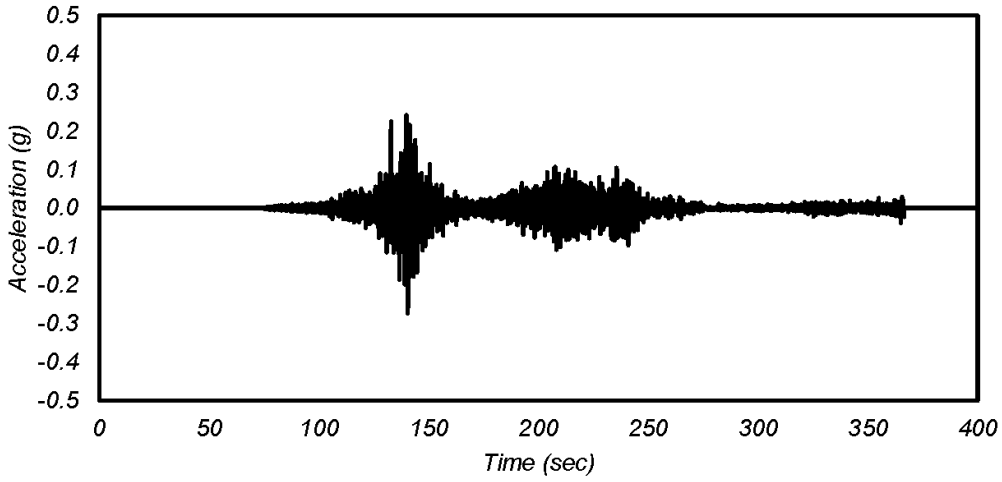

Input (outcrop) acceleration time history.

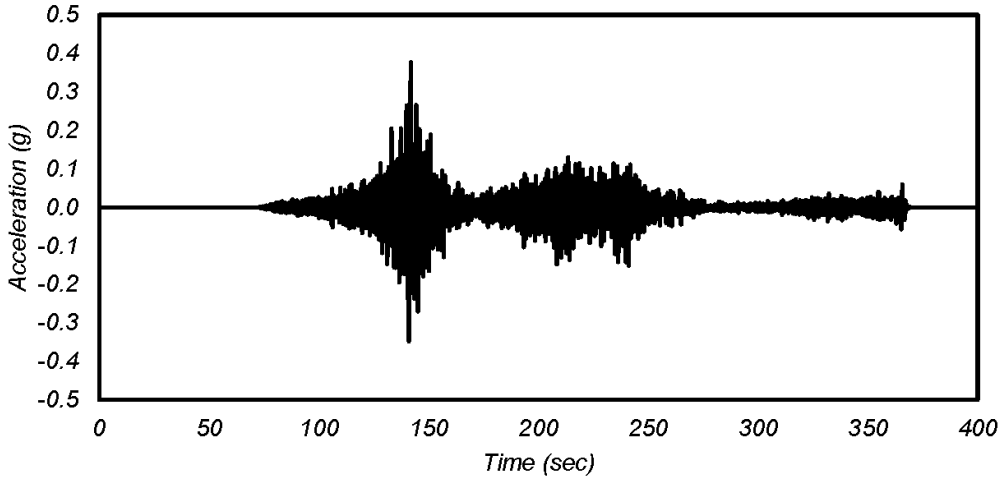

Ground surface acceleration time history.

Figure 4.6: Input and resulting surface ground-motion acceleration time-history from nonlinear analysis. Representative response from realization 05, profile B2, PDX IN (45.58, -122.49) location.

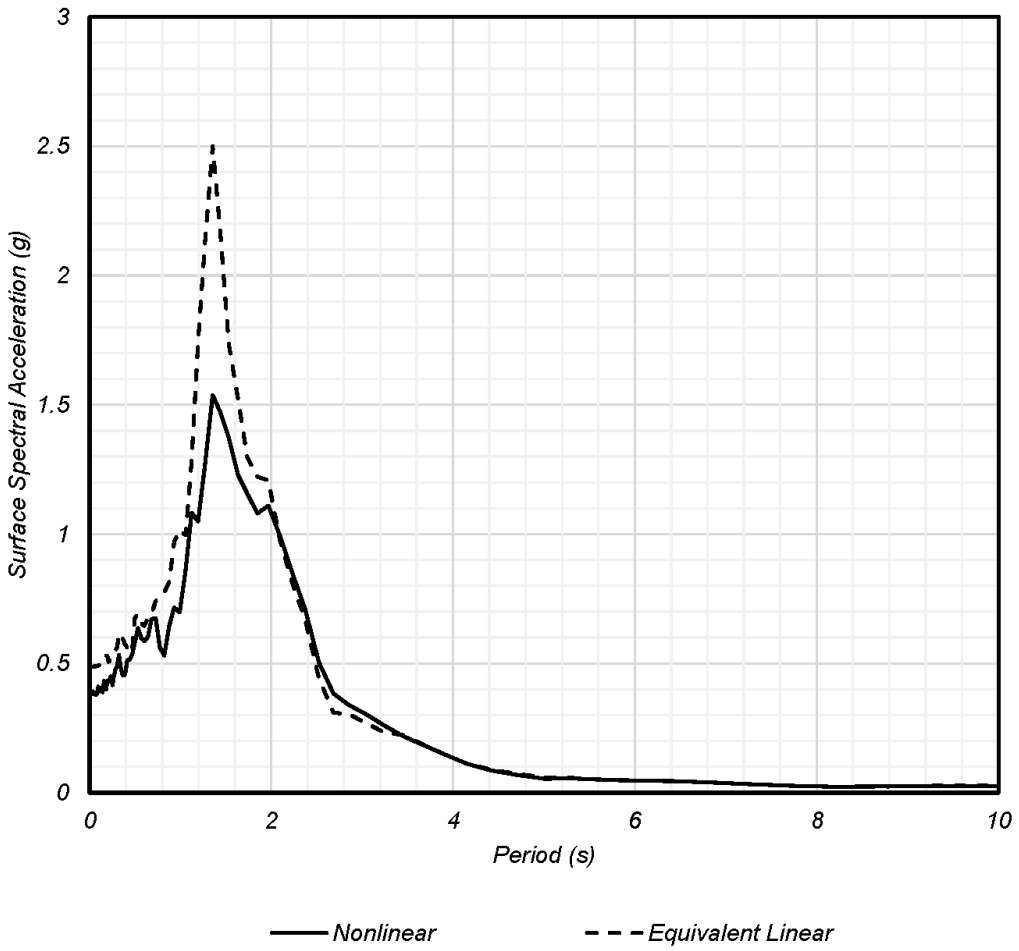

Figure 4.7: Surface response spectra from non-linear and equivalent linear analysis (representative response for realization 05, profile B2, PDX IN [45.58, -122.49]).

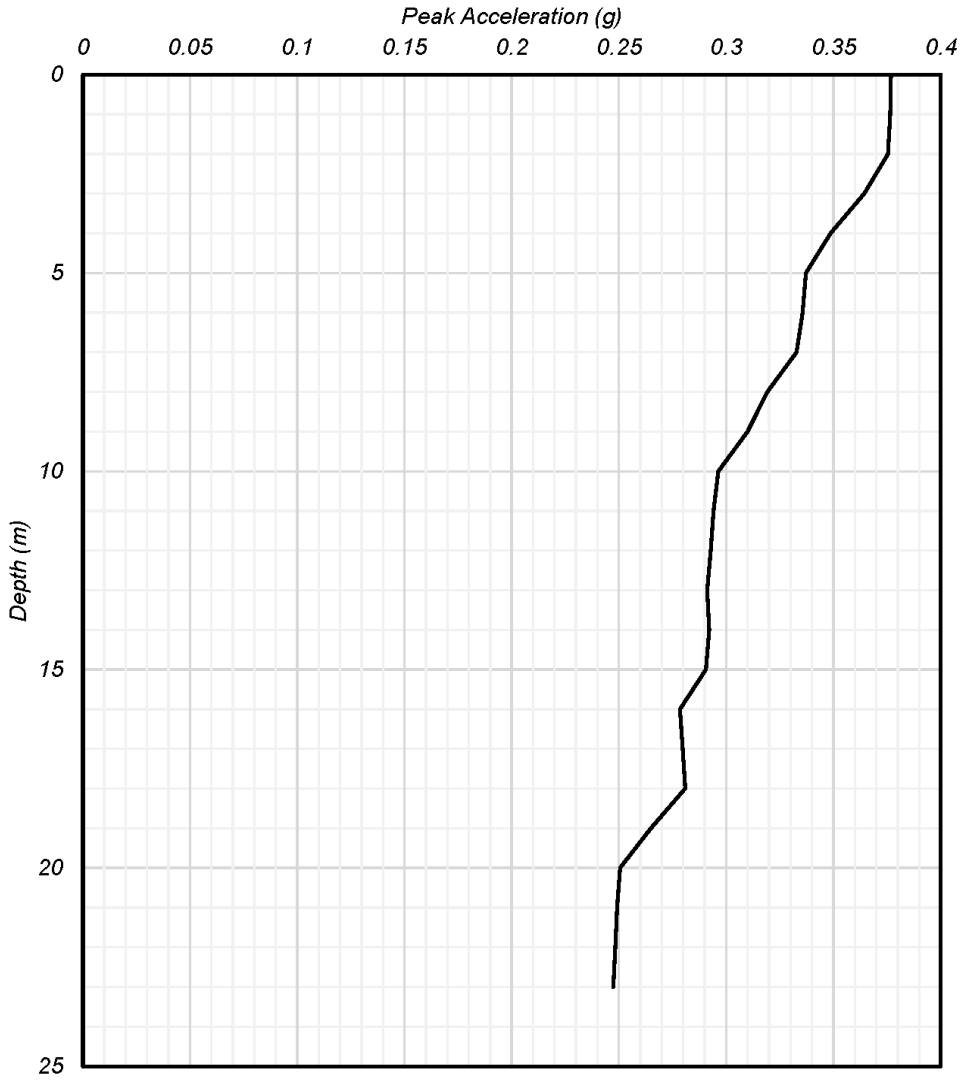

Figure 4.8: Peak acceleration from non-linear analysis (representative response from realization 05, profile B2, PDX IN [45.58, -122.49]).

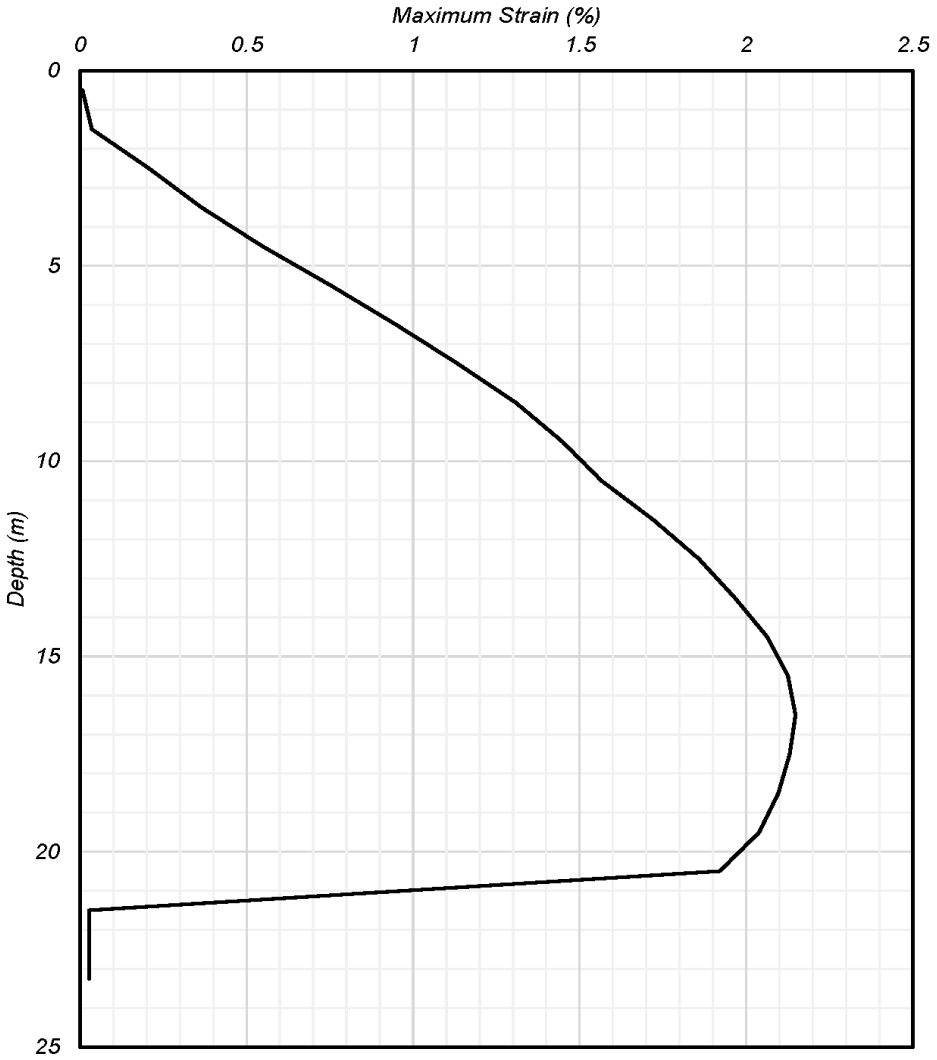

Figure 4.9: Peak shear strain from non-linear analysis (representative response from realization 05, profile B2, PDX IN [45.58, -122.49]).

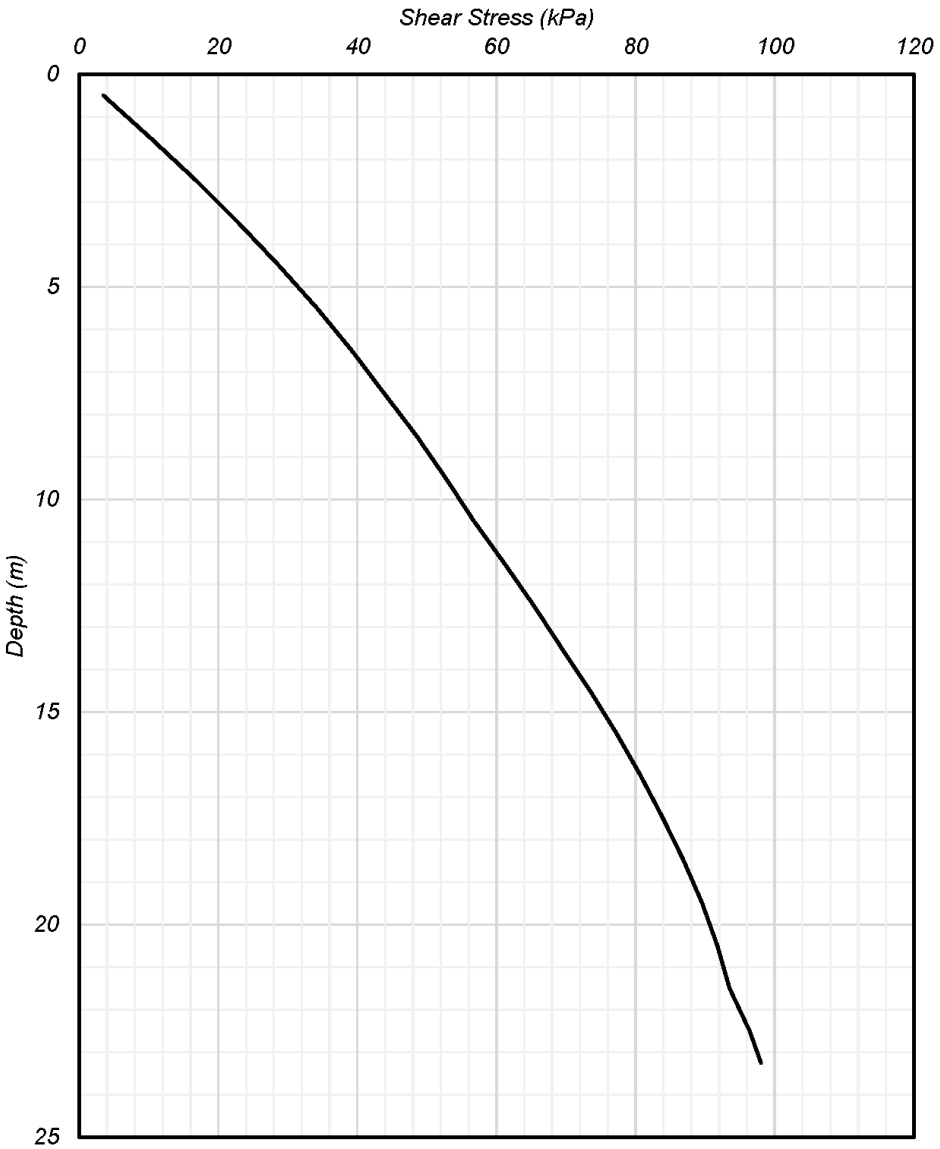

Figure 4.10: Peak shear stress from non-linear analysis (representative response from realization 05, profile B2, PDX IN [45.58, -122.49]).

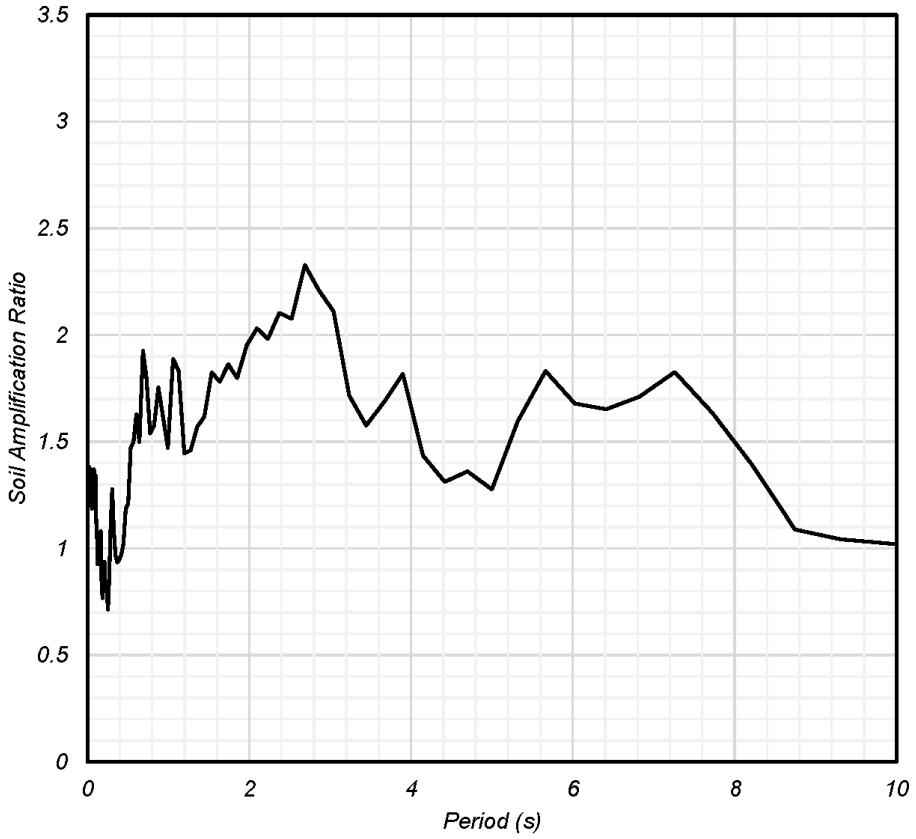

Figure 4.11: Soil amplification ratio from non-linear analysis (representative response for realization 05, profile B2, PDX IN [45.58, -122.49]).

4.4 VERIFICATION

The DEEPSOIL model generation and analysis process was verified by performing a comparison site-response analysis in the program FLAC by Itasca Consulting Group, Inc. FLAC is an explicit finite difference numerical modeling software capable of performing one- and two-dimensional dynamic, nonlinear site response analysis. The Profile B2 model was implemented in FLAC using the same soil parameters and modulus reduction and damping curves. The B2 model was analyzed with both DEEPSOIL and FLAC using the 30 realization bedrock motions from coordinate 45.56, -122.74, the location of the CEI hub. The results from both programs are presented on Figure 4.12.

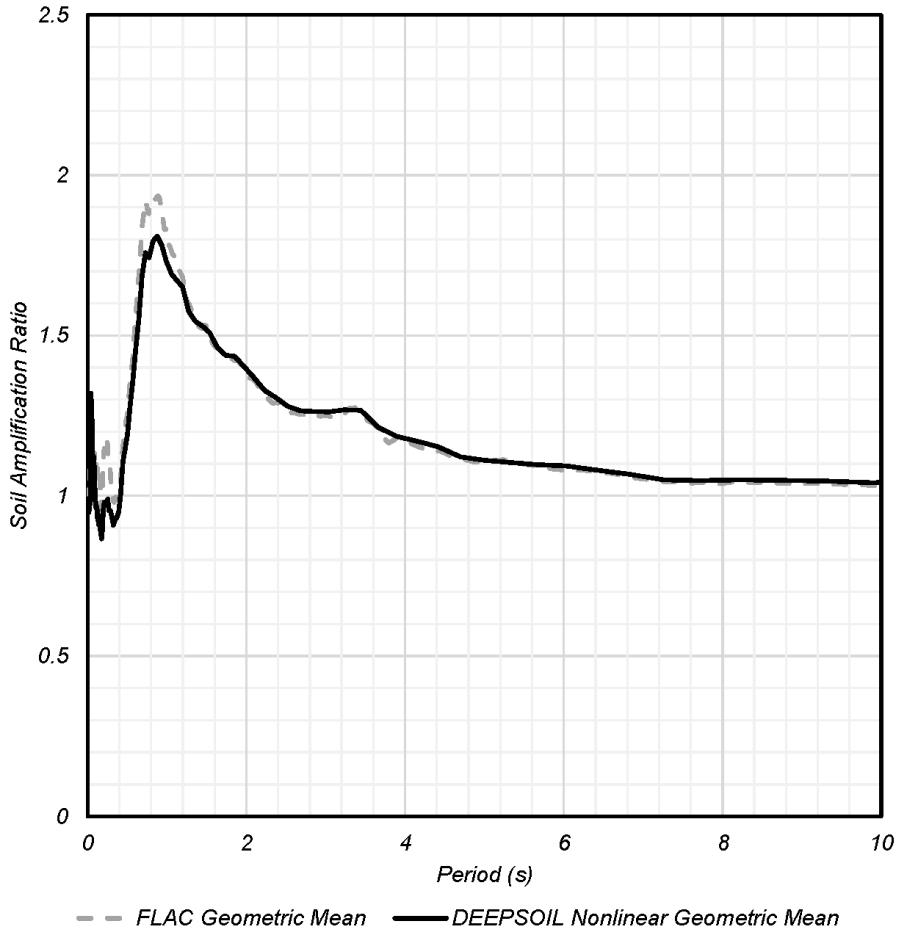

Figure 4.12: Site response analysis verification of DEEPSOIL using FLAC.

5.0 RESULTS

5.1 RESPONSE SPECTRA AT GROUND SURFACE

Figure 5.1 through Figure 5.30 display the 5-percent-damped surface-acceleration response-spectra computed from the site response analysis for each profile and coordinate location combination. Each figure depicts the geometric mean of the 30 individual realizations of surface response spectra (solid red line), the standard deviation from the geometric mean (dashed red lines) and the individual spectra of the realizations (gray lines).

Figure 5.1 through Figure 5.5 are the response spectra that correspond to location PDX IN located at 45.58 North latitude and 122.49 West longitude.

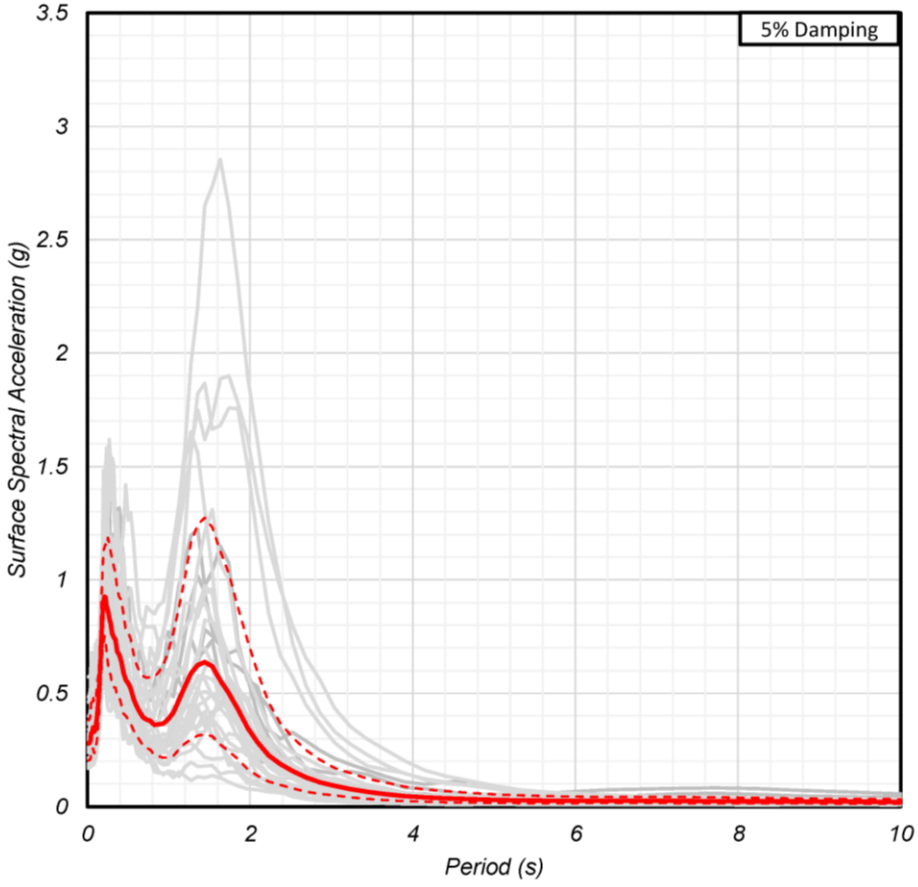

Figure 5.1: Surface acceleration spectra from non-linear analysis (profile B1UB, PDX IN (45.58, -122.49).

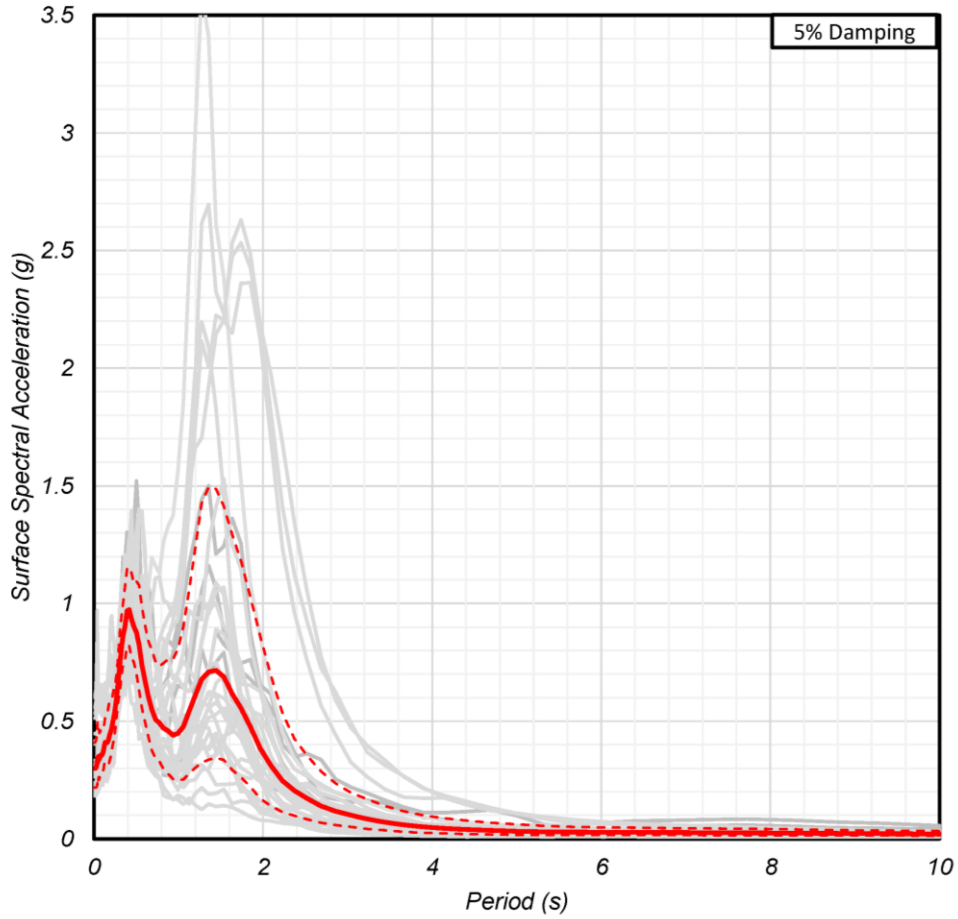

Figure 5.2: Surface acceleration spectra from non-linear analysis—profile B1, PDX IN (45.58, -122.49).

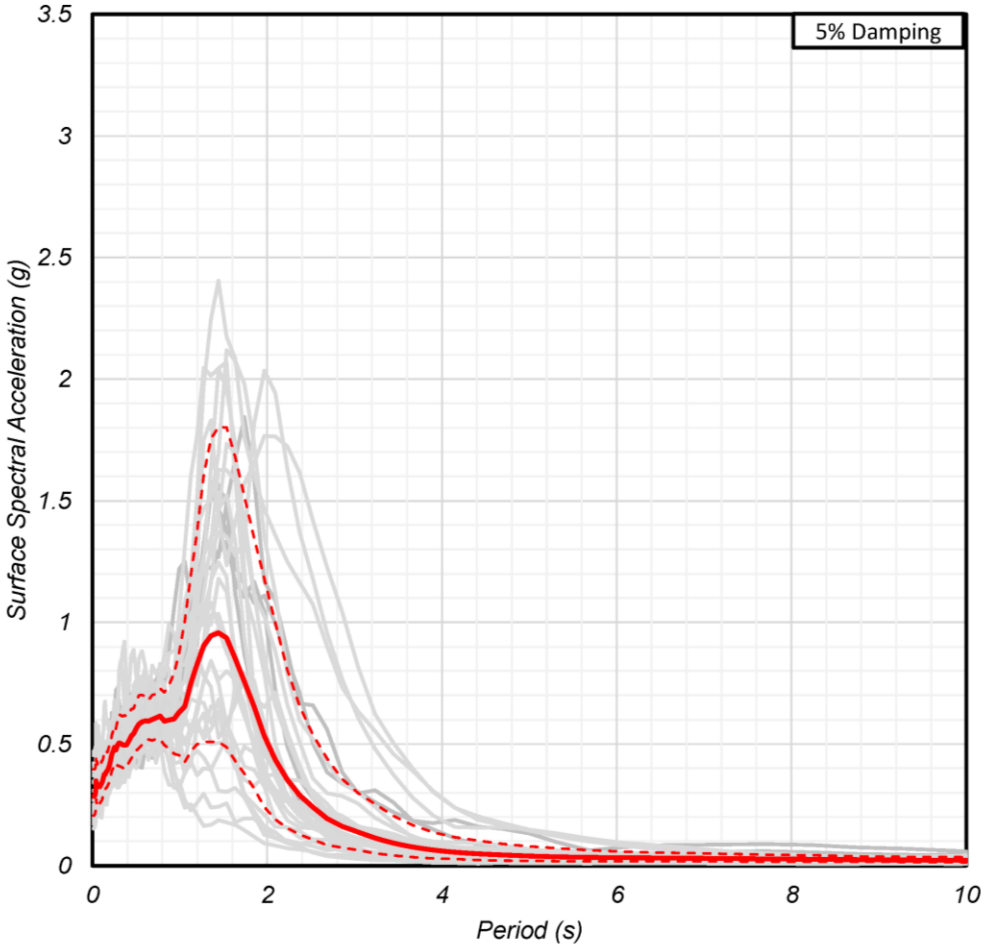

Figure 5.3: Surface acceleration spectra from non-linear analysis—profile B2, PDX IN (45.58, -122.49).

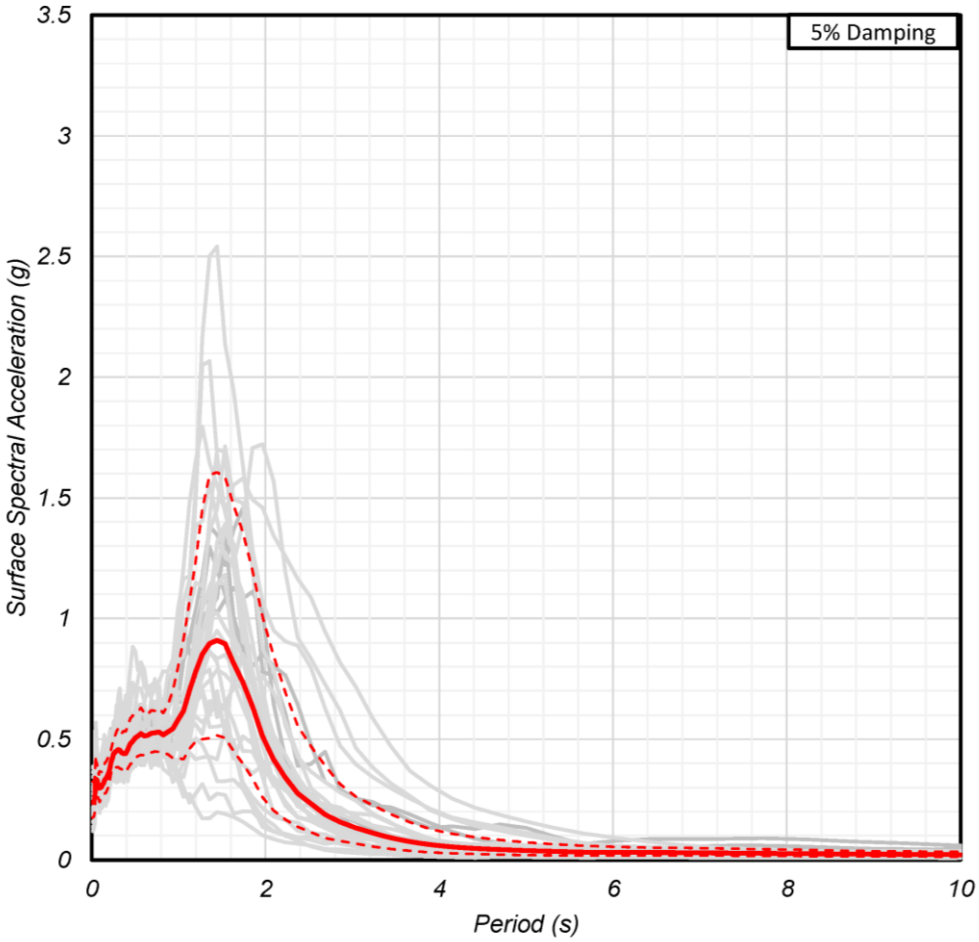

Figure 5.4: Surface acceleration Spectra from non-linear analysis—profile B3, PDX IN (45.58, -122.49).

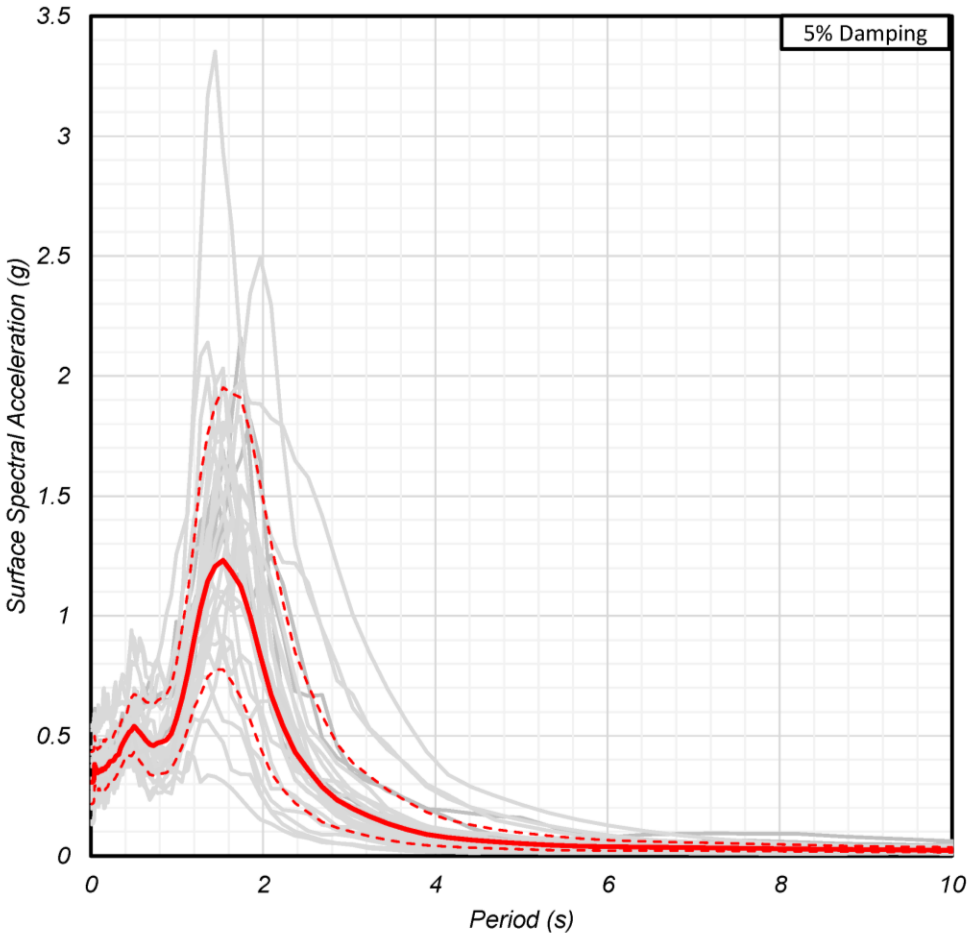

Figure 5.5: Surface acceleration spectra from non-linear analysis—profile B3LB, PDX IN (45.58, -122.49).

Figure 5.6 through Figure 5.10 are the response spectra that correspond to location PDX OUT located at 45.83 North latitude and 122.49 West longitude.

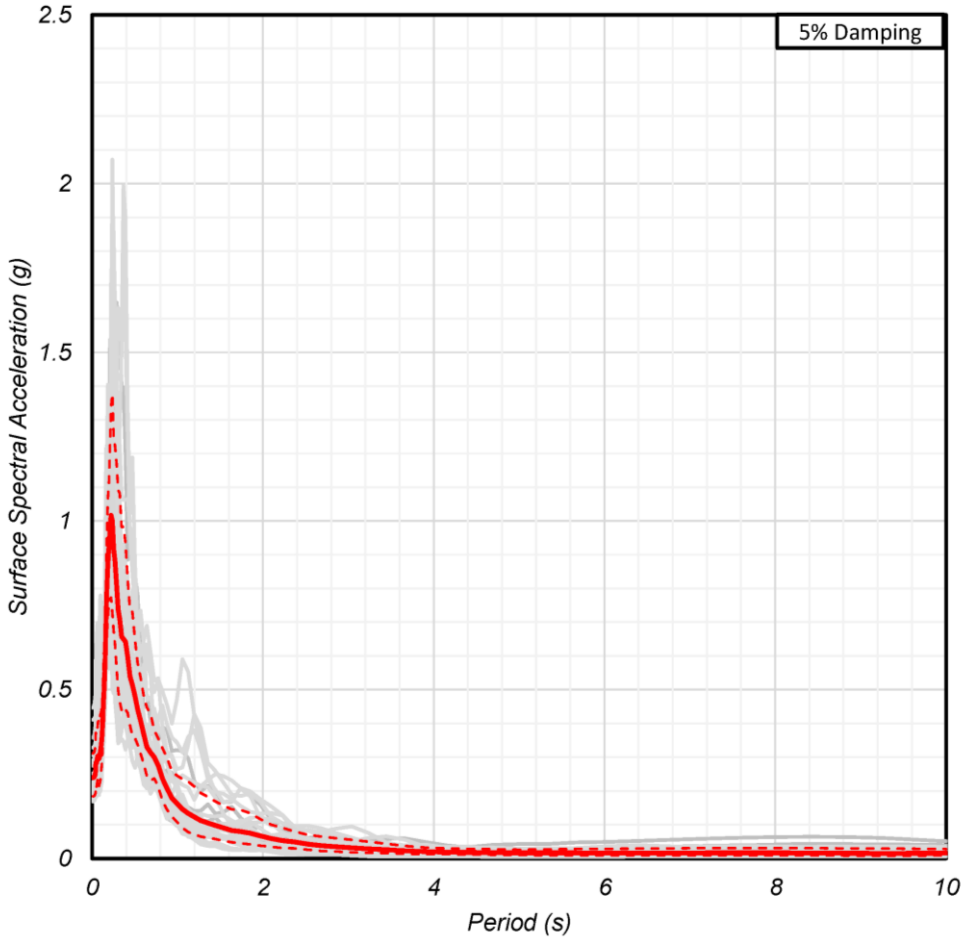

Figure 5.6: Surface acceleration spectra from non-linear analysis, profile B1UB, PDX OUT (45.83, -122.49).

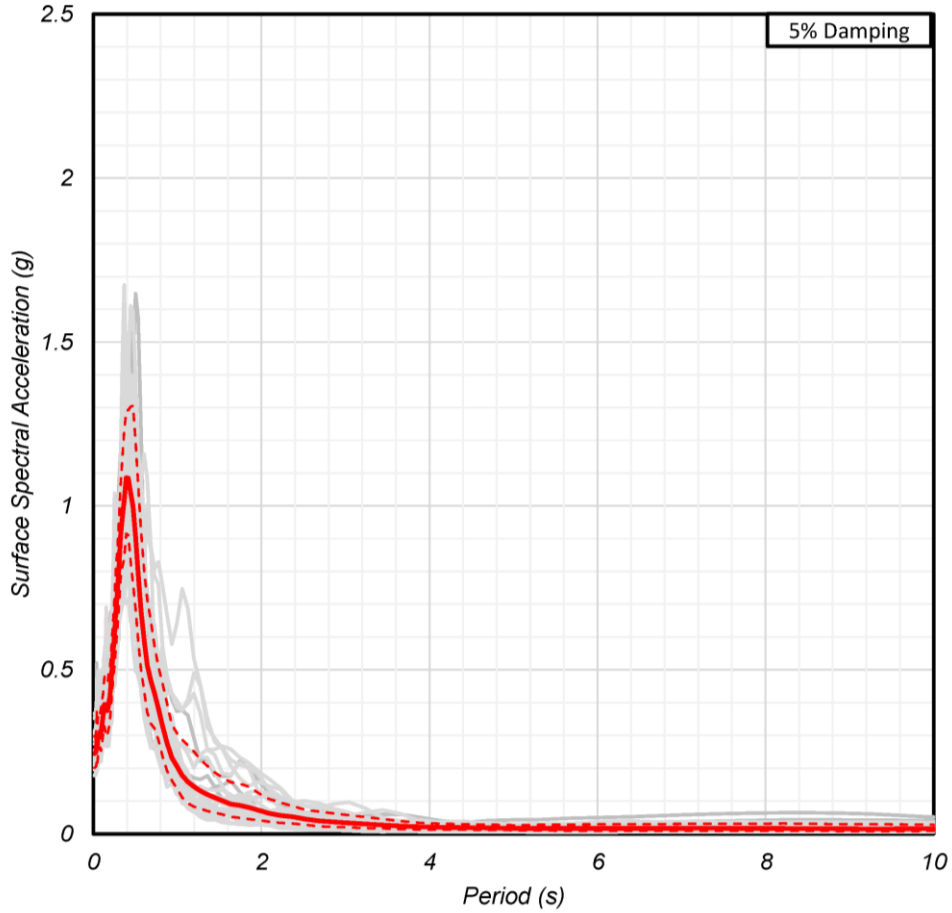

Figure 5.7: Surface acceleration spectra from non-linear analysis—profile B1, PDX OUT (45.83, -122.49).

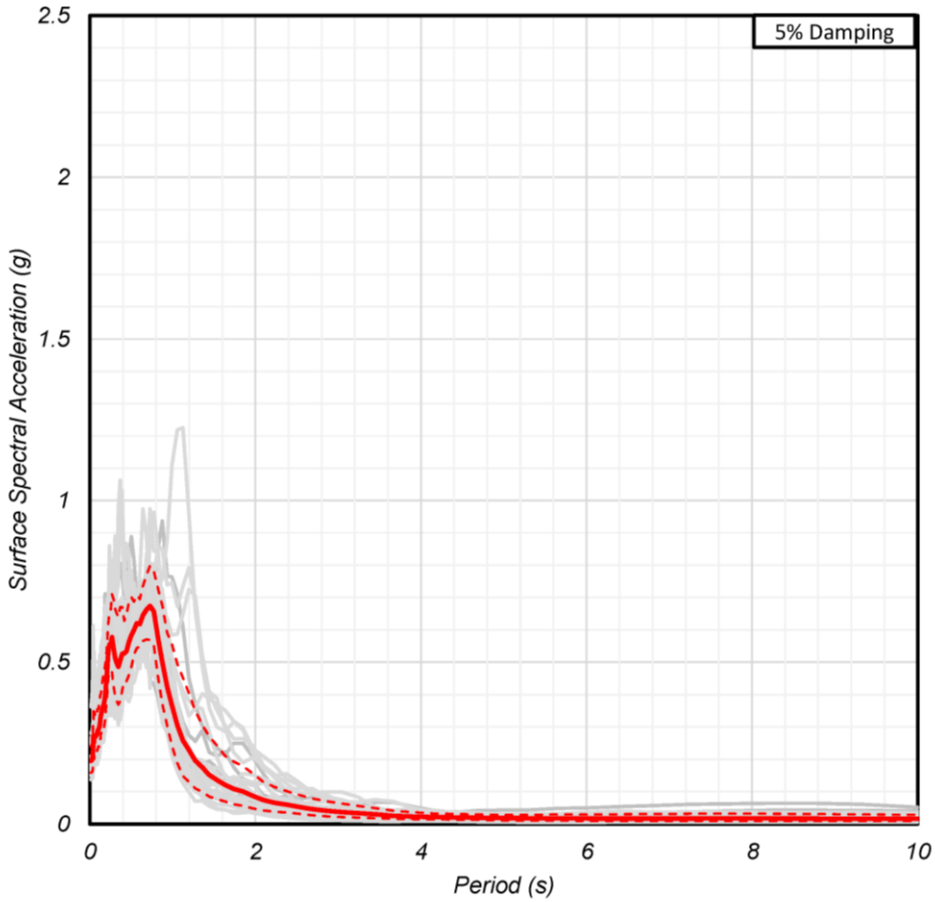

Figure 5.8: Surface acceleration spectra from non-linear analysis—profile B2, PDX OUT (45.83, -122.49).

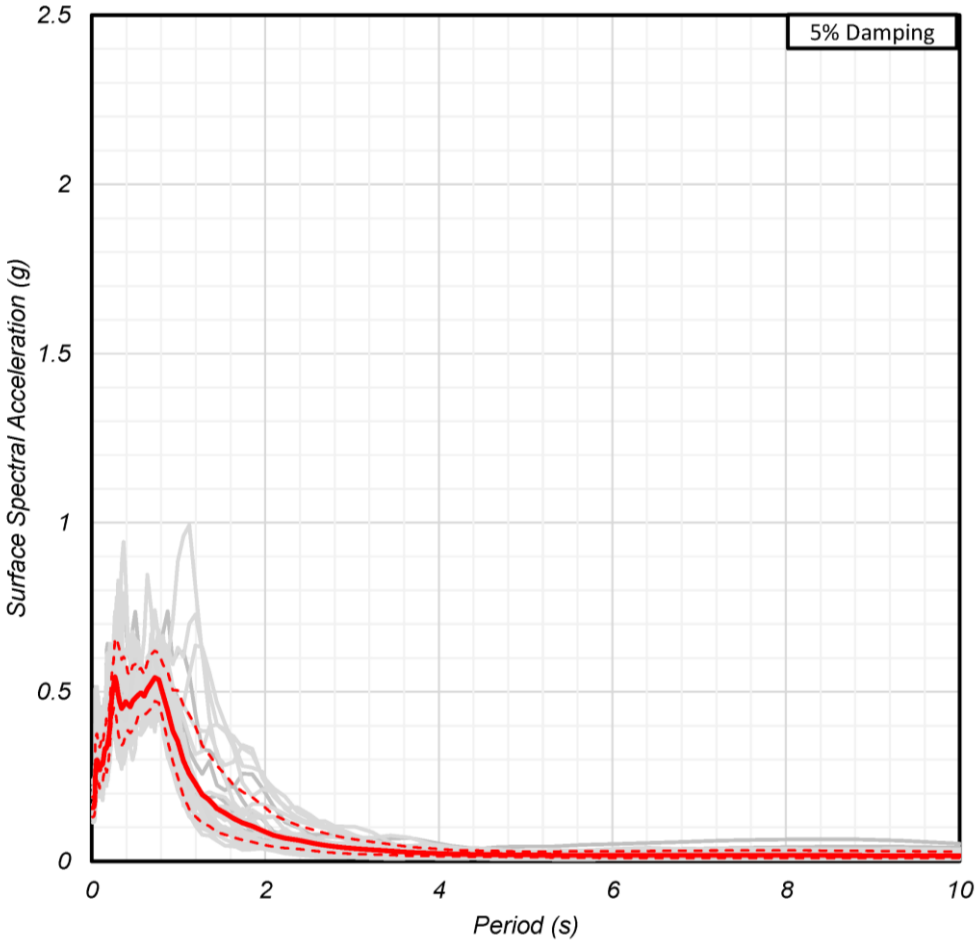

Figure 5.9: Surface acceleration spectra from non-linear analysis—profile B3, PDX OUT (45.83, -122.49).

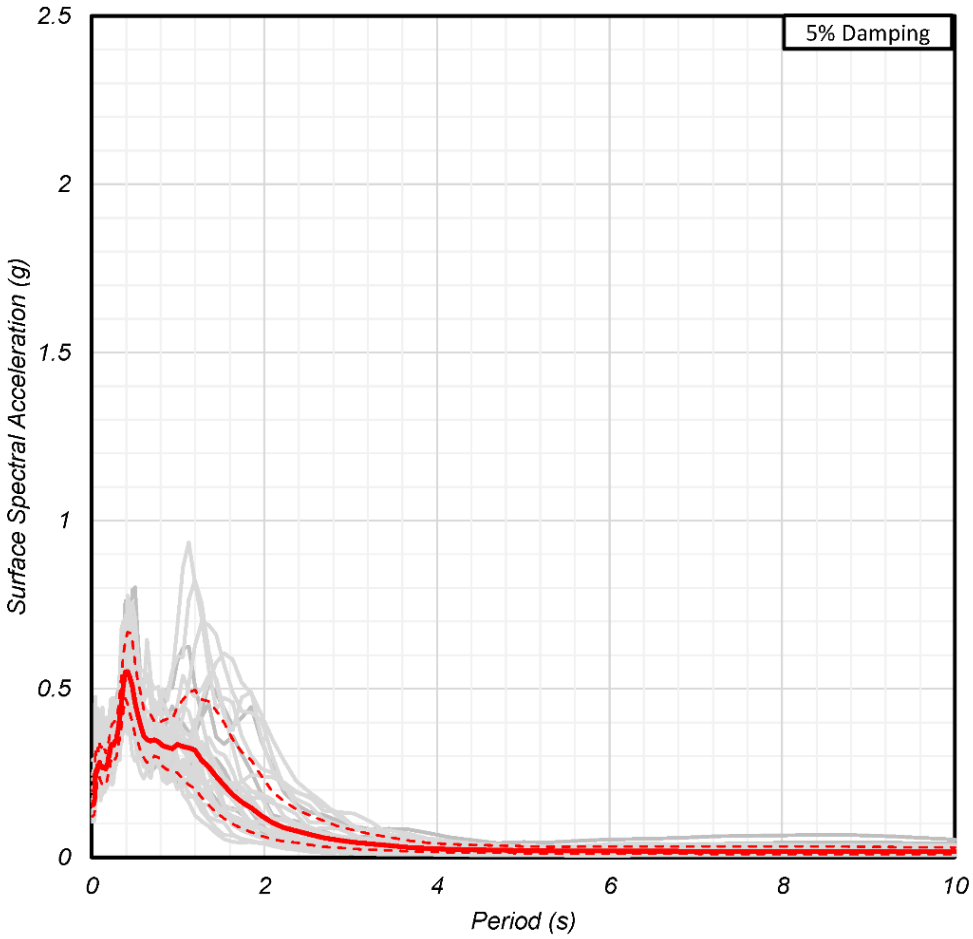

Figure 5.10: Surface acceleration spectra from non-linear analysis—profile B3LB, PDX OUT (45.83, -122.49).

Figure 5.11 through Figure 5.15 are the response spectra that correspond to location TUA IN located at 45.52 North latitude and 122.92 West longitude.

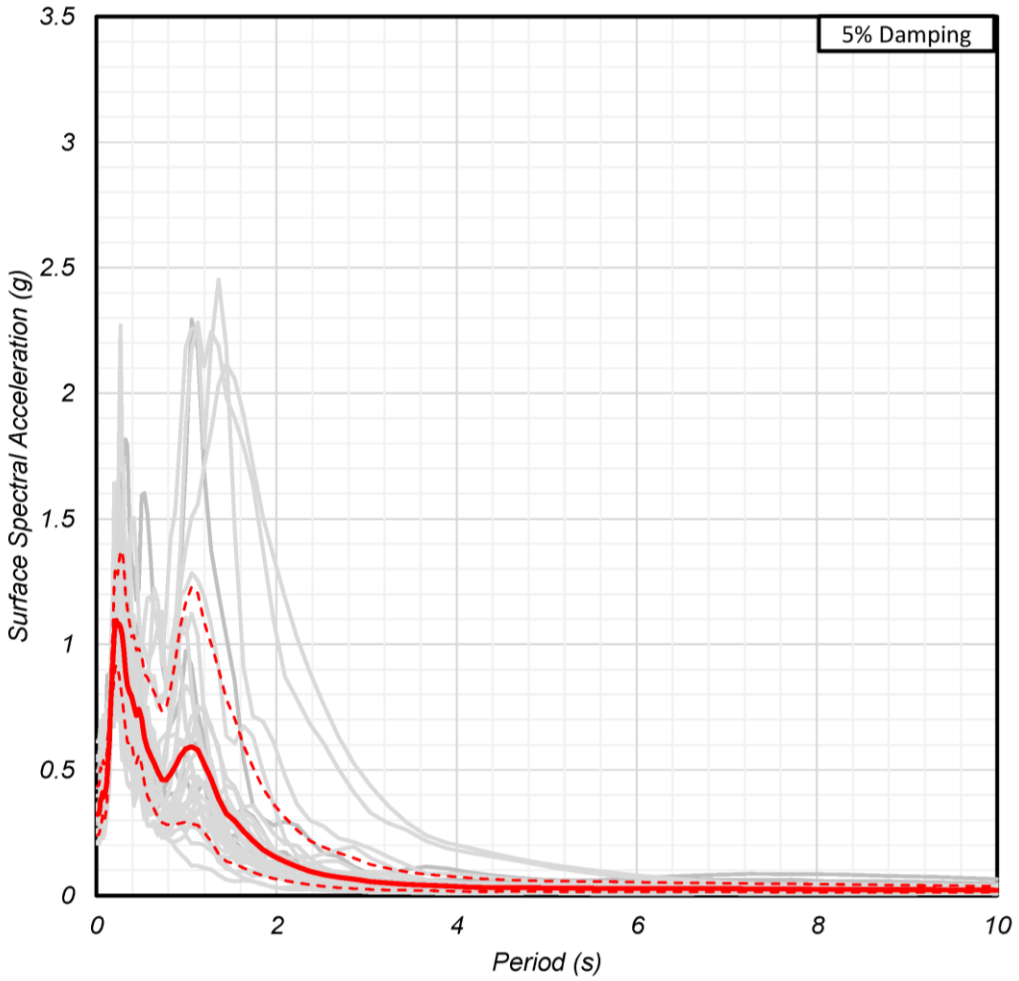

Figure 5.11: Surface acceleration from non-linear analysis—profile B1UB, TUA IN (45.52, -122.92).

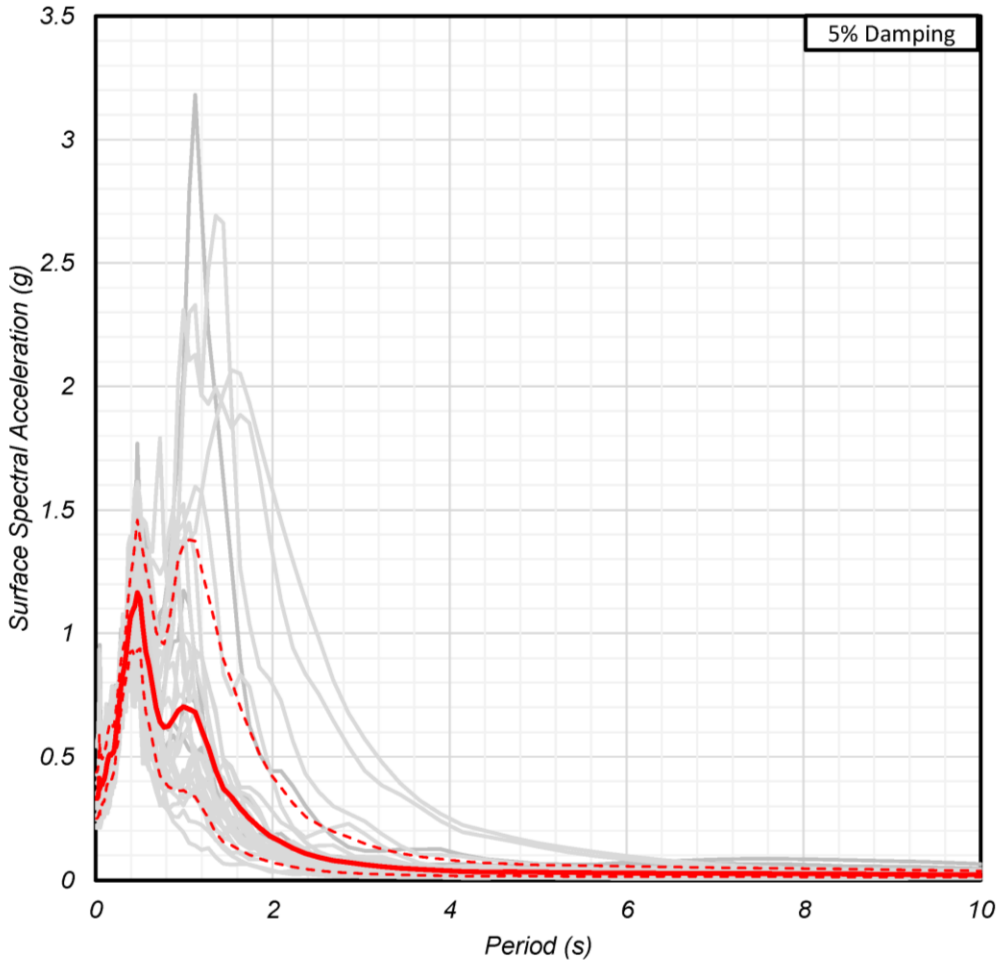

Figure 5.12: Surface acceleration from non-linear analysis—profile B1, TUA IN (45.52, -122.92).

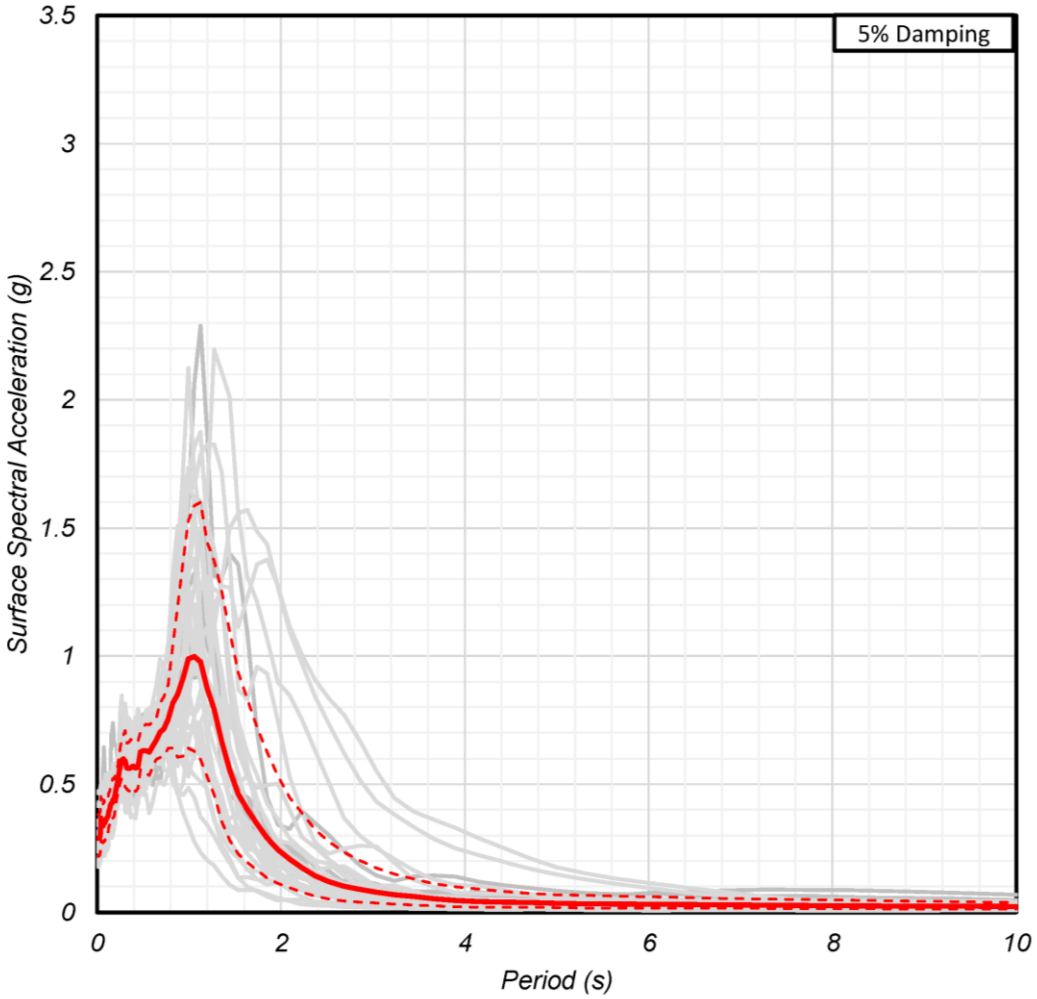

Figure 5.13: Surface acceleration from non-linear analysis—profile B2, TUA IN (45.52, -122.92).

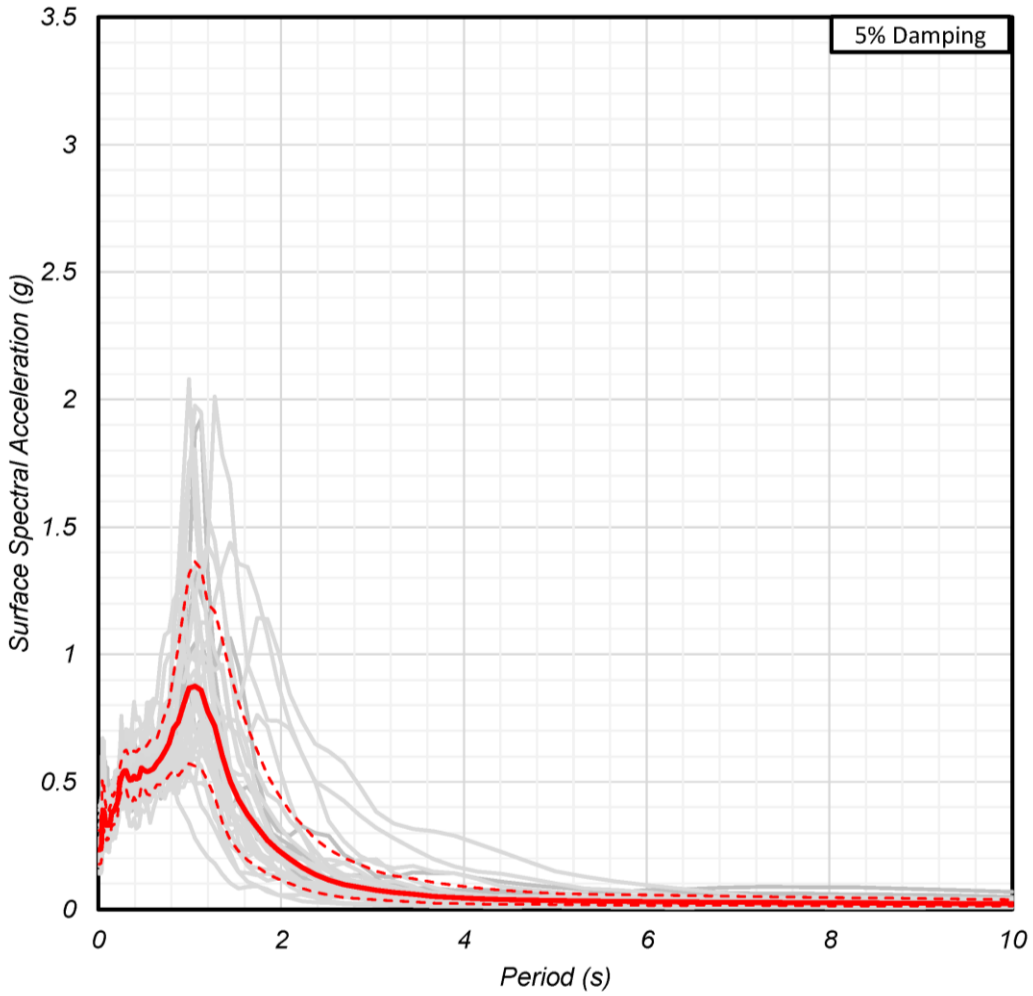

Figure 5.14: Surface acceleration from non-linear analysis—profile B3, TUA IN (45.52, -122.92).

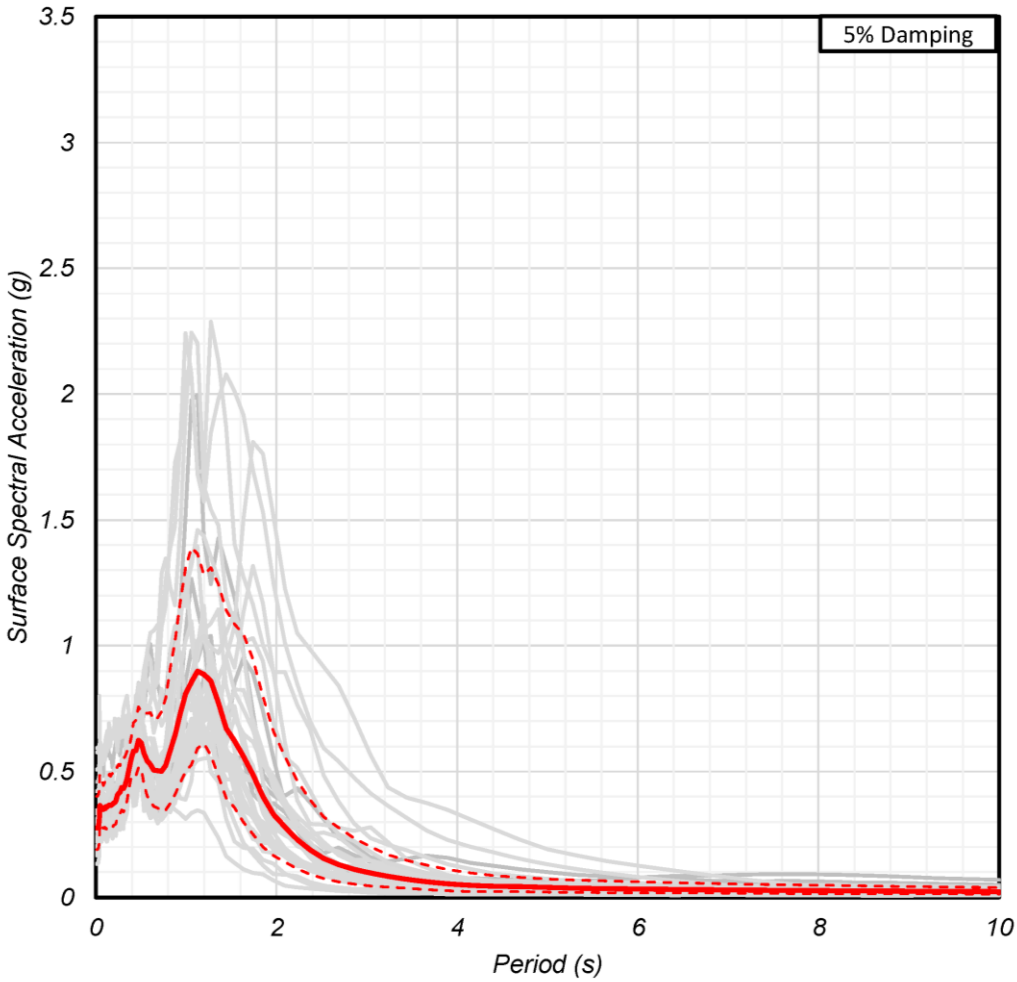

Figure 5.15: Surface acceleration from non-linear analysis—profile B3LB, TUA IN (45.52, -122.92).

Figure 5.16 through Figure 5.20 are the response spectra that correspond to location TUA OUT located at 45.83 North latitude and 122.92 West longitude.

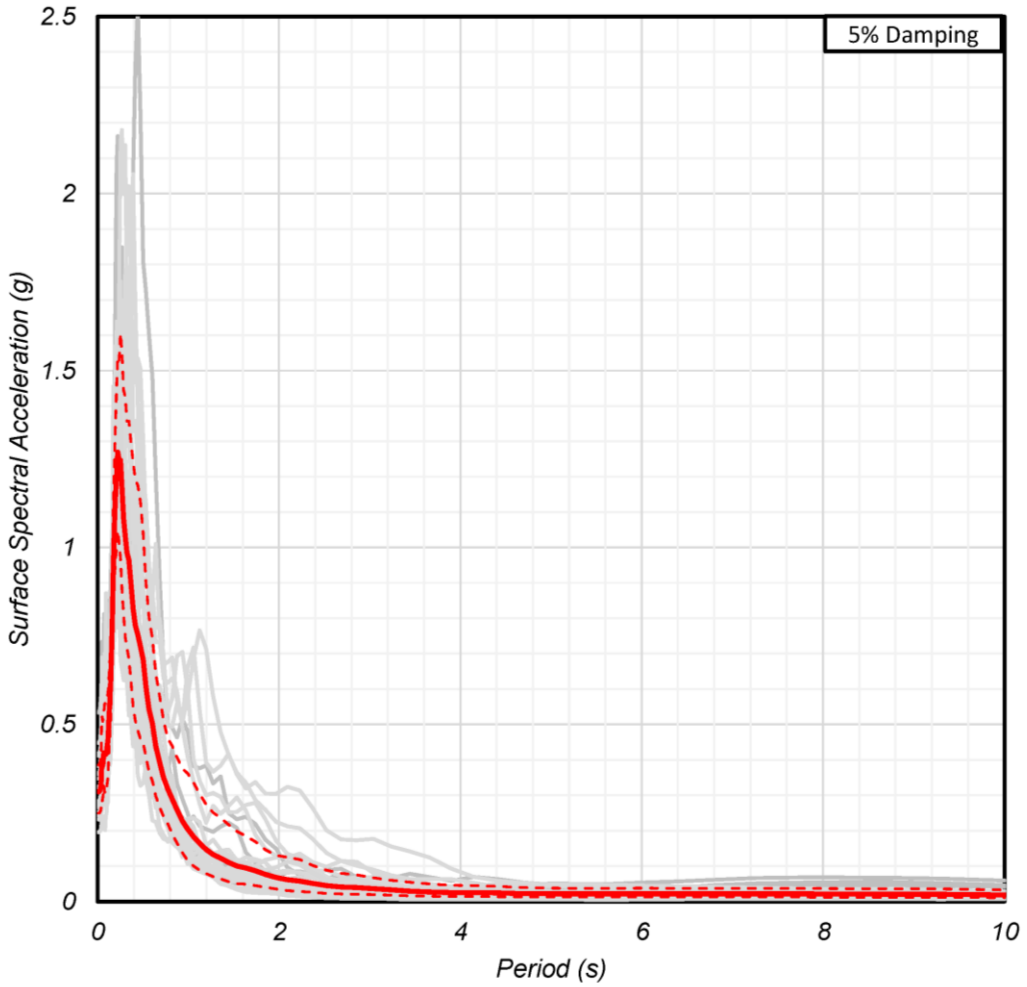

Figure 5.16: Surface acceleration from non-linear analysis—profile B1UB, TUA OUT (45.67, -122.92).

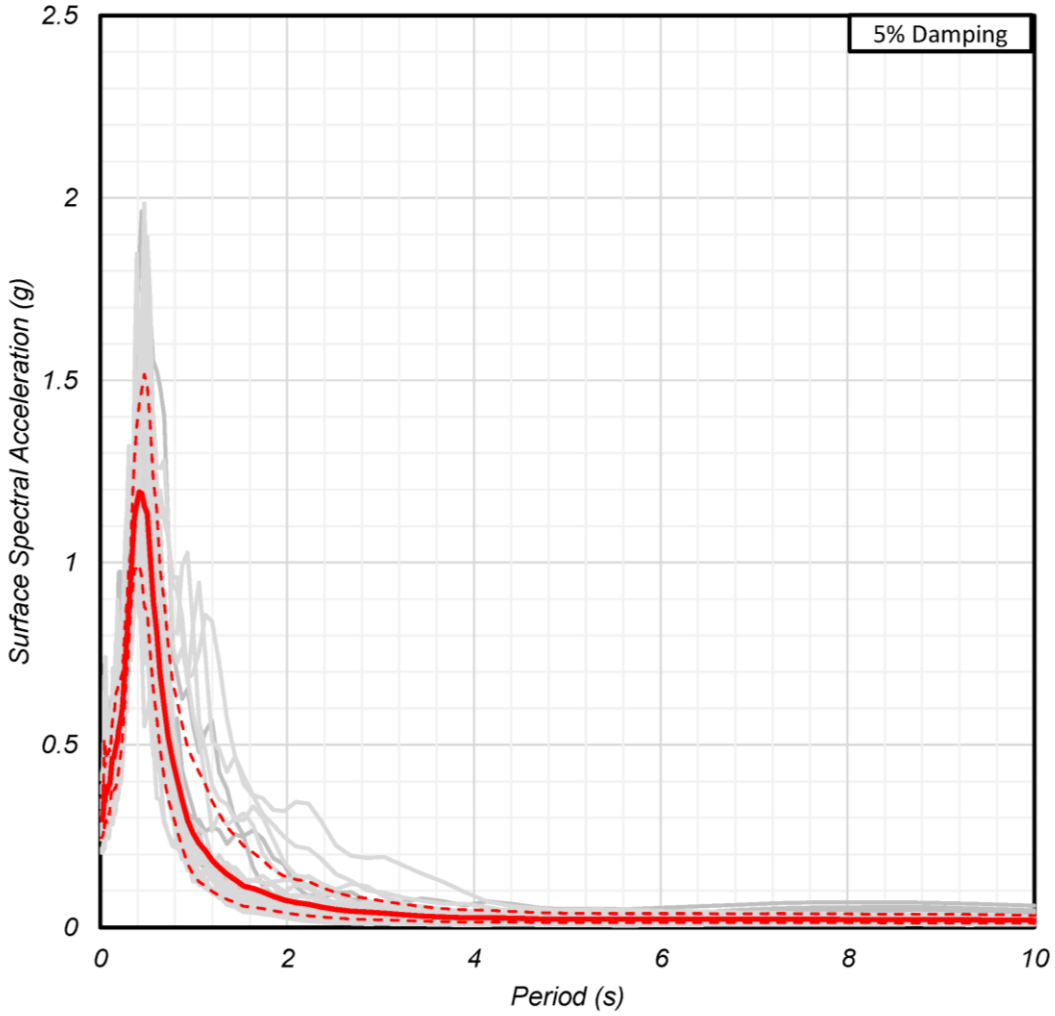

Figure 5.17: Surface acceleration from non-linear analysis—profile B1, TUA OUT (45.67, -122.92).

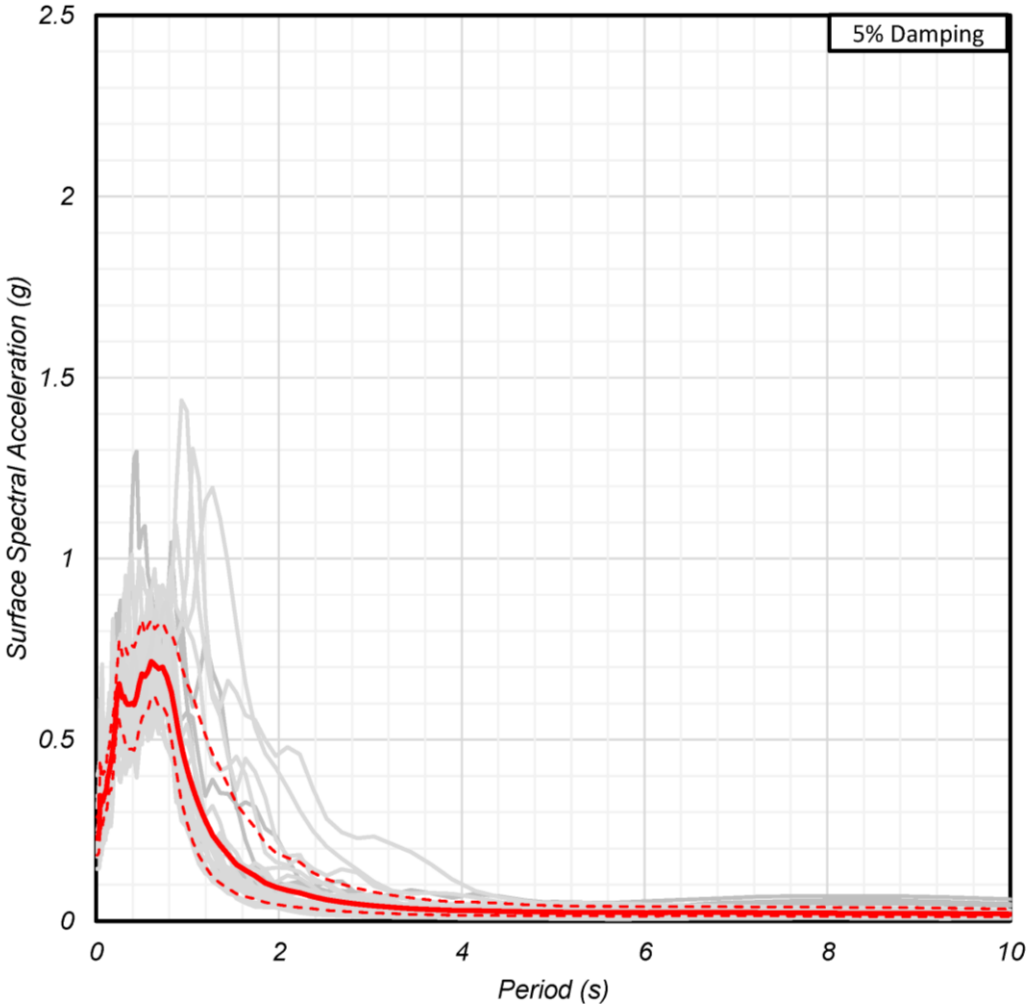

Figure 5.18: Surface acceleration from non-linear analysis—profile B2, TUA OUT (45.67, -122.92).

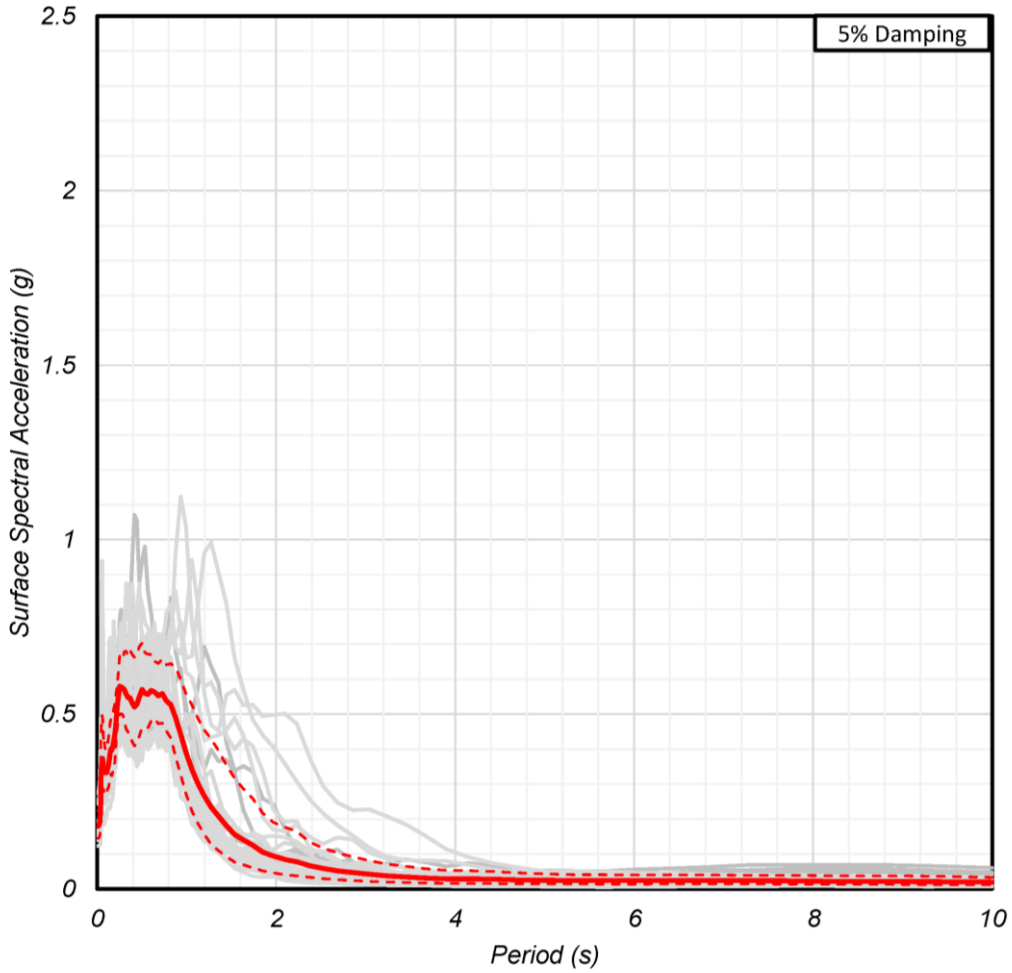

Figure 5.19: Surface acceleration from non-linear analysis—profile B3, TUA OUT (45.67, -122.92).

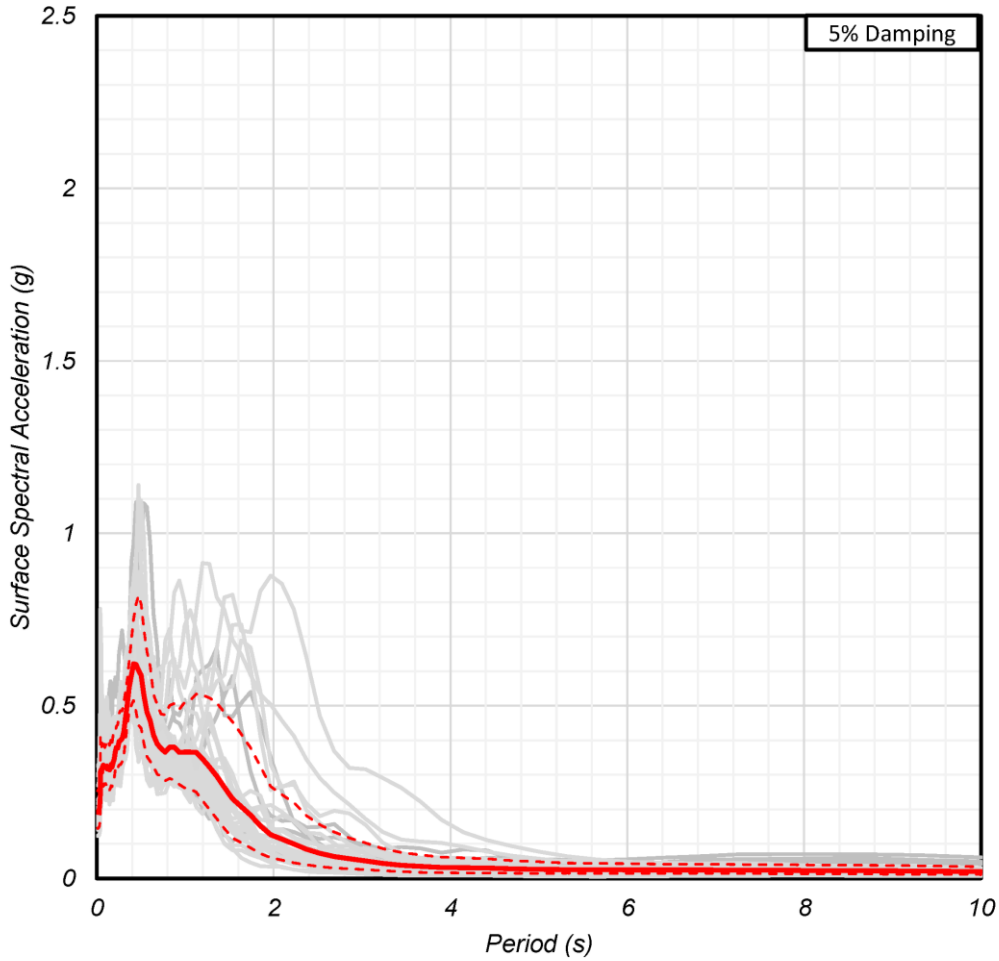

Figure 5.20: Surface acceleration from non-linear analysis—profile B3LB, TUA OUT (45.67, -122.92).

Figure 5.21 through Figure 5.25 are the response spectra that correspond to location NWB IN located at 45.11 North latitude and 122.76 West longitude.

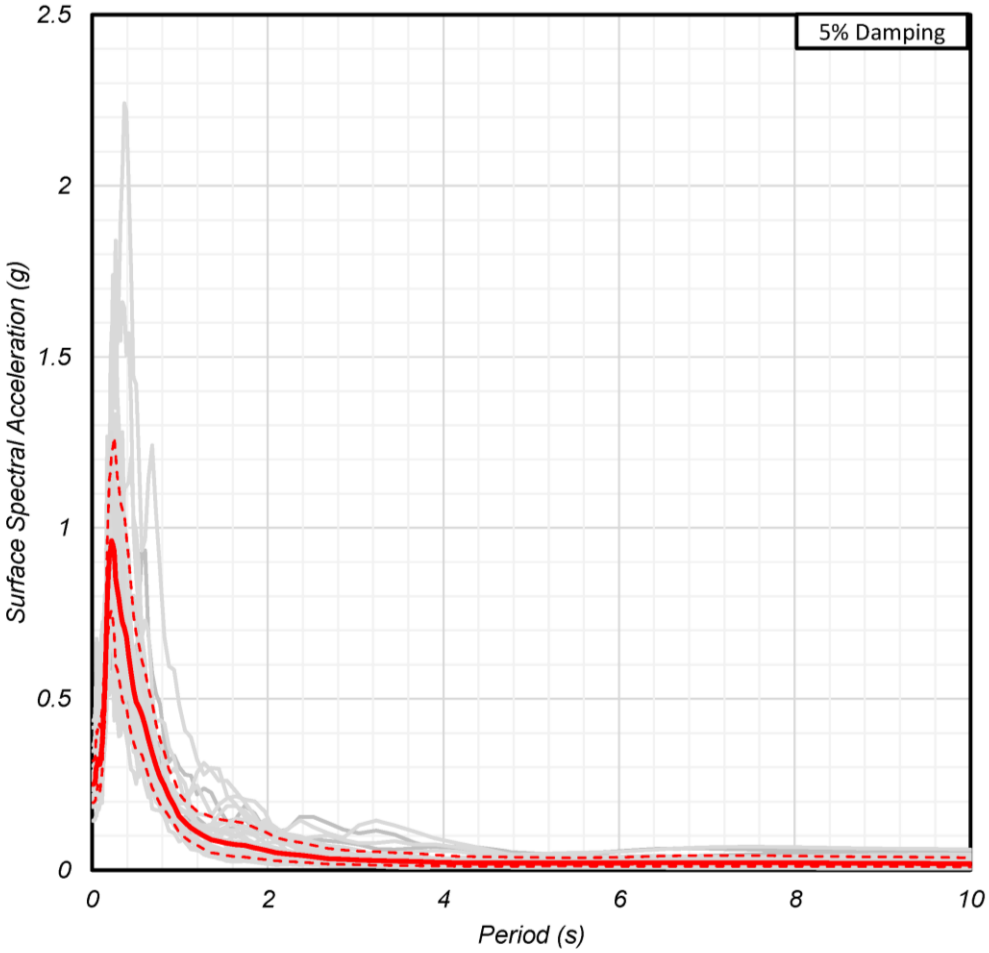

Figure 5.21: Surface acceleration from non-linear analysis—profile B1UB, NWB IN (45.11, -122.76).

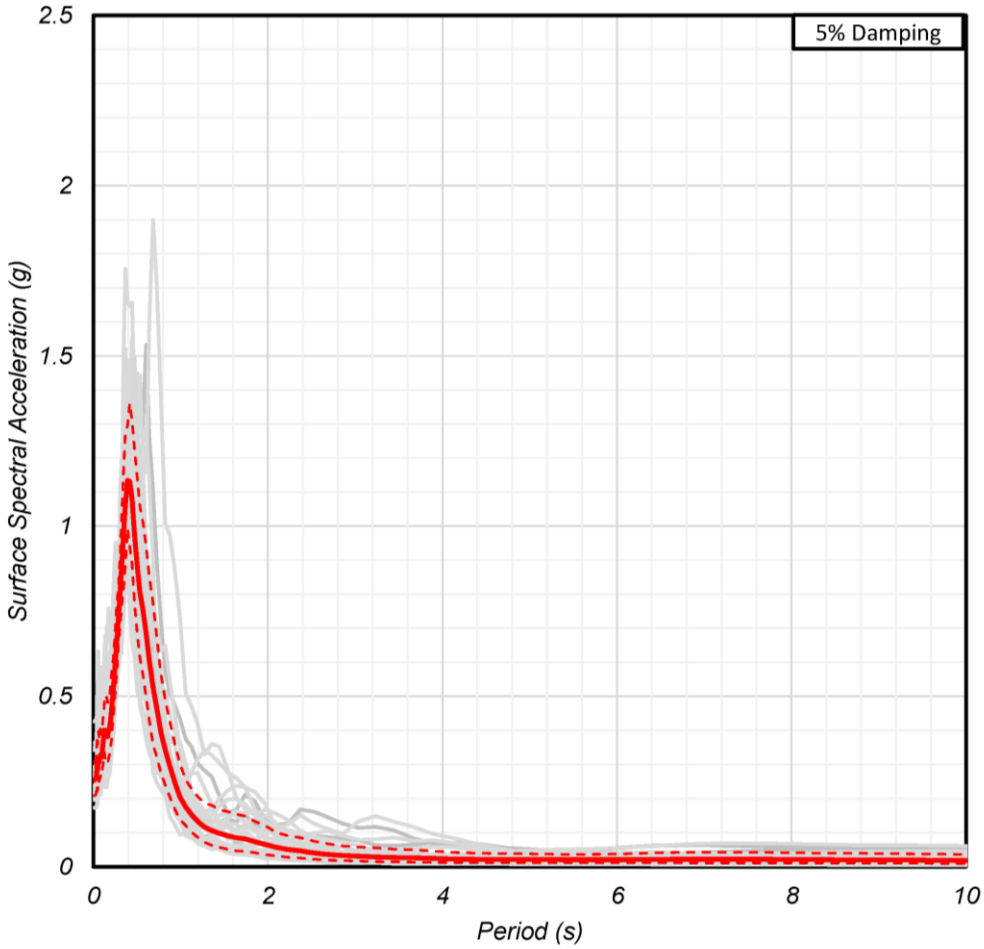

Figure 5.22: Surface acceleration from non-linear analysis—profile B1, NWB IN (45.11, -122.76).

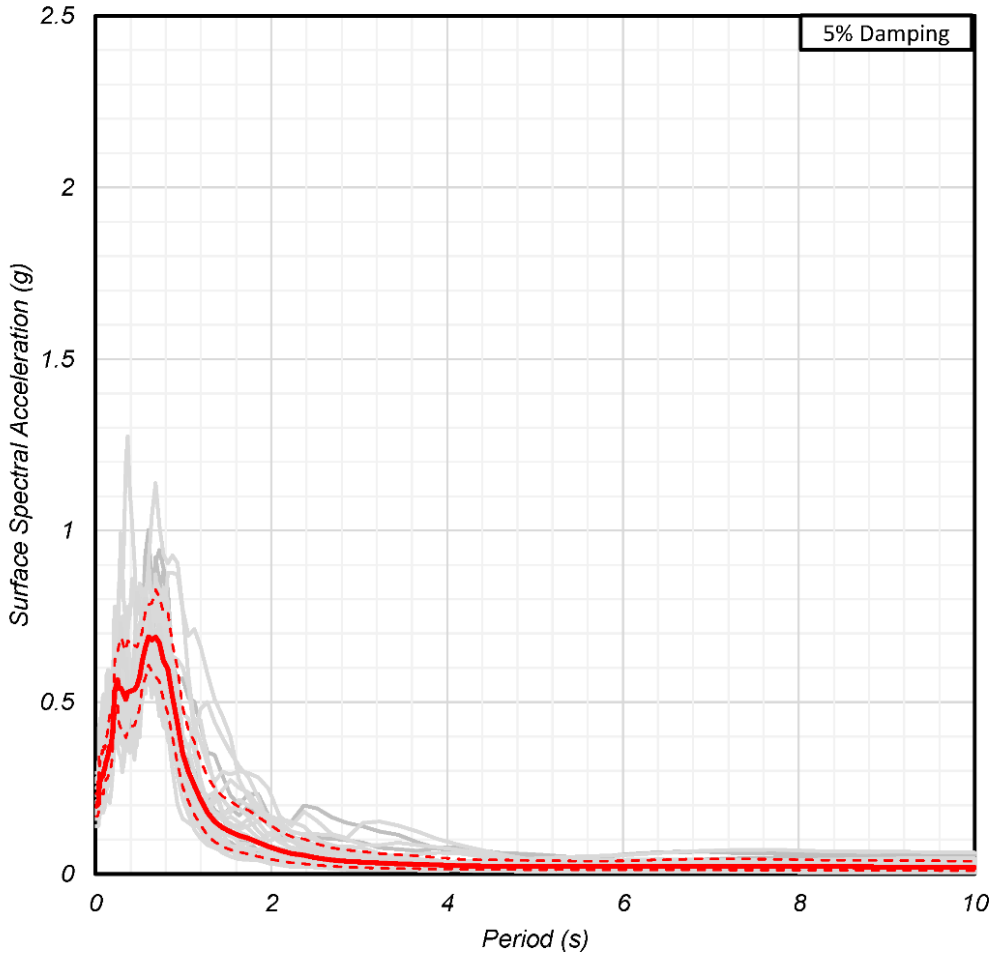

Figure 5.23: Surface acceleration from non-linear analysis—profile B2, NWB IN (45.11, -122.76).

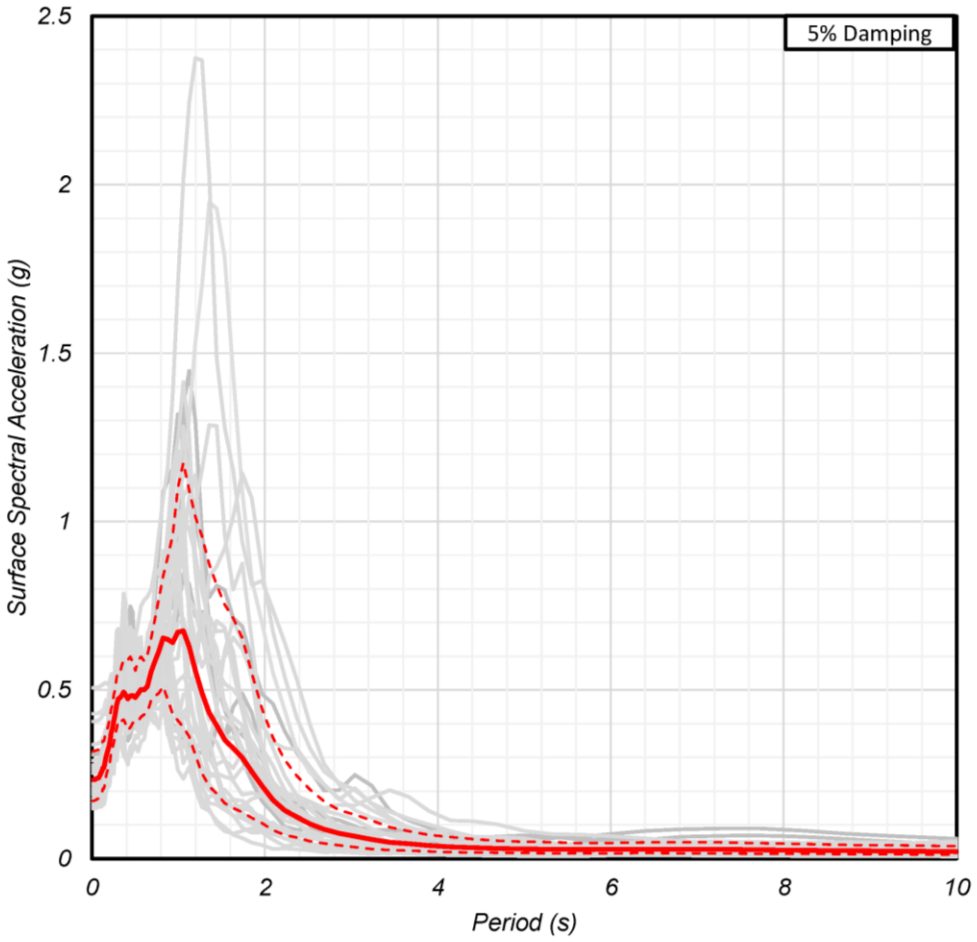

Figure 5.24: Surface acceleration from non-linear analysis—profile B3, NWB IN (45.11, -122.76).

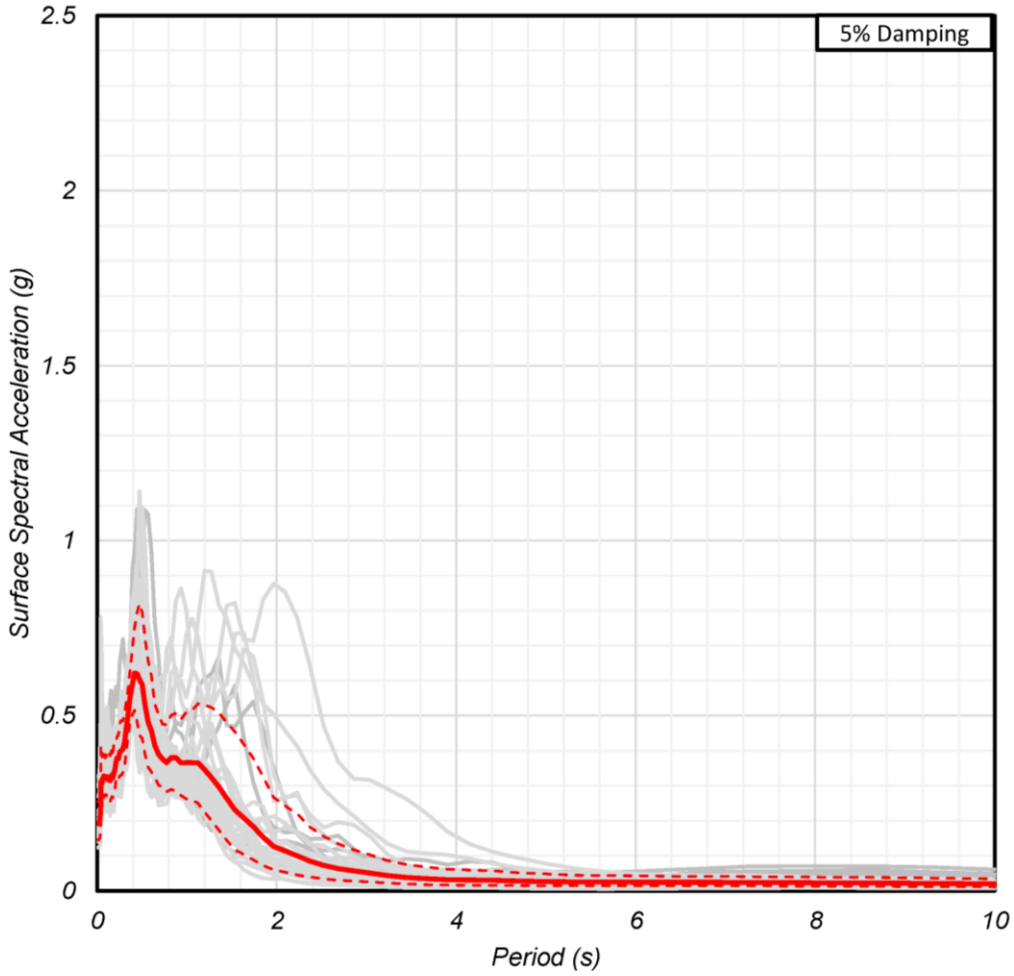

Figure 5.25: Surface acceleration from non-linear analysis—profile B3LB, NWB IN (45.11, -122.76).

Figure 5.26 through Figure 5.30 are the response spectra that correspond to location NWB OUT located at 44.75 North latitude and 122.76 West longitude.

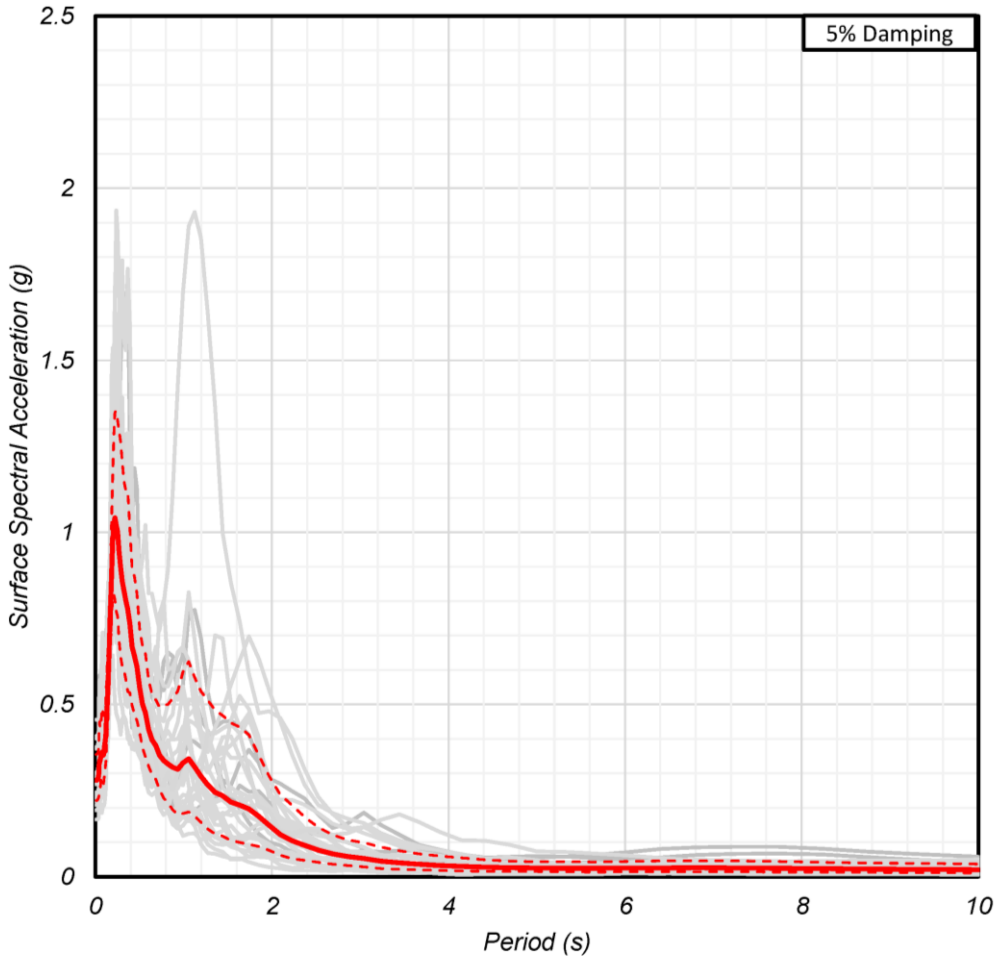

Figure 5.26: Surface acceleration from non-linear analysis—profile B1UB, NWB OUT (44.75, -122.76).

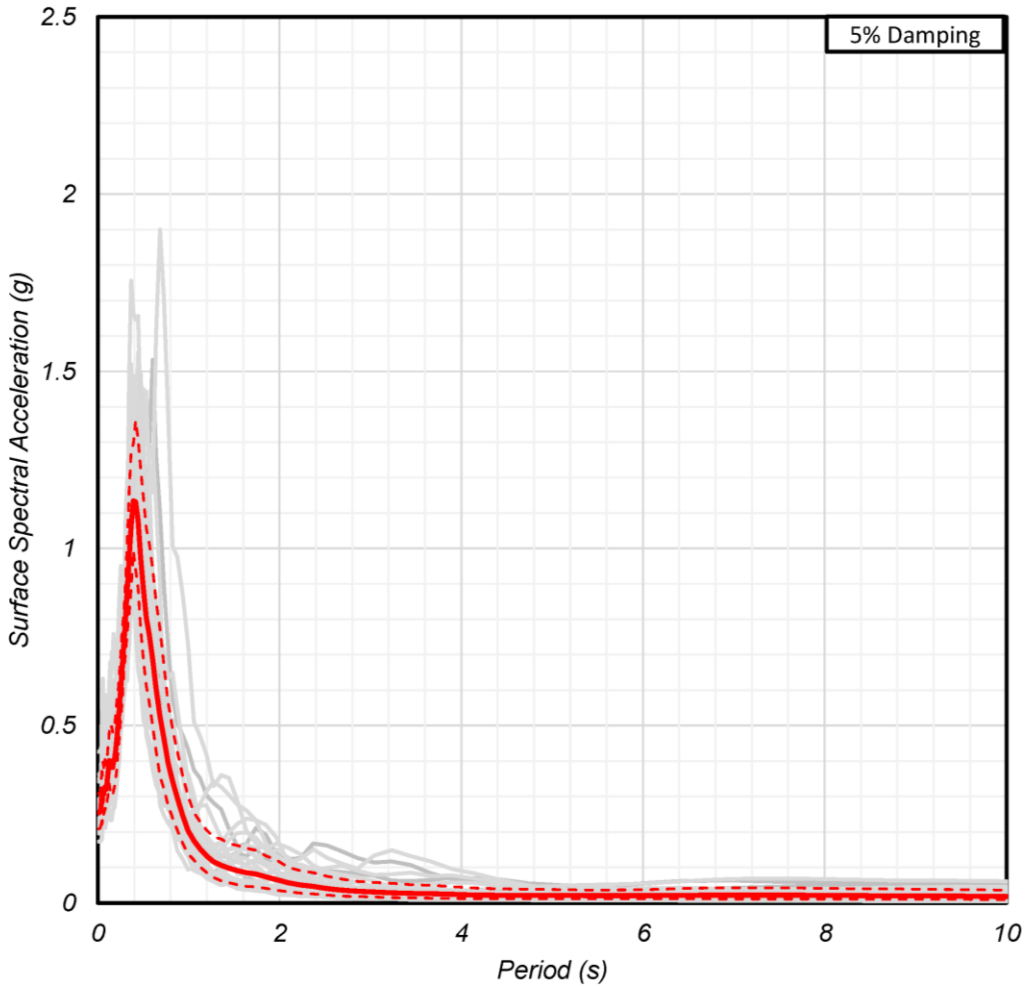

Figure 5.27: Surface acceleration from non-linear analysis—profile B1, NWB OUT (44.75, -122.76).

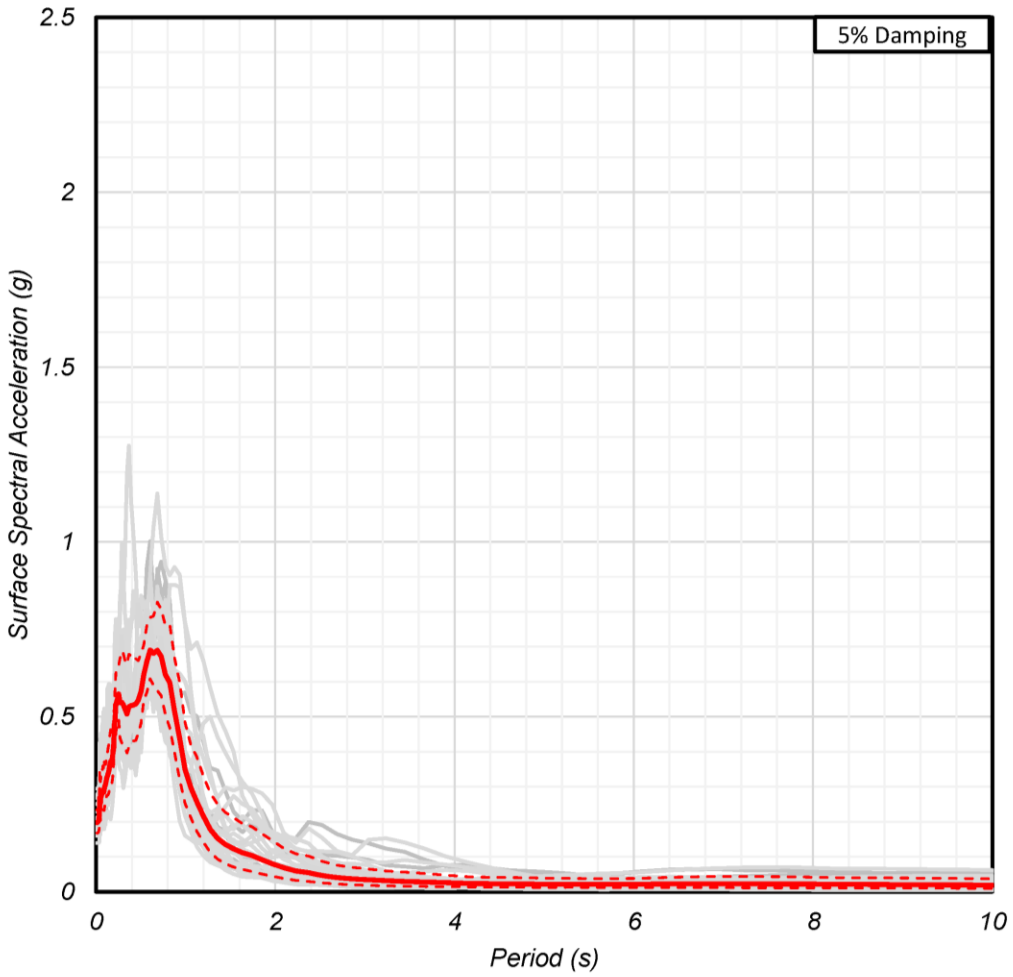

Figure 5.28: Surface acceleration from non-linear analysis—profile B2, NWB OUT (44.75, -122.76).

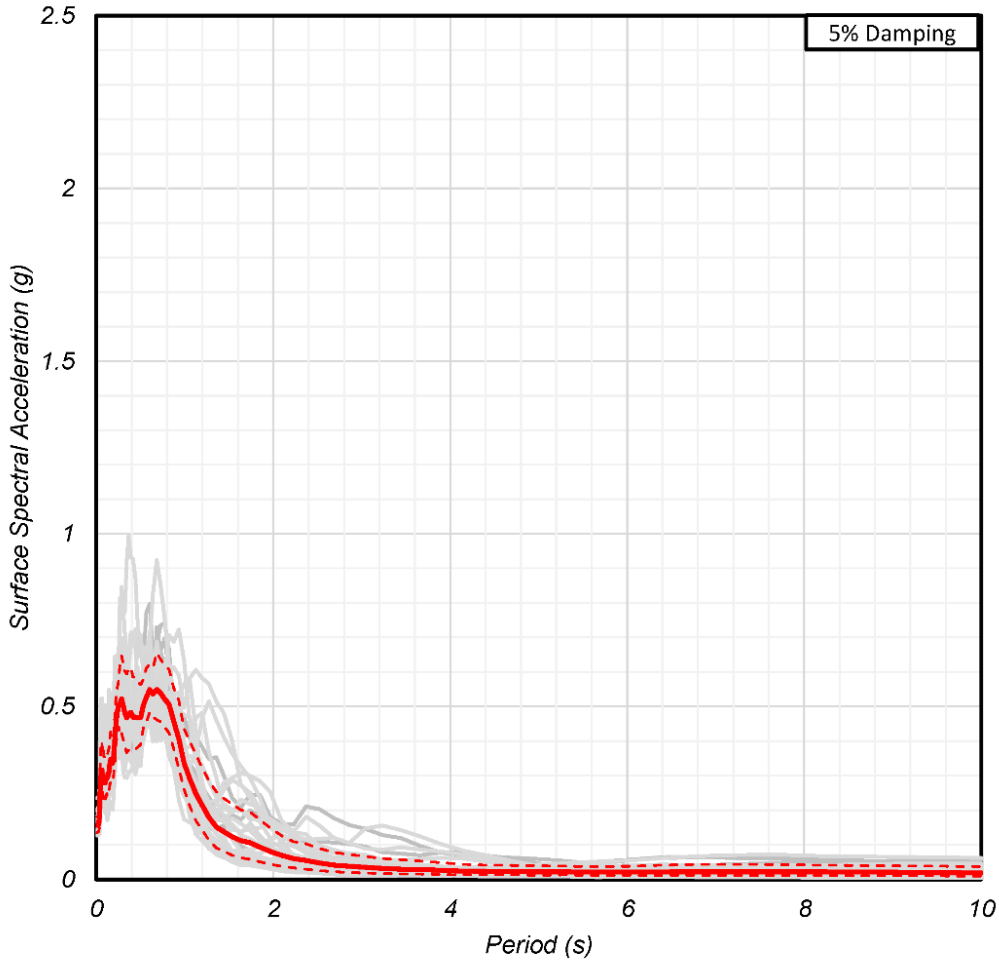

Figure 5.29: Surface acceleration from non-linear analysis—profile B3, NWB OUT (44.75, -122.76).

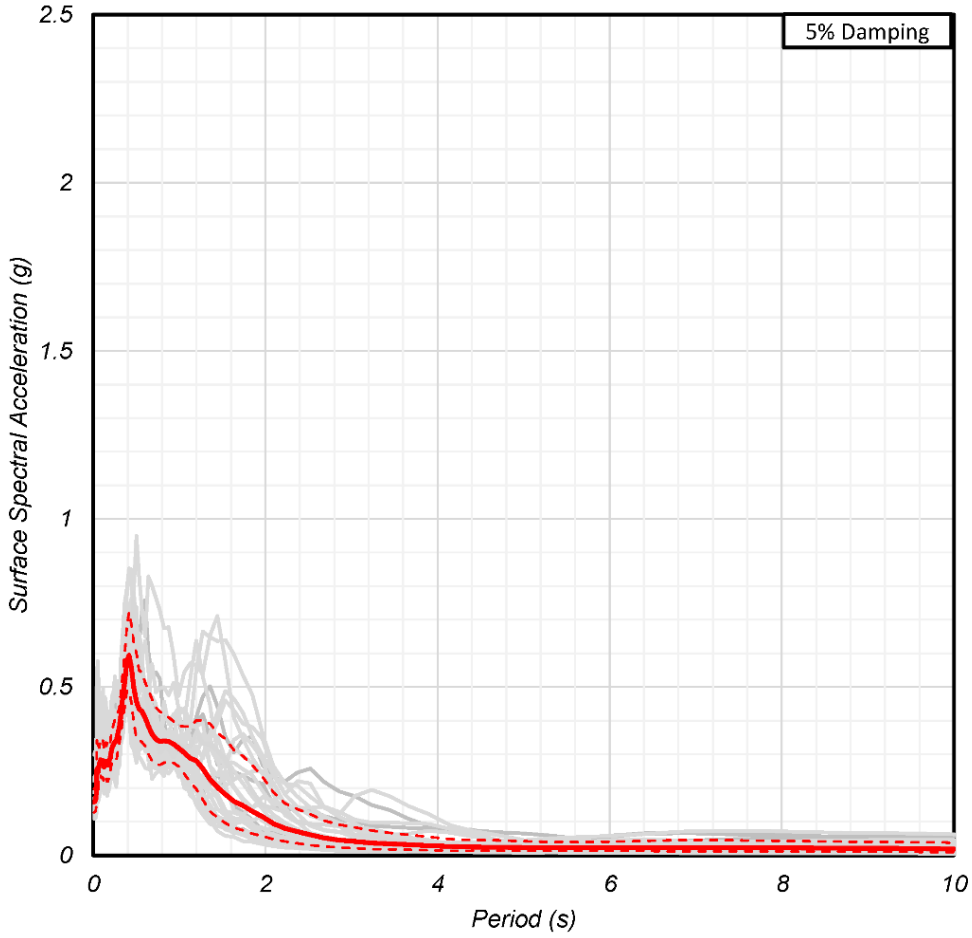

Figure 5.30: Surface acceleration from non-linear analysis—profile B3LB, NWB OUT (44.75, -122.76).

5.2 SOIL AMPLIFICATION RATIOS

Soil amplification ratios for this study were calculated as the ratio of the spectral acceleration values at the ground surface to the spectral acceleration values of the bedrock input motions as defined in equation below. Figure 5.31 through Figure 5.36 are graphs that compare the resulting soil amplification ratios for each of the five profiles at each coordinate location. Soil amplification ratios for both equivalent-linear analysis and non-linear analysis techniques are depicted in dashed and solid lines, respectively.

$$\textbf{soil amplification ratio} = \frac{\textbf{Ground surface } S_a}{\textbf{Rock outcrop } S_a} \quad \textbf{(5-1)}$$

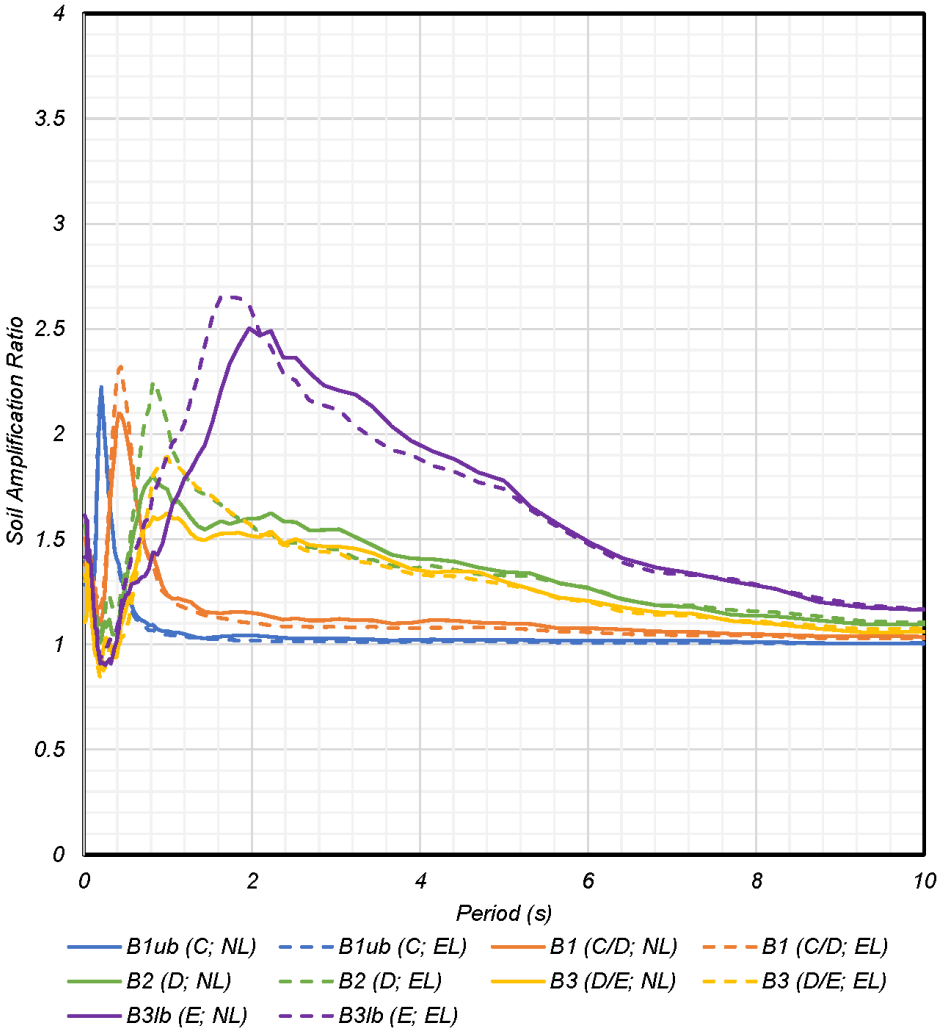

Letters denote site class; EL = Equivalent Linear; NL = Nonlinear

Figure 5.31: Soil amplification ratio using geometric means from non-linear analysis for 30 M9 realizations—PDX IN (45.58, -122.49).

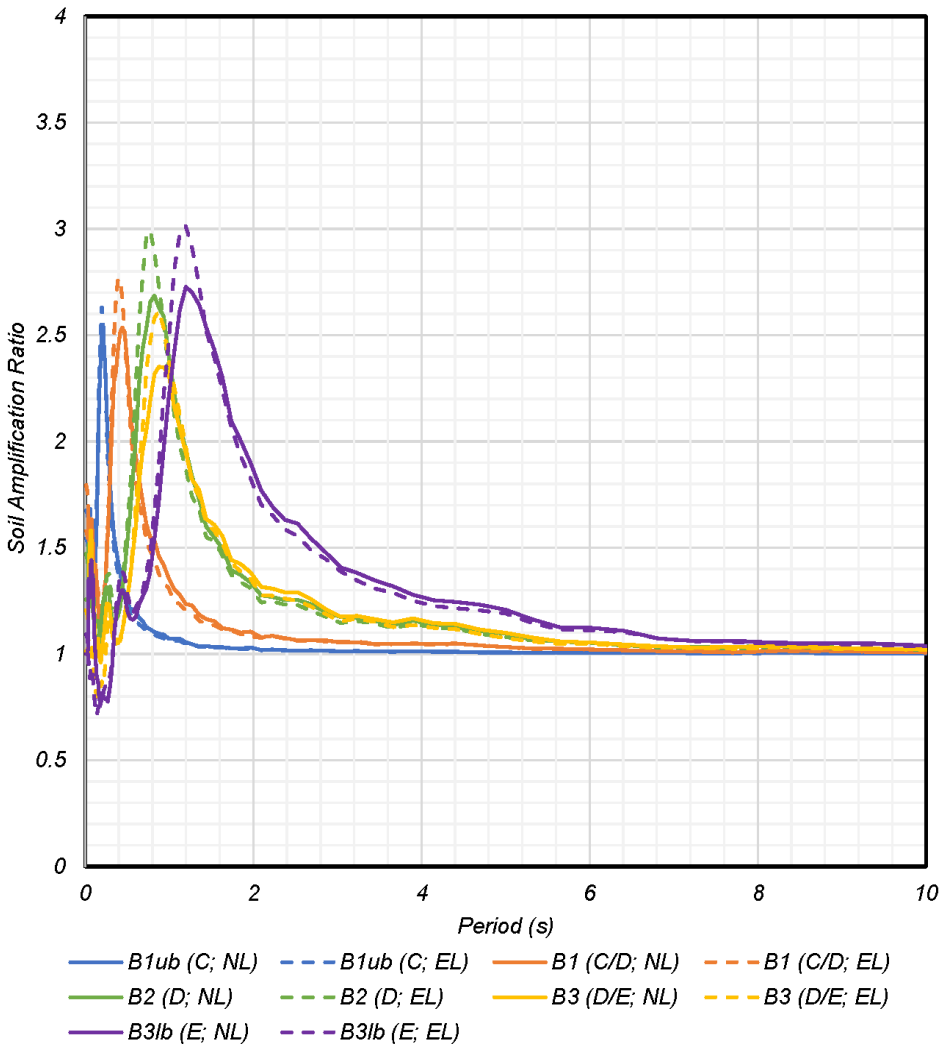

Letters denote site class; EL = Equivalent Linear; NL = Nonlinear

Figure 5.32: Soil amplification ratios using geometric means from non-linear analysis of 30 M9 realizations—PDX OUT (45.83, -122.49).

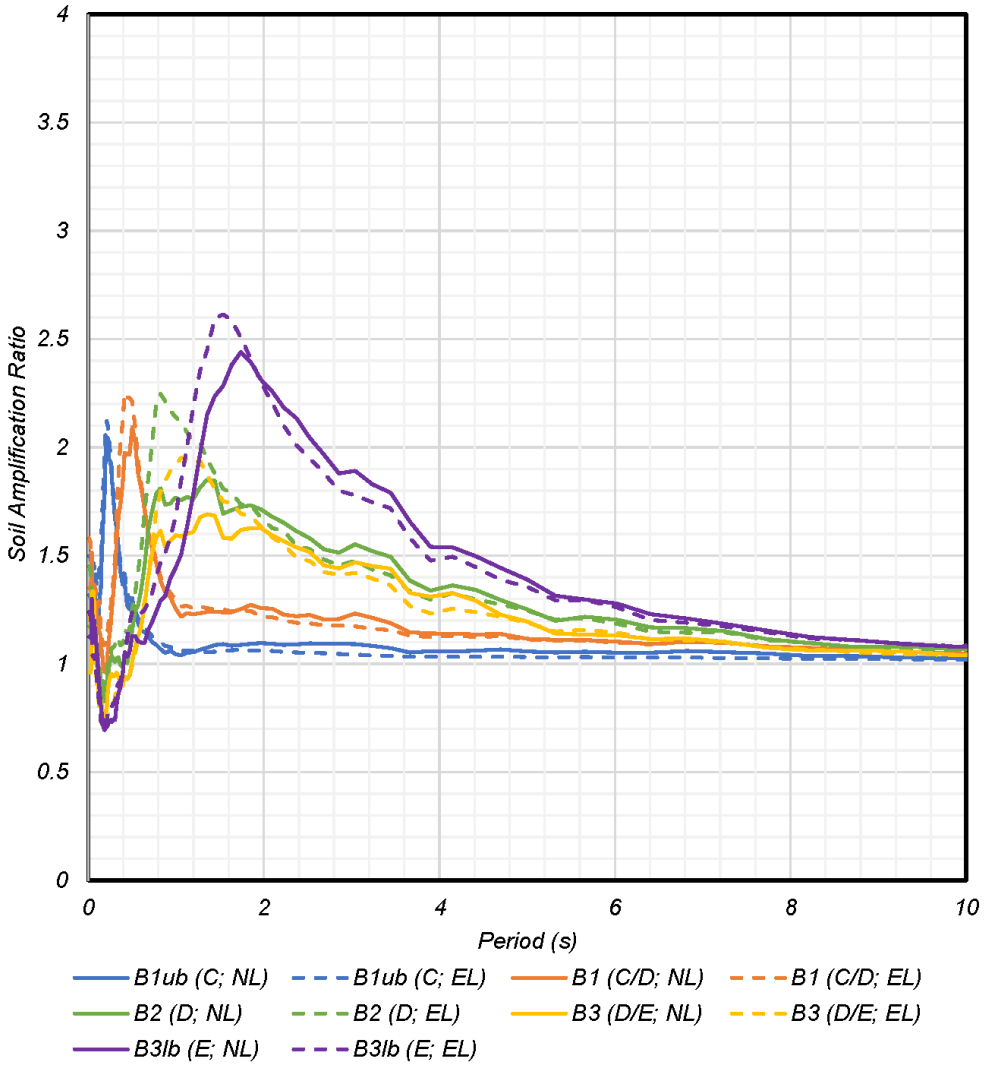

Letters denote site class; EL = Equivalent Linear; NL = Nonlinear

Figure 5.33: Soil amplification ratio using geometric means from non-linear analysis for 30 M9 realizations—TUA IN (45.52, -122.92).

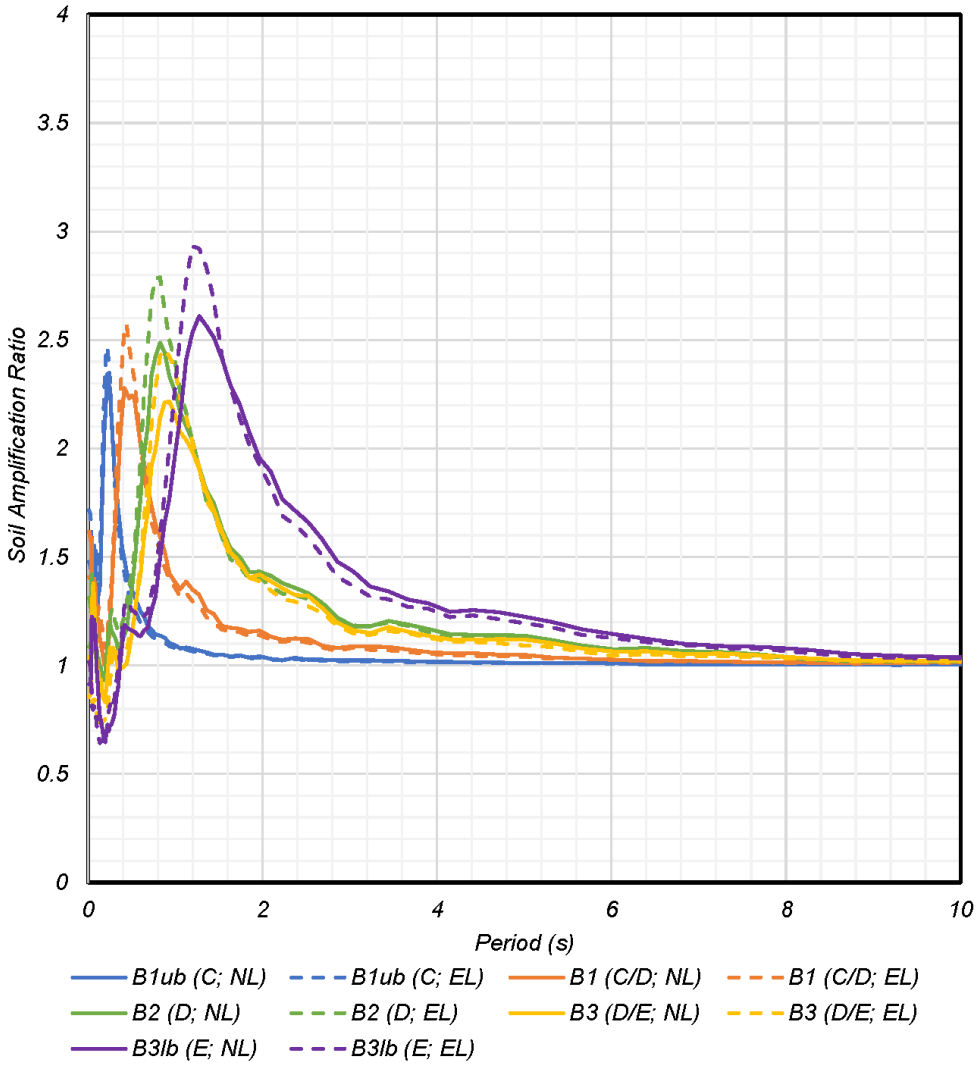

Figure 5.34: Soil amplification ratio using geometric means from non-linear analysis for 30 M9 realizations—TUA OUT (45.67, -122.92).

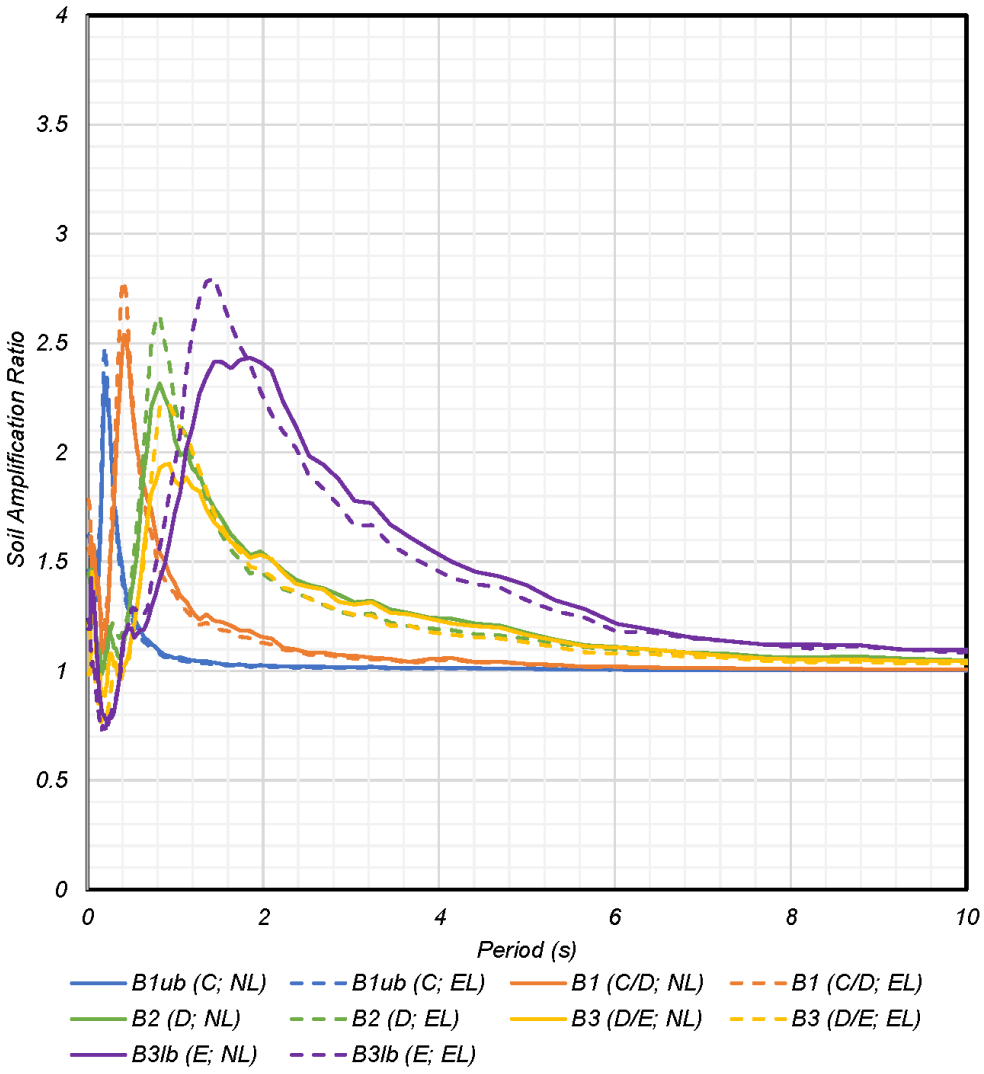

Letters denote site class; EL = Equivalent Linear; NL = Nonlinear

Figure 5.35: Soil amplification ratio using geometric means from non-linear analysis for 30 M9 realizations—NWB IN (45.11, -122.76).

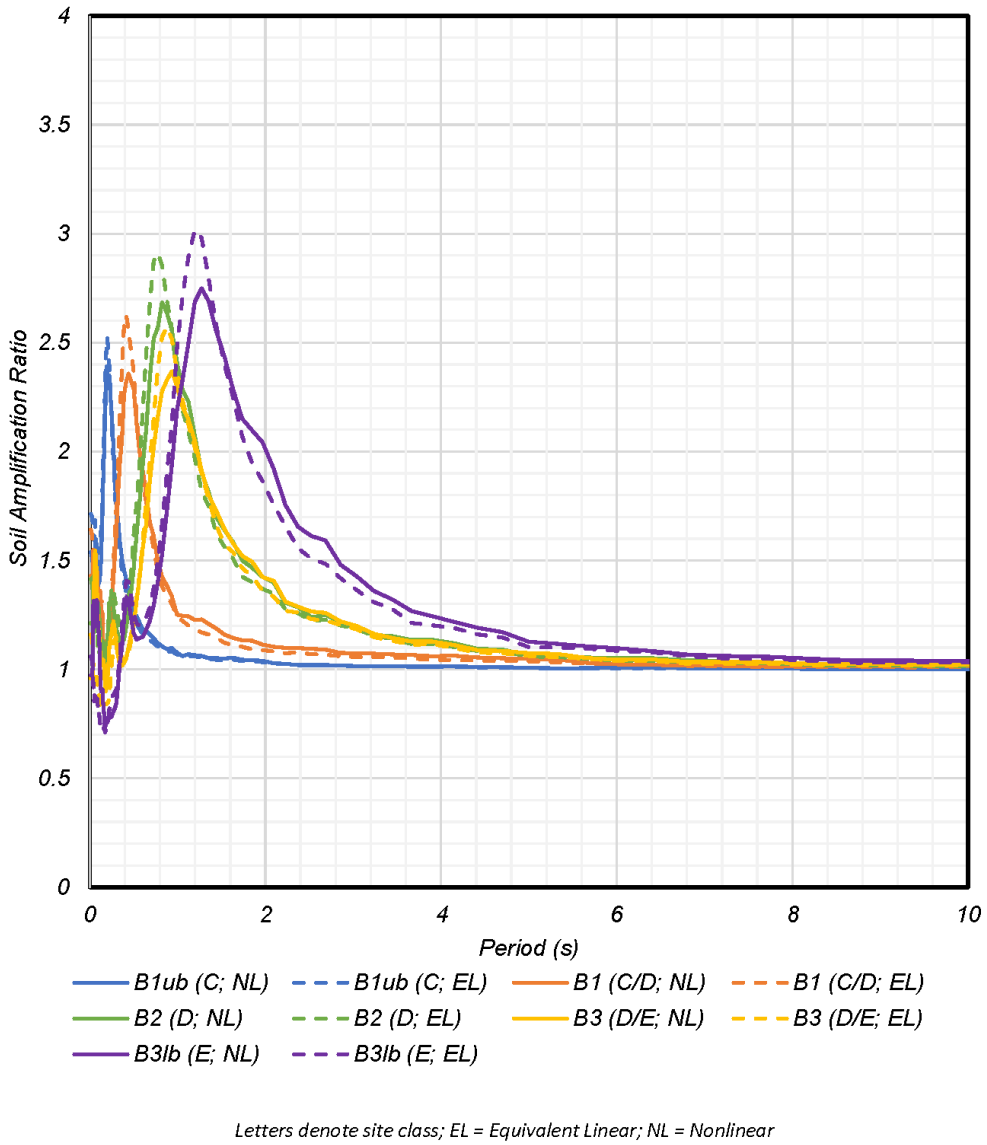

Figure 5.36: Soil amplification ratio using geometric means from non-linear analysis for 30 M9 realizations—NWB OUT (44.75, -122.76).

5.3 COMPARISON TO CODE-BASED SITE AMPLIFICATION COEFFICIENTS

We compared the soil amplification ratios from each of the five profiles at the PDX IN (45.58, -122.49) location to site amplification factors from ASCE 7 and the site amplification factor implemented in the BC Hydro GMM. The code-based site coefficients (F_a and F_v) depend on motion intensity (i.e., S_s and S_1). The site coefficients in this study were extracted based on S_s and S_1 from USGS seismic hazard maps and from the M9 motions. S_s and S_1 from the M9 motions were extracted as the mean spectral bedrock accelerations at periods of 0.2 and 1 seconds, respectively.

Figure 5.37 presents the comparison of Profile B1UB (Site Class C) to code-based based and BC-Hydro amplification values. The geometric mean of the 30 realizations reached a peak amplification of about 2.4 at short periods (about 0.2 second). Individual realizations reached peak amplifications above 3 at similar periods. At longer periods, Profile B1UB amplifications (both geometric mean and individual realizations) are well within the envelope of all code-based amplification factors.

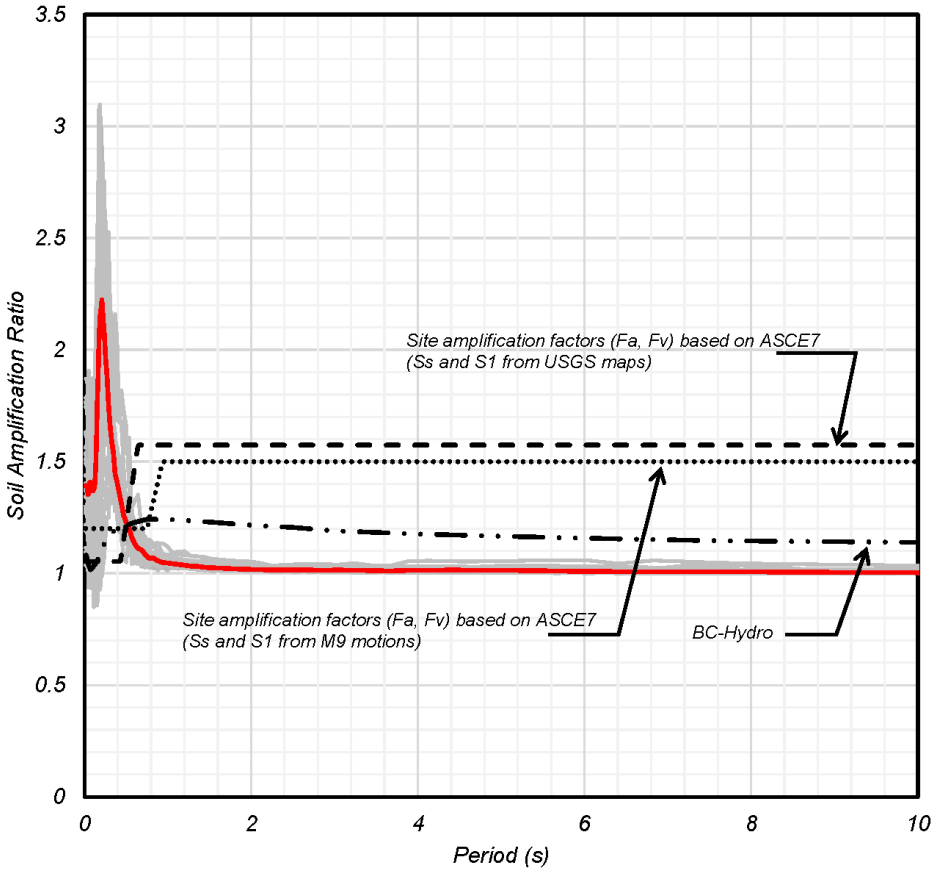

Figure 5.37: Soil amplification ratios compared to code-based site amplification factors—profile B1UB (Site Class C), PDX IN (45.58, -122.49).

Figure 5.38 presents the comparison of Profile B1 (Site Class C/D) to code-based based and BC-Hydro amplification values. The geometric mean of the 30 realizations reached a peak amplification of about 2.2 at intermediate periods (about 0.6 second). Individual realizations reached peak amplifications of about 3 at similar periods. While the peak amplifications occur at different periods, BC Hydro generally captures the amplifications of the Profile B1 geometric mean. At longer periods, Profile B1 geometric mean amplifications are well within the envelope of all code-based amplification factors. Several individual realizations approach the envelope of ASCE 7 amplification factors, with one realization exceeding all code-based amplification factors between periods of 2.0 and 3.4 seconds.

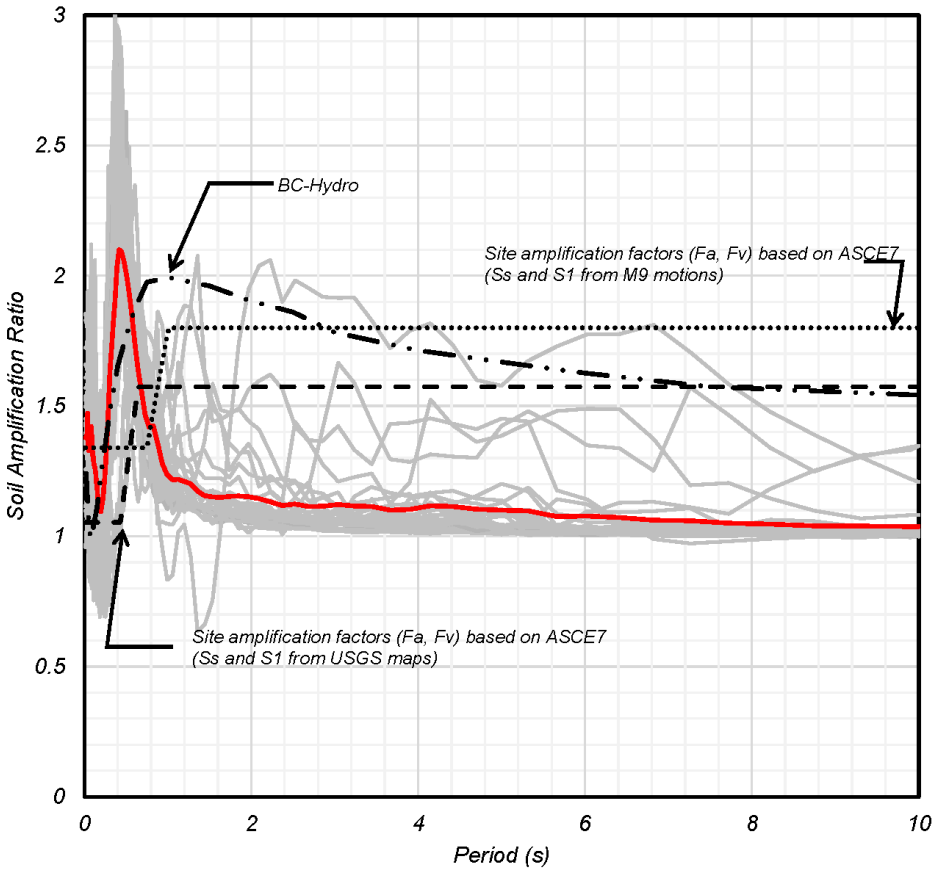

Figure 5.38: Soil amplification ratios compared to code-based site-amplification factors—Profile B1 (Site Class C/D), PDX IN (45.58, -122.49).

Figure 5.39 presents the comparison of Profile B2 (Site Class D) to code-based based and BC-Hydro amplification values. The geometric mean of the 30 realizations reached a peak amplification of about 1.8 at a period of approximately 0.8 second. Individual realizations reached peak amplifications of about 2.8 to 2.9 in the same period. A group of smaller individual realization peaks reaching amplifications of 2.7 occurs between periods of 1.6 and 3.0 seconds. Profile B2 geometric mean amplifications are generally within the envelope of the code-based amplifications. Numerous individual realizations exceed the code-based amplifications but are generally within BC-Hydro amplifications except for the largest peaks.

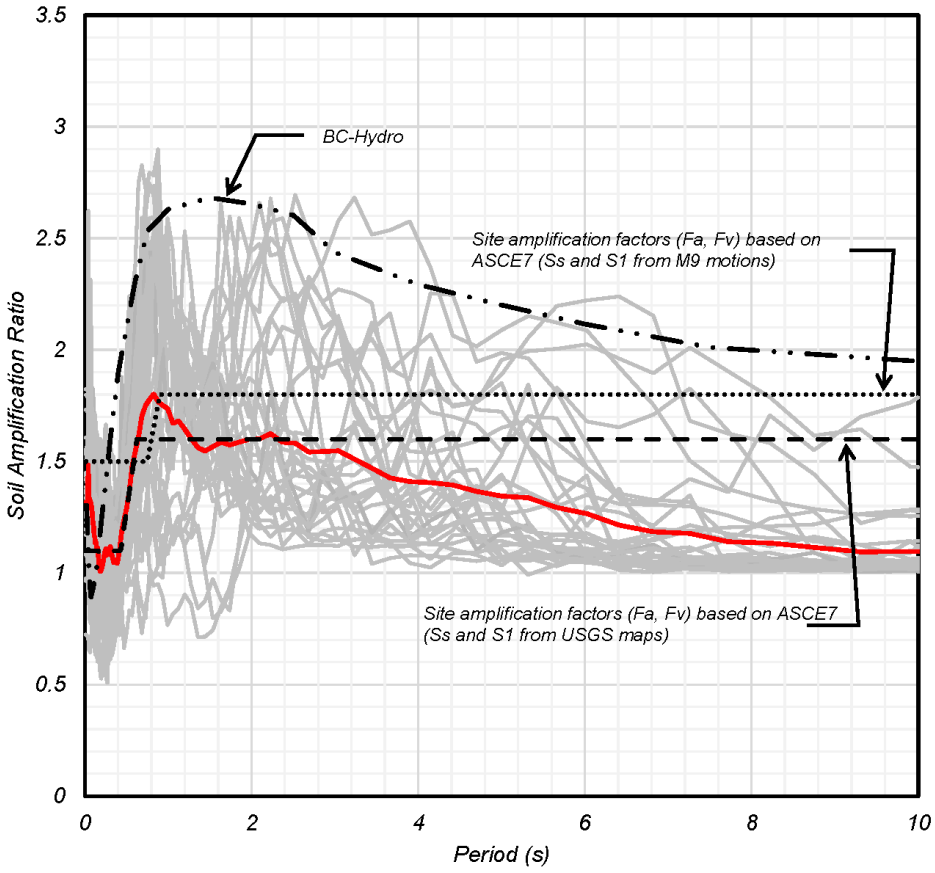

Figure 5.39: Soil amplification ratios compared to code-based site-amplification factors—Profile B2 (Site Class D), PDX IN (45.58, -122.29).

Figure 5.40 presents the comparison of Profile B3 (Site Class D/E) to code-based based and BC-Hydro amplification values. The geometric mean of the 30 realizations reached a peak amplification of about 1.6 at a period of approximately 1.0 second. Individual realizations reached peak amplifications of about 2.7 at the same period. Profile B2 geometric mean amplifications are generally within the envelope of all code-based and BC-Hydro amplifications, especially at long periods. Individual realizations reach amplifications similar to the code-based amplifications but fall outside the envelope at very short periods (<0.2 second). The individual realizations are within BC-Hydro amplifications.

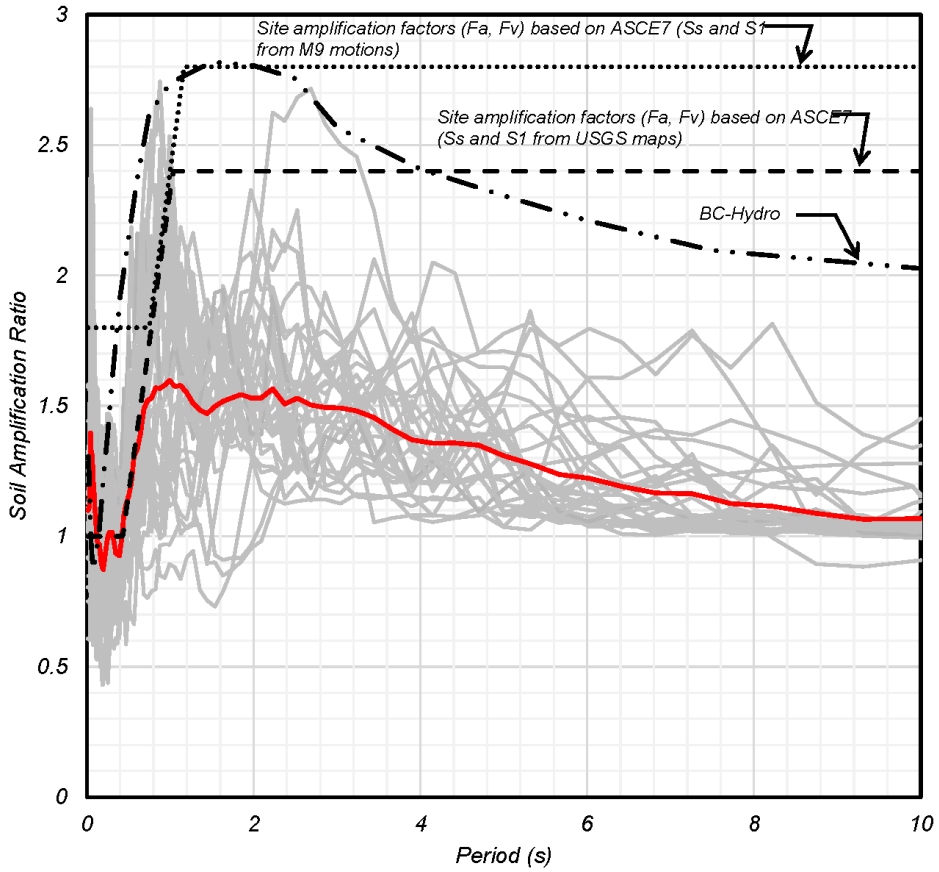

Figure 5.40: Soil amplification ratios compared to code-based site amplification factors—Profile B3 (Site Class D/E), PDX IN (45.58, -122.49).

Figure 5.41 presents the comparison of Profile B3LB (Site Class D/E) to code-based and BC-Hydro amplification values. The geometric mean of the 30 realizations reached a peak amplification of about 2.6 at a period of approximately 1.6 seconds. Individual realizations reached peak amplifications of about 3.5 at similar periods. Profile B3LB geometric mean amplifications are within BC-Hydro and ASCE 7 amplifications from M9 data but exceed ASCE 7 amplifications from USGS maps at short periods. Individual realizations exceed code-based and BC-Hydro amplifications at periods less than 2.0 seconds but fall within all amplification envelopes after a period of 5 seconds.

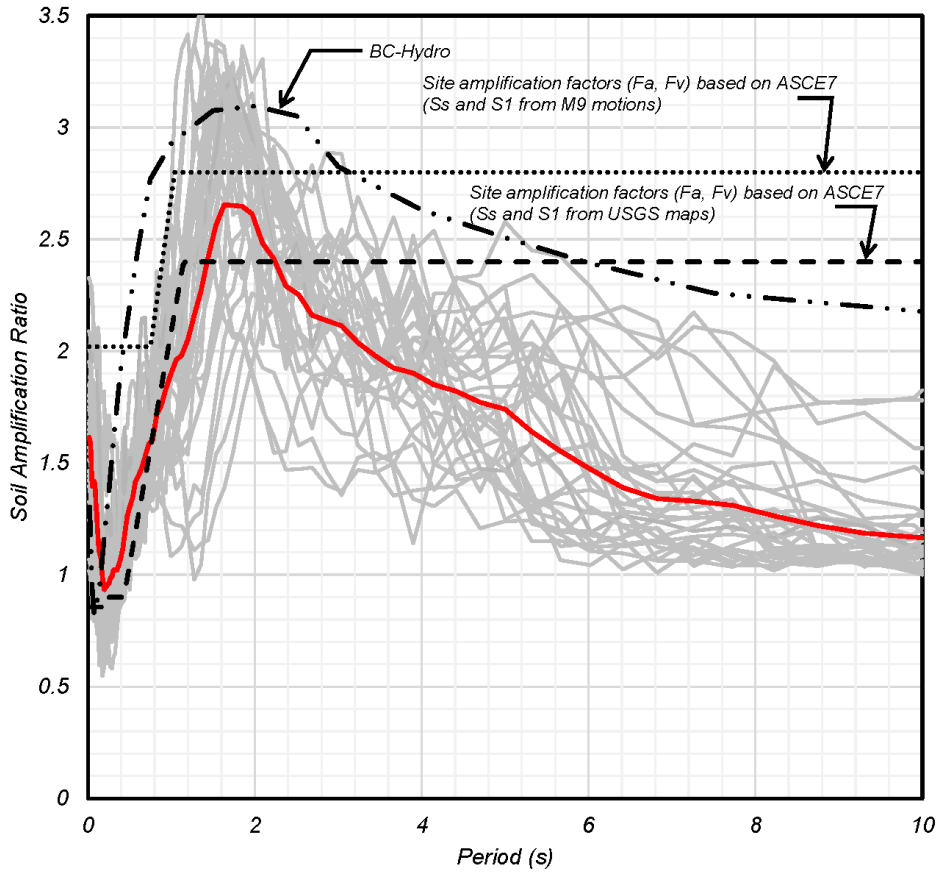

Figure 5.41: Soil amplification ratios compared to code-based site amplification factors—Profile B3LB (Site Class E), PDX IN (45.58, -122.49).

5.4 BASIN EFFECTS ON SOIL AMPLIFICATIONS

To evaluate the effects of basin motions on soil amplifications, an additional parameter was calculated by dividing the soil amplification ratios inside basin to the ratios outside basin as defined in equation below. This parameter is defined as "basin effects on soil amplification" and is intended to measure the additional impact of basins on soil amplification ratios. Figures 5.18 to 5.20 present comparisons of the basin effect on soil amplification ratios for each basin. This effect is generally bounded by a 34% decrease to 58% increase in soil amplifications for the cases studied here depending on different structural periods and soil profiles as explained next.

$$\textbf{basin effects on soil amplification} = \frac{\textbf{Soil amplification inside basin}}{\textbf{Soil amplification outside basin}} \quad \textbf{(5-2)}$$

The Portland basin, shown on Figure 5.42, displayed the largest effects of the three basins, with a peak amplification increase of about 58 percent at a period of 3.5 seconds and a peak amplification decrease of about 34 percent at a period of approximately 1.0 seconds for Profile B3LB (Site Class C). Profile B2 and B3 show amplification increases of about 20 percent at

periods from 2.0 to 6.0 seconds, and amplification decreases of about 32 percent at periods around 1.0 seconds. Profile B1 and B1UB show increases of less than 10 percent at periods greater than 1.0 seconds and decreases of about 20 percent at periods less than 0.4 seconds.

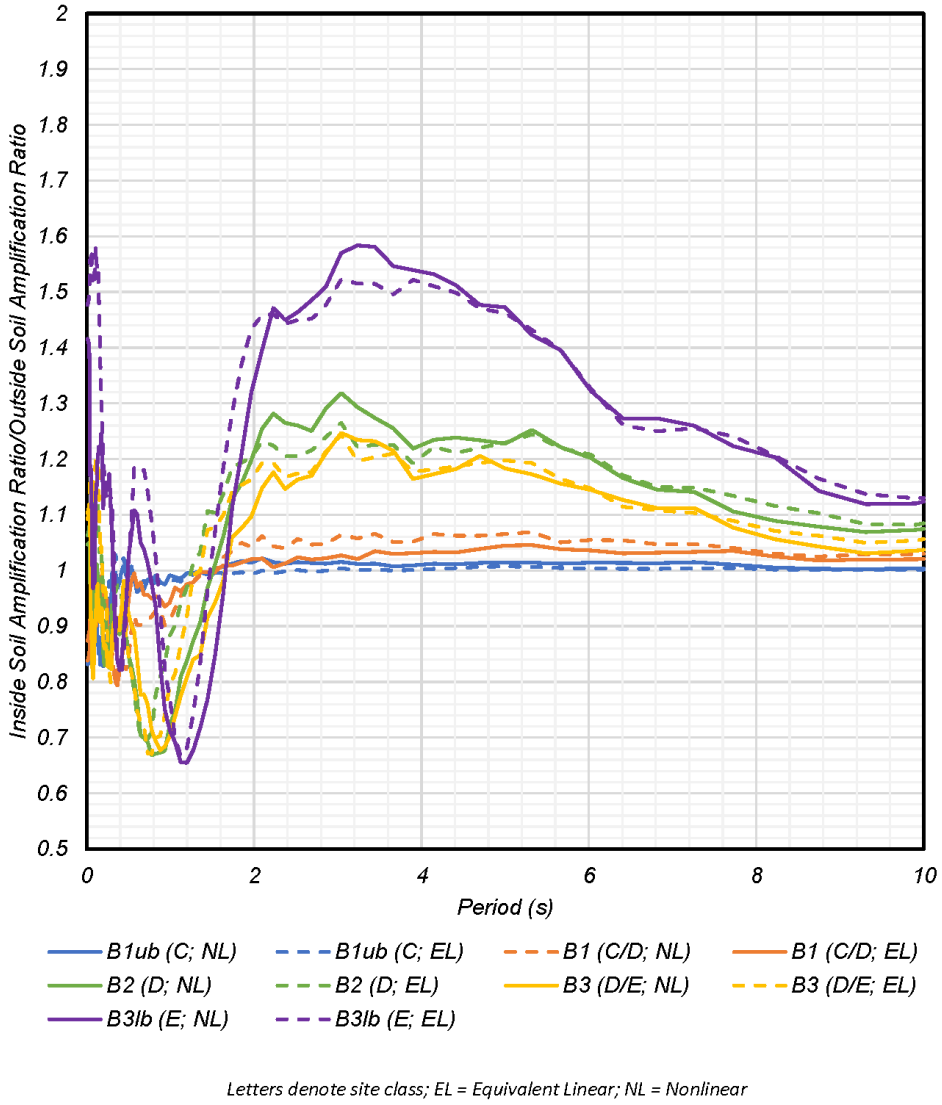

Figure 5.42: Portland basin effects on soil amplification ratios using geometric means from non-linear analysis of 30 M9 realizations.

The Tualatin basin, shown on Figure 5.43, exhibited a peak amplification increase of about 34 percent at a period of 3.2 seconds and a peak amplification decrease of about 32 percent at a period of approximately 1.0 seconds for Profile B3LB (Site Class C). Profile B2 and B3 show amplification increases of about 20 percent at periods from 2.0 to 4.0 seconds, and amplification decreases of about 30 percent at periods around 1.0 seconds. Profile B1 and B1UB show increases of about 10 percent or less at periods greater than 1.0 seconds and decreases of about 10 to 15 percent at periods less than 1.0 seconds.

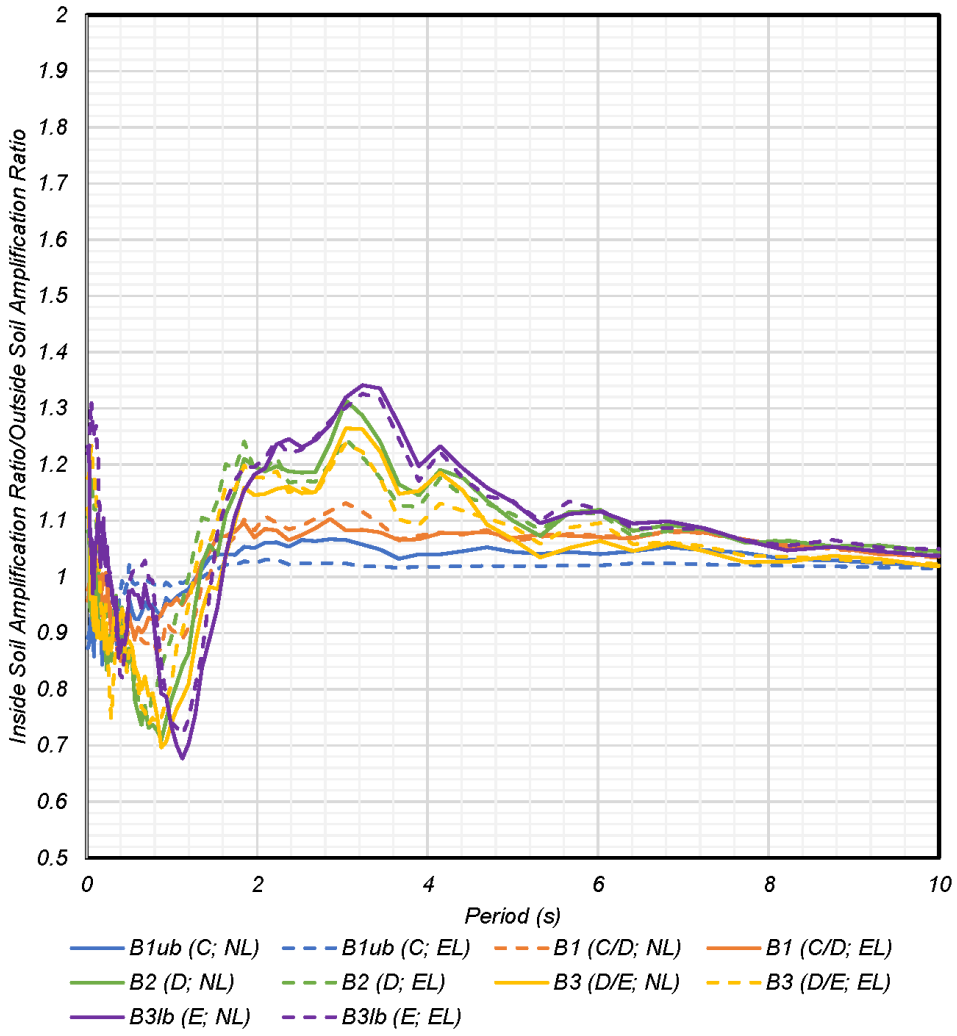

Letters denote site class; EL = Equivalent Linear; NL = Nonlinear

Figure 5.43: Tualatin basin effects on soil amplification ratios using geometric means from non-linear analysis of 30 M9 realizations.

The North Willamette basin, shown on Figure 5.20, exhibited a peak amplification increase of about 30 percent between periods of 2.0 to 4.0 seconds and a peak amplification decrease of about 20 percent at a period of approximately 1.0 seconds for Profile B3LB (Site Class C). Profile B2 and B3 show amplification increases of about 10 percent at periods from 2.0 to 6.0 seconds, and amplification decreases of about 30 percent at periods around 1.0 seconds. Profile B1 shows increases of about 10 percent, or less, at periods less than 1.0 seconds and no effect at periods greater than 1.0 seconds. Profile B1UB exhibited minimal effects.

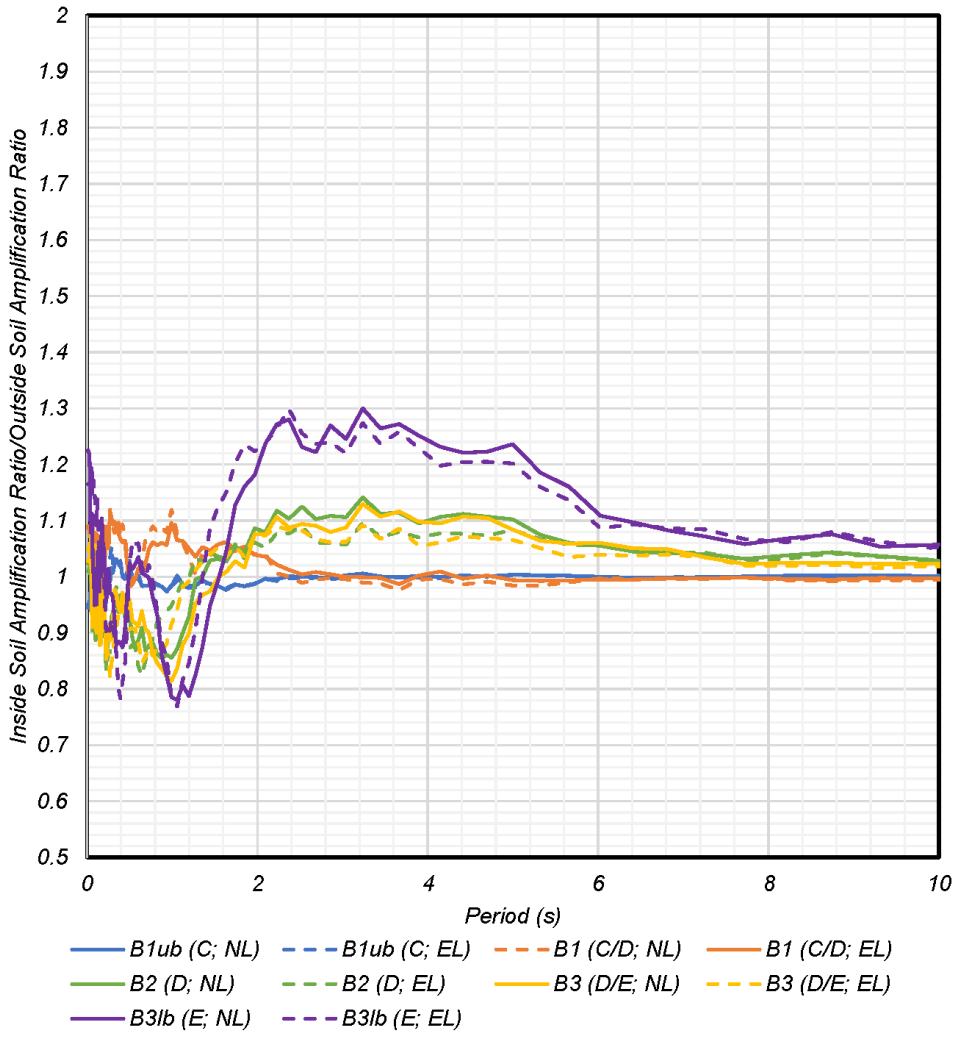

Figure 5.44: North Willamette basin effects on soil amplification ratios using geometric means from non-linear analysis of 30 M9 realizations.

6.0 SUMMARY AND CONCLUSIONS

6.1 PROJECT SUMMARY

Site response analyses were performed for locations in the Portland, Tualatin, and North Willamette basins using simulated Cascadia Subduction Zone earthquake ground motions developed by the M9 Project. Nonlinear and equivalent linear 1D analyses were performed using the program DEEPSOIL on five soil profiles representing a range of site classes from Site Class C to Site Class E. The profiles were developed to represent different site classes. A total of 1,800 analyses were performed for all the profile and coordinate combinations. The results were compared to site response analyses of the same profiles at non-basin reference sites to evaluate the basin effects on site response (i.e., soil amplification ratios).

6.2 CONCLUSIONS

The following conclusions are made based on the results of the site response analyses and comparisons to literature and code-based amplification values:

1. The M9 synthetic motions produce basin amplification ratios that are within the range observed from other studies involving recorded accelerometer data (e.g., Frankel and Grant 2021, Frankel et al. 2009, and Marafi et al. 2017). However, the basin amplification factors calculated in this study are noticeably larger than the ratios calculated from empirical correlations that are incorporated in NGA-West2 GMMs (e.g., Campbell and Bozorgnia 2014). It is recommended that the basin amplification factors characterized in this study be considered in combination with the results from other studies using empirical methods such as those in NGA-West2 (Campbell & Bozorgnia, 2014) and Frankel and Grant (2021).

2. The soil amplification ratios calculated from the site response analyses generally fall within the envelope of code-based site coefficients F_a and F_v in ASCE 7, except for very short periods (<0.5 seconds). Considering the large uncertainties associated with predicting ground motion intensities, it appears reasonable to continue using the current code-based site coefficients per ASCE 7 for sites inside and outside basins.

3. The effect of basin on soil amplification factor was characterized by comparing the soil amplifications inside and outside basins for the same soil profiles. This effect generally ranged from 50 percent increase to 30 percent decrease. The decrease in soil amplification ratios observed at periods close to the natural period of the basin (generally between 1 sec and 2 sec) may benefit projects with that period of interest. Site-specific site response analyses may be used in those cases to determine if this benefit is applicable.

7.0 REFERENCES

Abrahamson, N. A., Silva, W. A., & Kamai, R. (2014). Summary of the ASK14 ground motion relation for active crustal regions. *Earthquake Spectra*, *30*(3), 1025–1055. https://doi.org/10.1193/070913eqs198m

Beck, J. D., & Hall, J. E. (1986). Factors contributing to the catastrophe in Mexico City during the earthquake of September 19, 1985. *Geophysical Research Letters*, *13*(6), 593–596. https://doi.org/10.1029/gl013i006p00593

Boore, D. M., Stewart, J. P., Seyhan, E., & Atkinson, G. M. (2014). NGA-West2 equations for predicting PGA, PGV, and 5% damped PSA for shallow crustal earthquakes. *Earthquake Spectra*, *30*(3), 1057–1085. https://doi.org/10.1193/070113eqs184m

Campbell, K. S., & Bozorgnia, Y. (2014). NGA-West2 ground motion model for the average horizontal components of PGA, PGV, and 5% damped linear acceleration response spectra. *Earthquake Spectra*, *30*(3), 1087–1115. https://doi.org/10.1193/062913eqs175m

Chang, S. M., Frankel, A. E., & Weaver, C. S. (2014). Report on workshop to incorporate basin response in the design of tall buildings in the Puget Sound region, Washington. *Open-file Report /*. https://doi.org/10.3133/ofr20141196

Chiou, B. S., & Youngs, R. R. (2014). Update of the Chiou and Youngs NGA model for the average horizontal component of peak ground motion and response spectra. *Earthquake Spectra*, *30*(3), 1117–1153. https://doi.org/10.1193/072813eqs219m

Darendeli, M. B. (2001). *Development of a new family of normalized modulus reduction and material damping curves* (Doctoral dissertation, 2001). Austin, TX: University of Texas.

Day, S. M., Graves, R., Bielak, J., Dreger, D. S., Larsen, S., Olsen, K. R., . . . Ramirez-Guzman, L. (2008). Model for basin effects on long-period response spectra in Southern California. *Earthquake Spectra*, *24*(1), 257–277. https://doi.org/10.1193/1.2857545

Evarts, R. C., O'Connor, J. E., Wells, R. E., & Madin, I. P. (2009). The Portland Basin: A (big) river runs through it. *GSA Today*, 4–10. https://doi.org/10.1130/gsatg58a.1

Frankel, A. E., & Grant, A. (2021). Site response, basin amplification, and earthquake stress drops in the Portland, Oregon area. *Bulletin of the Seismological Society of America*, *111*(2), 671–685. https://doi.org/10.1785/0120200269

Frankel, A. E., Stephenson, W. J., & Carver, D. (2009). Sedimentary basin effects in Seattle, Washington: Ground-motion observations and 3D simulations. *Bulletin of the Seismological Society of America*, *99*(3), 1579–1611. https://doi.org/10.1785/0120080203

Frankel, A. E., Wirth, E. A., Marafi, N. A., Vidale, J. E., & Stephenson, W. J. (2018). Broadband synthetic seismograms for magnitude 9 earthquakes on the Cascadia megathrust based on 3D simulations and stochastic synthetics, Part 1: Methodology and overall results. *Bulletin of the Seismological Society of America*, *108*(5A), 2347–2369. https://doi.org/10.1785/0120180034

Groholski, D. R., Hashash, Y. M. A., Kim, B., Musgrove, M. T., Harmon, J. E., & Stewart, J. P. (2016). Simplified model for small-strain nonlinearity and strength in 1D seismic site response analysis. *Journal of Geotechnical and Geoenvironmental Engineering*, *142*(9). https://doi.org/10.1061/(asce)gt.1943-5606.0001496

Hashash, Y.M.A., Musgrove, M.I., Harmon, J.A., Ilhan, O., Xing, G., Numanoglu, O…, & Park, D. (2020). *DEEPSOIL 7.0, user manual*. Urbana, IL: Board of Trustees of University of Illinois at Urbana-Champaign. Retrieved from http://deepsoil.cee.illinois.edu/Publications.html

Hatayama, K., Kanno, T., & Kudo, K. (2007). Control factors of spatial variation of long-period strong ground motions in the Yufutsu sedimentary basin, Hokkaido, during the Mw 8.0 2003 Tokachi-oki, Japan, Earthquake. *Bulletin of the Seismological Society of America*, *97*(4), 1308–1323. https://doi.org/10.1785/0120060200

Kakoty, P., Dyaga, S., & Hutt, C. (2020). Quantifying basin amplification in Southwest BC from simulated M9 Cascadia subduction zone earthquakes. In *Seismic isolation, energy dissipation and active vibration control of structures: 17th World Conference on Seismic Isolation (17WCSI)*. Sendai, Japan: Springer.

Kakoty, P., Dyaga, S. M., & Hutt, C. M. (2021). Impacts of simulated M9 Cascadia subduction zone earthquakes considering amplifications due to the Georgia sedimentary basin on reinforced concrete shear wall buildings. *Earthquake Engineering & Structural Dynamics*, *50*(1), 237–256. https://doi.org/10.1002/eqe.3361

Marafi, N. A., Eberhard, M. O., Berman, J. W., Wirth, E. A., & Frankel, A. E. (2017). Effects of deep basins on structural collapse during large subduction earthquakes. *Earthquake Spectra*, *33*(3), 963–997. https://doi.org/10.1193/071916eqs114m

McPhee, D. K., Langenheim, V. E., Wells, R. E., & Blakely, R. J. (2014). Tectonic evolution of the Tualatin basin, northwest Oregon, as revealed by inversion of gravity data. *Geosphere*, *10*(2), 264–275. https://doi.org/10.1130/ges00929.1

Moug, D. M., Khosravifar, A., & Dusicka, P. (2022). Ground deformation evaluation using numerical analyses and physics-based mega-thrust subduction zone motions. In *Geotechnical, geological and earthquake engineering* (pp. 961–970). Springer International Publishing. https://doi.org/10.1007/978-3-031-11898-2_73

Petersen, M. D., Shumway, A. M., Powers, P. E., Mueller, C., Moschetti, M. P., Frankel, A. E., … Zeng, Y. (2020). The 2018 update of the US National Seismic Hazard Model: Overview of model and implications. *Earthquake Spectra*, *36*(1), 5–41. https://doi.org/10.1177/8755293019878199

Petersen, M.D., Zeng, Y., Haller, K.M., McCaffrey, R., Hammond, W.C., … & Thatcher, W.R., (2014). *Geodesy-and geology-based slip-rate models for the Western United States (excluding California) national seismic hazard maps*. Reston, Virginia: US Geological Survey. https://doi.org/10.3133/ofr20131293

Pratt, T. G., & Brocher, T. M. (2006). Site response and attenuation in the Puget Lowland, Washington State. *Bulletin of the Seismological Society of America*, *96*(2), 536–552. https://doi.org/10.1785/0120040200

Pratt, T. G., Brocher, T. M., Weaver, C. S., Creager, K. C., Snelson, C., Crosson, R. S., . . . Tréhu, A. M. (2003). Amplification of seismic waves by the Seattle Basin, Washington State. *Bulletin of the Seismological Society of America*, *93*(2), 533–545. https://doi.org/10.1785/0120010292

Roe, W.P. & Madin, I.P. (2013). *3D geology and shear-wave velocity models of the Portland, Oregon, Metropolitan Area*. Portland, OR: Oregon Department of Geology and Mineral Industries (DOGAMI). Retrieved from https://digital.osl.state.or.us/islandora/object/osl%3A73139

Stephenson, W.J., Reitman, N.G., & Angster, S.J. (2017). *P-and S-wave velocity models incorporating the Cascadia subduction zone for 3D earthquake ground motion simulations, Version 1.6—Update for Open-File Report 2007–1348.* Reston, Virginia: US Geological Survey. Retrieved from https://pubs.usgs.gov/of/2017/1152/ofr20171152.pdf